POLITECNICO DI TORINO

Dipartimento di Elettronica e Telecomunicazioni

DIPARTIMENTO INTERATENEO DI FISICA "M. MERLIN"

European Semiconductor Laser Workshop

September 21-22, 2018

Centro Polifunzionale Studenti

Università degli Studi di Bari,

Piazza Cesare Battisti, 1, Bari, Italy

Sponsors

Puglia PROMOZIONE Agenzia Regionale del Turismo

THORLABS

WELCOME

Dear Colleagues,

It is our pleasure to welcome you to the Workshop on "European Semiconductor Laser Workshop 2018" at Università degli Studi di Bari, Italy.

The workshop is jointly organized in Bari, Italy by the Department of Electronics and Telecommunications, Politecnico di Torino and the Department of Physics, Politecnico and Università degli Studi di Bari just before the 44^{th} European Conference and Exhibition on Optical Communication (ECOC-2018, September 23^{rd} – 27^{th} in Rome, Italy). The ESLW 2018 aims at providing an informal discussion forum on most recent research results and achievements in the field of semiconductor lasers, related devices, applications and technology.

The organizing committee

ESLW2018 Organizing Committee

Paolo **Bardella** paolo.bardella@polito.it
Politecnico di Torino, Italy

Massimo **Brambilla** massimo.brambilla@uniba.it
Politecnico ed Università degli Studi di Bari, Italy

Lorenzo Luigi **Columbo** lorenzo.columbo@polito.it
Politecnico di Torino, Italy

Mariangela **Gioannini** mariangela.gioannini@polito.it
Politecnico di Torino, Italy

Gaetano **Scamarcio** gaetano.scamarcio@uniba.it
Politecnico ed Università degli Studi di Bari, Italy

ESLW2018 Scientific Committee

Stephane **Barland** stephane.barland@inphyni.cnrs.fr
Université Côte d'Azur, CNRS-INPHYNI, France

Adonis **Bogris** abogris@teiath.gr
University of West Attica, Greece

Stefan **Breuer** stefan.breuer@physik.tu-darmstadt.de
Technische Universität Darmstadt, Germany

Giampiero **Contestabile** giampiero.contestabile@santannapisa.it
Scuola Superiore Sant'Anna, Pisa, Italy

Pierluigi **Debernardi** pierluigi.debernardi@ieiit.cnr.it
CNR IEIIT Torino, Italy

Mariangela **Gioannini** mariangela.gioannini@polito.it
Politecnico di Torino, Italy

Guido **Giuliani** guido.giuliani@unipv.it
Università degli studi di Pavia, Italy

Frederic **Grillot** frederic.grillot@telecom-paristech.fr
Télécom ParisTech, France

Åsa **Haglund** asa.haglund@chalmers.se
Chalmers University of Technology, Sweeden

Julien **Javaloyes** julien.javaloyes@uib.es
University of the Balearic Islands, Palma de Maiorca, Spain

Christian **Jirauschek** jirauschek@tum.de
Technische Universität München, Germany

Bryan **Kelleher** bryan.kelleher@ucc.ie
University College Cork & Tyndall National Institute, Ireland

Sylwester **Latkowski** s.latkowski@tue.nl
Technische Universiteit Eindhove, Eindhoven, The Netherlands

Huiyun **Liu** huiyun.liu@ucl.ac.uk
University College London, United Kingdom

Kathy **Lüdge** kathy.luedge@tu-berlin.de
Technische Universität Berlin, Germany

Gaetano **Scamarcio** gaetano.scamarcio@uniba.it
Università degli studi di Bari, Italy

Kresten **Yvind** kryv@fotonik.dtu.dk
Technical University of Denmark, Denmark

Participants

Nicola **Andriolli** nicola.andriolli@santannapisa.it
Scuola Superiore Sant'Anna di Pisa, Italy

Dominik **Auth** dominik.auth@physik.tu-darmstadt.de
Technische Universität Darmstadt, Germany

Paolo **Bardella** paolo.bardella@polito.it
Politecnico di Torino, Italy

Massimo **Brambilla** massimo.brambilla@uniba.it
Università degli Studi e Politecnico di Bari, CNR-IFN, Italy

Stephane **Barland** stephane.barland@unice.fr
Université Côte d'Azur, CNRS-INPHYNI, France

Lorenzo Luigi **Columbo** lorenzo.columbo@polito.it
Politecnico di Torino, Italy

Maurizio **Dabbicco** maurizio.dabbicco@uniba.it
Università degli Studi di Bari, CNR-IFN, Italy

Wolfgang **Elsäßer** elsaesser@physik.tu-darmstadt.de
Technische Universität Darmstadt, Germany

Andrea **Fiore** a.fiore@tue.nl
Technische Universiteit Eindhoven, The Netherlands

Marcin **Gebski** marcin.gebski@p.lodz.pl
Technische Universität Berlin, Germany

Mariangela **Gioannini** mariangela.gioannini@polito.it
Politecnico di Torino, Italy

Nasibeh **Haghighi** nasibeh.haghighi@tu-berlin.de
Technische Universität Berlin, Germany

Jan Philipp **Hausen** jan.hausen@yahoo.de
Technische Universität Berlin, Germany

Andreas **Herdt** andreas.herdt@physik.tu-darmstadt.de
Technische Universität Darmstadt, Germany

Diana **Huffaker** huffaker.diana@gmail.com
Cardiff University, United Kingdom

German **J de Valcarcel** german.valcarcel@uv.es
Universitat de València, Spain

Lewis **Kastein** kasteinl3@cf.ac.uk
Cardiff University, United Kingdom

Niall **Kelly** n.p.kelly@tue.nl
Technische Universiteit Eindhoven, The Netherlands

Bryan **Kelleher** bryan.kelleher@ucc.ie
University College Cork (IRL), Ireland

Gunter **Larisch** larisch@ciomp.ac.cn
Bimberg Chinese-German Center of Green Photonics, China

Di **Liang** di.liang@hpe.com
HP Labs Palo Alto, USA

Alberto **Maina** alberto.maina@primaelectro.com
Prima Electro S.p.A., Italy

Cristina **Masoller** cristina.masoller@upc.edu
Universitat Politecnica de Catalunya, Spain

Robert **McKenna** mckennr2@tcd.ie
Trinity College Dublin, Ireland

Alexandru **Mereuta** alexandru.mereuta@epfl.ch
Ecole Polytechnique Fédérale de Lausanne, Switzerland

Rainer **Michalzik** rainer.michalzik@uni-ulm.de
Universität Ulm (DE), Germany

Emilia **Pruszynska-Karbownik** emilia.pruszynska-karbownik@p.lodz.pl
Lodz University of Technology, Poland

Thorsten **Rasmussen** thsv@fotonik.dtu.dk
Technical University of Denmark, Denmark

Johann Peter **Reithmaier** jpreith@ina.uni-kassel.de
University of Kassel, Germany

Alejandro **Rosado Pérez** alejandro.rosado.perez@gmail.com
Universidad Politécnica de Madrid, Spain

Marco **Saldutti** marco.saldutti@polito.it
Politecnico di Torino, Italy

Gaetano **Scamarcio** gaetano.scamarcio@uniba.it
Univesrità degli Studi di Bari, CNR-IFN, Italy

Carlo **Silvestri** carlo.silvestri@polito.it
Politecnico di Torino, Italy

Vincenzo **Spagnolo** vincenzoluigi.spagnolo@poliba.it
PolySense Laboratory, Politecnico di Bari and Thorlabs GMBH, Italy

Patrycja **Śpiewak** patrycja.spiewak@edu.p.lodz.pl
Lodz University of Technology, Poland

Olivier **Spitz** olivier.spitz@telecom-paristech.fr
LTCI Télécom ParisTech-Université Paris-Saclay, France

Miriam **Vitiello** miriam.vitiello@sns.it
NEST, CNR - Istituto Nanoscienze and Scuola Normale Superiore, Italy

Michal **Wasiak** michal.wasiak@p.lodz.pl
Lodz University of Technology, Poland

Christoph **Weber** christoph.weber@physik.tu-darmstadt.de
Technische Universität Darmstadt, Germany

James **Whiteaway** james@ranovus.com
Ranovus Inc., Canada

Workshop program

September 21st, morning

8h15 – 8h45

Registration

8h45 – 9h00

Welcome and opening

Session 1.
Optical communication and optical interconnect – I

9h00 – 9h30

Monolithically integrated optical frequency comb generator based on cascaded modulators (Invited talk)

*N. Andriolli**, T. Cassese, M. Chiesa, and G. Contestabile

Scuola Superiore Sant'Anna, CNIT*

9h30 – 9h45

Radio-frequency and relative intensity noise analysis of a self mode-locked single-section quantum-dot laser

*C. Weber**, P. Bardella, L. L. Columbo, L. F. Lester, M. Gioannini, and S. Breuer

Technische Universiteit Darmstadt, Politecnico di Torino, Virginia Polytechnic Institute and State University*

9h45 – 10h00

Detector-free bidirectional symmetric communication scheme based on compound states of two mutually coupled diode lasers

M. Weidmann, *A. Herdt**, R. Phelan, and W. Elsäßer

Technische Universität Darmstadt, Eblana Photonics Ltd., West Pier Business Campus*

10h00 – 10h15

A curved lumped element electroabsorption modulator suitable for flip-chip integration

*N.P. Kelly**, J. O'Callaghan, A. Gocalinska, K. Thomas, E. Peluchhi, and F.H. Peters

Eindhoven University of Technology, Tyndall National Institute*

10h15 – 10h45

Coffee break, Restaurant Urban, Via Domenico Nicolai 10

Session 2.
Semiconductor lasers dynamics

10h45 – 11h00

Mean-field dynamics of a fully connected network of spiking neuromorphic semiconductor lasers
A. Dolcemascolo, A. Miazek, F. Marino, R. Veltz, *S. Barland**
Université Côte d'Azur, CNRS INPHYNI, CNR-INO*

11h00 – 11h15

Optical frequency comb generation from semiconductor lasers using pulsed excitation and optical injection
*A. Rosado**, A. Pérez-Serrano, J. M. G Tijero, A. Valle, L. Pesquera, and I. Esquivias
Universidad Politécnica de Madrid, Instituto de Física de Cantabria*

11h15 – 11h30

Dual-cavity optical self-feedback stabilization of a passively mode-locked quantum-well laser
*D. Auth**, C. Weber, A. Klehr, A. Knigge, and S. Breuer
Technische Universität Darmstadt, Leibniz-Institut für Höchstfrequenztechnik*

11h30 – 11h45

Experimental characterization of transitions between locking regimes in a semiconductor laser with optical feedback and small amplitude current modulation
J. Tiana-Alsina, C. Quintero-Quiroz, M. C. Torrent, and *C. Masoller*
Universitat Politecnica de Catalunya

11h45 – 12h00

Novel excitability and canard explosions in optically injected quantum dot lasers
M. Dillane, D. Goulding, I. Dubinkin, N. Federov, E. A. Viktorov, and *B. Kelleher**
University College Cork, Tyndall National Institute*, Cork Institute of Technology, ITMO, Université Libre de Bruxelles*

12h00 – 12h15

Multi-wavelength analysis of synthetic tissue samples by optical feedback interferometry
*M. Dabbicco**, M. C. Cardilli
Università degli Studi di Bari, CNR-IFN**

12h15 – 13h30

Lunch break, Restaurant Urban, Via Domenico Nicolai 10

September 21st, afternoon

Session 3.
Nano-lasers and novel light sources

13h30 – 13h45

Semiconductor-based broad-band superluminescent diodes: a novel light source for photon correlation metrology: ghost imaging, ghost spectroscopy and ghost polarimetry

W. Elsäßer, P. Janassek, and S. Blumenstein

Technische Universität Darmstad

13h45 – 14h00

Improved feedback stability of semiconductor nanolasers by inclusion of a Fano mirror

T. S. Rasmussen and J. Mørk

Technical University of Denmark

14h00 – 14h30

Spontaneous and stimulated emission in nanoscale light sources (Invited talk)

A. Fiore, B. Romeira, V. Dolores-Calzadilla, A. Higuera-Rodriguez, D. Heiss, and M.K. Smit

Technische Universiteit Eindhoven

Session 4.
Modelling and numerical simulation

14h30 – 14h45

Understanding the emergence of non-equidistant multi-pulse emission in passively mode-locked VECSELs

J. Hausen, S. Meinecke, B. Lingnau, and K. Lüdge

Technische Universität Berlin

14h45 – 15h00

Master equation for modelocking in lasers with fast gain recovery

A. M. Perego, B. Garbin, F. Gustave, S. Barland, F. Prati, and *G. J. de Valcárcel**

*Aston University, The University of Auckland, Université Côte d'Azur-CNRS INPHYNI, Università dell'Insubria, Universitat de València**

15h00 – 15h15

Near field analysis of broad-area high-power laser diode using non-linear bidirectional beam propagation method

A. Maina and C. Coriasso

Prima Electro S.p.A.

15h15 – 15h30

Numerical model of small signal modulation response for vertical-cavity surface-emitting lasers

*M. Wasiak**, P. Śpiewak, E. Pruszyńska-Karbownik, M. Gębski, P. Komar J. A. Lott, and R. P. Sarzała

Lodz University of Technology, Technische Universität Berlin*

15h30 – 17h00

Coffee break, Restaurant Urban, Via Domenico Nicolai 10

Poster session:

Impact of the laser structure and driving current on the modulation properties of a 980 nm GaAs-based VCSEL

*E. Pruszyńska-Karbownik**, P. Śpiewak, P. Komar, J. A. Lott, and M. Wasiak

Lodz University of Technology, Technische Universität Berlin*

Coupled-Bloch-Wave analysis of PhC lasers

*M. Saldutti**, J. Mørk, P. Bardella, I. Montrosset, and M. Gioannini

Politecnico di Torino, Technical University of Denmark*

Computer modeling of a nitride tunnel junction VCSEL

P. Śpiewak, M. Wasiak, and R. P. Sarzała

Lodz University of Technology

A multiphysics electro-thermo-opto VCSEL simulator

A. Tibaldi, F. Bertazzi, M. Goano, M. Daubenschüz, *R. Michalzik**, and P. Debernardi

*CNR-IEIIT, Politecnico di Torino, Philips GmbH, Ulm University**

Session 5.
VCSELs and VECSEL

17h00 – 17h15

New type of vertical-cavity surface-emitting laser incorporating a monolithic high contrast grating mirror

*M. Gebski**, J. A. Lott, and T. Czyszanowski

Technische Universität Berlin, Lodz University of Technology**

17h15 – 17h30

Trade-off in high bandwidth versus high optical output power in 980 nm VCSELs

N. Haghighi, G. Larisch, and J. A. Lott

Technische Universität Berlin

17h30 – 17h45

Electrically-pumped wafer-fused VECSELs emitting at 1550-nm wavelength range

A. Mereuta, A. Caliman, A. Rudra, G. Suruceanu, and E. Kapon

Ecole Polytechnique Fédérale de Lausanne

17h45 – 18h00

Photo session

19h00 – 20h00

Old town (Bari Vecchia) guided tour

20h30

Gala dinner, Restaurant La Biglietteria, Largo Adua 234

September 22nd, morning

9h00 – 9h45

Nanoscale for optical integration (Keynote talk)

D. Huffaker

Cardiff University

Session 6.
Optical communication and optical interconnect – II

9h45 – 10h15

1.55 µm quantum dot lasers and amplifiers with high temperature stability (Invited talk)

*J. P. Reithmaier**, G. Eisenstein

University of Kassel, Technion – Israel Institute of Technology*

10h15 – 10h45

Heterogeneous multi-wavelength quantum-dot light sources on silicon (Invited talk)

D. Liang, G. Kurczveil, C. Zhang, A. Descos, Y. Hu, M. Fiorentino, and R. Beausoleil

HP Labs Palo Alto

10h45 – 11h00

Energy-efficient VCSELs for 200+ Gb/s optical interconnects

*G. Larisch**, R. Rosales, J. A. Lott, and D. Bimberg

Bimberg Chinese-German Center of Green Photonics – Chinese Academy of Sciences (CAS), Technische Universität Berlin*

11h00 – 11h30

Coffee break, Restaurant Urban, Via Domenico Nicolai 10

11h30 – 12h15

Photonic engineering of high performance quantum cascade lasers at Terahertz frequencies (Keynote talk)

M. Vitiello

NEST – CNR Istituto Nanoscienze

Session 7.
QCLs and their applications

12h15 – 12h45

Recent advancements in QCL-based quartz-enhanced photoacoustic spectroscopy for gas sensing applications (Invited talk)

P. Patimisco, A. Sampaolo, M. Giglio, V. Mackoviak, H. Rossmadl, A. Cable, F.K. Tittel, and *V. Spagnolo**

PolySense Lab-University and Politecnico of Bari, Rice University*, Thorlabs GmbH, Thorlabs, Inc.*

12h45 – 13h00

Entrainment phenomenon in a mid-infrared QCL with external optical feedback and low frequency modulation

*O. Spitz**, J. Wu,M. Carras, C. W. Wong, F. Grillot

LTCI Télécom ParisTech-Université Paris-Saclay, Centre d'intégration NanoInnov*, UCLA*, Southwest University Chongqing, University of New-Mexico*

13h00 – 13h15

Terahertz self-detection near-field microscopy: recent advances in the weak feedback regime

*M. Brambilla**, C. Silvestri, L. L. Columbo, G. Scamarcio

Università degli Studi e Politecnico di Bari, CNR-IFN*, Politecnico di Torino*

13h15 – 13h25

Closing remarks

13h25

Lunch, Restaurant Urban, Via Domenico Nicolai 10

Abstracts

Monolithically integrated optical frequency comb generator based on cascaded modulators

N. Andriolli[1,2,*], T. Cassese[1,2], M. Chiesa[1,2], and G. Contestabile[1,2]

1 Scuola Superiore Sant'Anna, Via Moruzzi, 1, 56124, Pisa, Italy
2 CNIT, Photonic Networks & Technologies National Lab, Via Moruzzi 1,56124 Pisa, Italy
** nicola.andriolli@santannapisa.it*

Summary: We present an InP photonic integrated frequency comb generator realized on a generic integration platform and composed of a DBR laser and a cascade of intensity and phase modulators. The maximum tested repetition frequency was 10 GHz, mainly limited by the bandwidth of the available lumped modulators. 28 spectral lines within a 5 dB power range have been demonstrated at a repetition frequency of 5 GHz.

1. Introduction

The use of optical frequency comb generators is promising for many applications, comprising metrology, spectroscopy, optical communications, THz generation, optical arbitrary waveform generation, and microwave photonic filters [1-5]. Each application imposes its own design specifications and constraints, however a high correlation between optical modes and a small footprint are typically required. To this aim, the implementation of a comb generator in a single integrated device is desirable. Various techniques have been used for the purpose, such as mode-locking laser diodes [6], microresonators [7], pulsed operation in a semiconductor gain switched laser or vertical cavity surface emitting laser (VCSEL) [8]. The solution that we studied consists in a cascade of optical modulators driven by synchronous electrical sinusoidal signals [9]. This scheme allows the generation of stable optical combs with tunable frequency separation. However, the implementation typically requires a bulky setup comprising a monochromatic laser and a number of modulators. In this paper we present, to the best of our knowledge, the first photonic integrated implementation of such a scheme.

2. Integrated comb generator design

We designed and realized the monolithically integrated comb generator based on cascaded modulators shown in Fig. 1. Fig. 1(a) sketches the scheme of the photonic integrated circuit (PIC), Fig. 1(b) shows a microscopy image of the fabricated device, and Fig. 1(c) a picture of the packaged PIC. The CW signal at a selectable wavelength is provided either by an on-chip tunable distributed Bragg reflector laser diode (DBR-LD), or by an external laser and injected into the PIC via a spot-size-converter (SSC) used to maximize the coupling between fiber and waveguide. The CW signal, coupled through a 2×2 MMI, can either be sent out of the chip through another SSC for monitoring purposes or be directed to a Mach-Zehnder modulator (MZM) realized by means of a 1×2 multi-mode interference device (MMI) used as a splitter, two 1-mm-long phase modulators (PM), and a 2×1 MMI used as a coupler. The output of this coupler is fed into a series of two further 1-mm-long PM, identical to the previous ones. Finally, the modulated signal crosses a 0.5-mm-long multi quantum-well SOA before reaching the output SSC. Anti-reflective coating has been added on the chip facets. Arrays of square and round metal pads (for DC and RF contacts respectively) have been placed for bare chip testing by means of multiprobes.

The InP PIC has been fabricated by Oclaro Technology plc, UK, in a multi-project wafer run exploiting generic integration technology [10]. The footprint of the integrated comb regenerator is around 4.5×2.5 mm^2, limited by the orthogonal placement constraint of phase modulators and gain sections. The chip was mounted on a metal base using a thermally and electrically conductive epoxy, and then wire bonded to a custom-built PCB, as shown in Fig. 1(c). The temperature was controlled by means of a thermo-electric cooler (TEC) placed below the metal base.

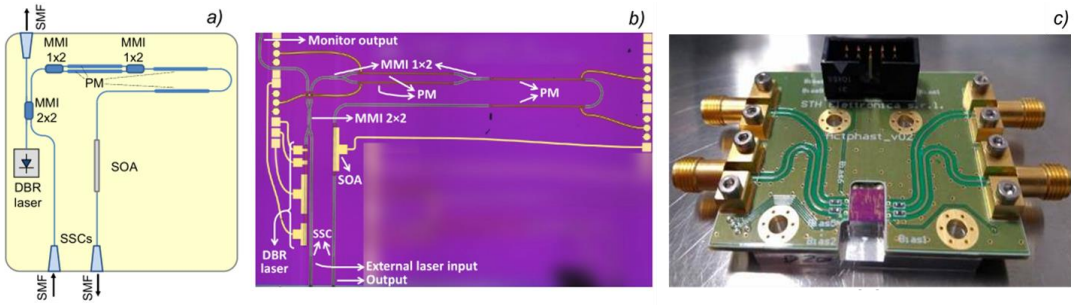

Fig. 1. (a) Scheme of photonic integrated circuit (PIC) implementing the optical frequency comb generator. (b) Picture of the fabricated PIC (Footprint: 3x2.5 mm^2). (c) PIC-PCB assembly.

3. Experimental characterization

The performance of the PMs was assessed through a test MZM identical to the one in the comb generator: we measured an extinction ratio of 27 dB, a 3 dB bandwidth for the PMs of 6.8 GHz and V_π = 4.5V at V_{bias} = -10V. Due to the limited bandwidth of the available lumped modulators, we utilized a maximum repetition frequency of 10 GHz. Fig. 2 depicts the experimental setup used to test the comb generator. Synchronous modulation is obtained by means of a low-noise sinusoidal signal generator, whose signal was then split in four and crossed four different RF phase shifter used as delay lines. The signals were then amplified by electrical drivers and coupled to the bias voltages through four high bandwidth bias-tees. The DBR laser and the SOA were controlled by means of laser drivers connected to the PIC through a multiple pin interface on the PCB.

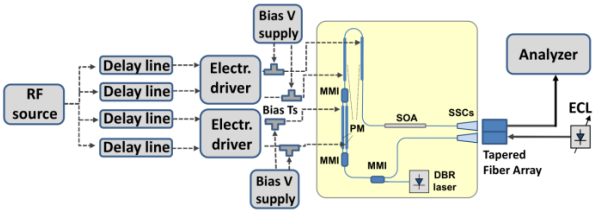

Fig. 2. Comb generator measurement setup.

To achieve a larger comb line count and enhanced comb flatness, phase modulators should be driven with multi-V_π voltages and the MZM with around V_π voltages. However, in our setup voltage swings were limited by the available electrical driver amplifiers. Some results of the measurement are reported in Fig. 3, showing the optical spectrum at the output of the comb generator driven by a 5 GHz sinusoidal signal: Fig. 3(a) exploits the integrated DBR, while Fig. 3(b) exploits an external cavity laser. The former spectrum shows 28 lines in a 5 dB power range, while the latter spectrum appears cleaner, showing less noise at low power levels due to a much larger SMSR and smaller linewidth.

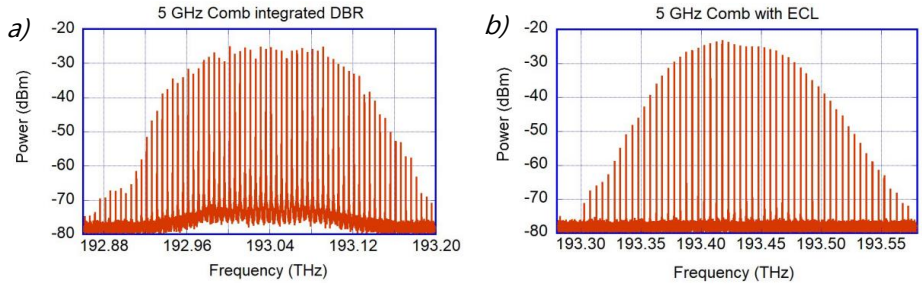

Fig. 3. Comb generation at 5 GHz with optimal electrical driving voltages and a) the on-chip DBR, b) an off-chip ECL.

4. Conclusions

We demonstrated an InP monolithically integrated tunable comb generator made by a DBR laser and a cascade of optical modulators, realized in a generic integration technology. Up to 28 tones within 5 dB power range have been obtained with repetition frequencies of a few GHz, exploiting both the integrated DBR and an ECL.

Acknowledgments

The authors would like to thank Prof. Mike Wale and Oclaro Technology Ltd for the PIC fabrication. This work has been partially supported by ACTPHAST (Access CenTer for PHotonics innovAtion Solutions and Technology Support), which is funded by the European Commission under the FP7 framework (Grant Agreement No. 619205).

References

[1] T. Udem, R. Holzwarth, and T. W. Hänsch, "Optical frequency metrology," *Nature*, vol. 416, pp. 233–237 (2002)
[2] F. Zhu et al., "Real-time dual frequency comb spectroscopy in the near infrared," *Appl. Phys. Lett.*, vol. 102 (2013)
[3] A. R. Criado et al., "Ultra narrow linewidth CW sub-THz generation using GS based OFCG and n-i-pn-i-p superlattice photomixers," *Electron. Lett.*, vol. 48, pp. 1425–1426 (2012)
[4] S. T. Cundiff and A. M. Weiner, "Optical arbitrary waveform generation," *Nature Photon.*, vol. 4, pp. 760–766 (2010)
[5] R. Wu, C. M. Long, D. E. Leaird, and A. M. Weiner, "Directly generated Gaussian-shaped optical frequency comb for microwave photonic filtering and picosecond pulse generation," *IEEE Photon. Technol. Lett.*, vol. 24, pp. 1484–1486 (2012)
[6] A. R. Criado, C. de Dios, P. Acedo, G. Carpintero, and K. Yvind, "Comparison of monolithic optical frequency comb generators based on passively mode-locked lasers for continuous wave mm-wave and sub-THz generation," *J. Lightw. Technol.*, vol. 30 (2012)
[7] T. J. Kippenberg, R. Holzwarth, and S. A. Diddams, "Microresonator-based optical frequency combs," *Science*, vol. 332 (2011)
[8] A. R. Criado et al., "VCSEL-Based Optical Frequency Combs: Toward Efficient Single-Device Comb Generation," *IEEE Photon. Technol. Lett.*, vol. 25 (2013)
[9] M. Fujiwara et al., "Optical carrier supply module using flattened optical multicarrier generation based on sinusoidal amplitude and phase hybrid modulation," *J. Lightw. Technol.*, vol. 21, pp. 2705-2714 (2003)
[10] M. K. Smit et al. "An introduction to InP-based generic integration technology," *Semiconductor Science and Technology*, vol. 29 (2014)

Radio-frequency and relative intensity noise analysis of a self mode-locked single-section quantum-dot laser

C. Weber[1]*, P. Bardella[2], L. L. Columbo[2], L. F. Lester[3], M. Gioannini[2], and S. Breuer[1]

[1]*Institut für Angewandte Physik, Technische Universität Darmstadt, Schlossgartenstraße 7, 64289 Darmstadt, Germany*
[2]*Dipartimento di Elettronica e Telecomunicazioni, Politecnico di Torino, Corso Duca degli Abruzzi 24, 10129 Torino, Italy*
[3]*Bradley Department of Electrical and Computer Engineering, Virginia Polytechnic Institute and State University, Blacksburg, Virginia 24061, USA*
**christoph.weber@physik.tu-darmstadt.de*

Summary: We investigate numerically and by experiment the radio-frequency linewidth and the integrated relative intensity noise of a single-section InAs/InGaAs quantum dot semiconductor laser. By simulations a transition from unlocked multi-mode emission to self mode-locking is predicted and experimentally confirmed by a significant reduction of the mode-beating frequency linewidth in the radio-frequency spectrum and the integrated relative intensity noise of all optical modes. In the regime of self mode-locking a radio-frequency linewidth of 20 kHz is measured. Simulations and experimental results are in good agreement.

1. Introduction

Semiconductor diode lasers (SCLs) generating optical frequency combs (OFCs) consisting of phase locked, frequency equidistant lasing modes with nearly equally distributed spectral power and low phase noise [1] are compact sources for high-data rate optical interconnections based on silicon photonics optical modulators [2], sub-THz signal generation by comb line mixing on fast photo detectors [3,4] or dual-comb spectroscopy applications with high speed and good precision [5]. Self mode-locking (SML) in single-section SCLs with active regions based on quantum-well [6], quantum-dash [7,8,9] or quantum-dot (QD) [10,11,12] material or in quantum-cascade lasers [5] without any saturable absorber has been proven to be one way to produce OFCs. Short pulses are observed either directly at the laser output facet [10] or after dispersion compensation [13]. Phase locking of the individual optical modes in SML SCLs occurs by internal nonlinear processes in the semiconductor active material, which could either be four-wave-mixing [8,9,14] or Kerr lensing [11] and are the subject of ongoing theoretical investigations. By modeling a single-section SML QD SCL using a time-domain traveling-wave (TDTW) model, the underlying physical process has been investigated and a transition from unlocked multi-mode emission to SML has been proposed [14].

2. Results and discussion

In our simulations we consider a 250-µm long single-section QD laser with a corresponding optical mode spacing frequency of 178 GHz. The laser is a ridge waveguide laser with a ridge width of 5 µm, 15 layers of QDs in the active region and a facet reflectivity of 60 %. For insight into the TDTW model and further simulation parameters, see Bardella et al. [14]. The laser under experimental investigation is a 1-mm long single-section ridge waveguide device with an active region consisting of 10 layers of InAs/InGaAs QDs. The ridge width amounts to 4 µm and the facets are as-cleaved. The laser is mounted on a copper cooling block, whose temperature is held constant at 10° C. The length of the laser corresponds to an optical mode spacing of approximately 40 GHz. Gain currents up to 400 mA are injected into the laser. The phase noise of the emitted light is analyzed using a fast photo diode and an electrical spectrum analyzer. The radio frequency (RF) beat note frequency linewidth obtained by applying a Lorentzian fit is directly correlated to the timing jitter of a semiconductor mode-locked laser [15] and an esti-

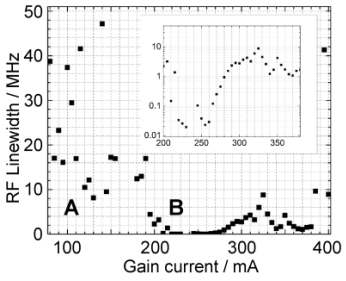

Figure 1: Experimentally estimated RF beat note linewidth as a function of gain current. A transition from unlocked optical modes (broad RF beat note) to phase-locked optical modes (small RF beat note) is observed. The inset depicts the linewidth in the phase-locked case on a logarithmic scale.

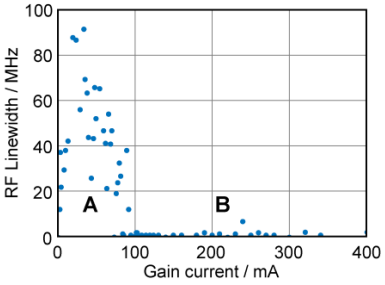

Figure 2: Simulated RF beat note linewidth as a function of gain current. As in Fig. 1, a transition to phase-locked optical modes is evident.

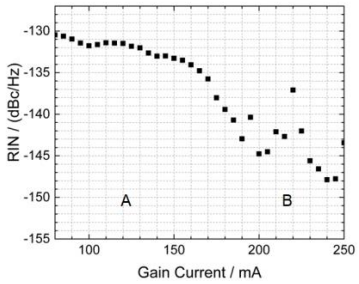

Figure 3: Experimentally measured integrated RIN (40 MHz to 50 MHz) of all modes as a function of gain current. A and B denote the locking regimes observed in the RF beat note linewidth analysis.

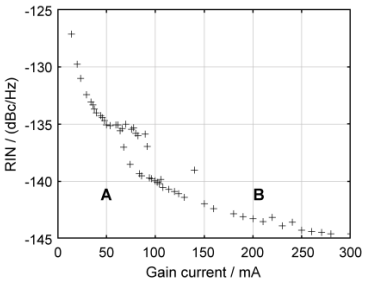

Figure 4: Simulated integrated RIN (10 MHz to 20 GHz) of all modes as a function of gain current. A and B denote the locking regimes observed in the RF beat note linewidth analysis.

mation of the phase noise of the optical frequency comb. The integrated relative intensity noise (RIN) as a measurement for amplitude fluctuations of the optical power is evaluated from 40 MHz to 50 MHz by an InGaAs photo-detector in combination with an electrical spectrum analyzer [16,17]. First, RF beat note spectra are measured for increasing gain injection current. Figure 1 and Figure 2 depict the resulting RF beat note linewidths from experiment and simulation, respectively, as a function of the gain injection current. In both Figures, two regimes can be clearly differentiated depending on the gain current. For low currents the RF beat note is very broad (two-digit MHz) whereas at a sharp transition the RF beat note is narrowed significantly to below 100 kHz in the simulations and down to 20 kHz in the experiment. The simulations suggest that at low gain current, in a first regime, the emitted light consists of several longitudinal modes without a constant phase difference in time and thus varying frequency difference between the modes. At the threshold towards a second regime, the beat note linewidth decreases significantly and the phase-difference between adjacent modes is constant as is the frequency difference. Additionally, we investigate by simulation and in the experiment the integrated RIN of all modes depending on the applied gain current. The simulated RIN is integrated from 10 MHz to 20 GHz. In the experiment the RIN is measured between 40 MHz and 50 MHz where the spectral noise density is observed to be flat. The results are depicted in Figure 3 and Figure 4. In the simulation, a significant RIN decrease at the threshold to the second regime, obtained in the experimental and simulated linewidth measurements, is evident. A RIN decrease for currents above this threshold is also confirmed by experiment.

4. Conclusions

In this work, we studied experimentally and theoretically, applying the model in [14], the RF beat note linewidth and the RIN dependencies on laser injection current. Both simulation and experiments indicated a current threshold where the optical modes appear to be phase-locked and the laser emission changes from multi-mode to SML. This threshold is characterized by a reduction of the RF beat note linewidth, with the lowest experimentally measured linewidth of 20 kHz, and a reduction of the integrated RIN. Experimentally observations are in good agreement with simulations.

5. References

[1] A. Schliesser et al., *Nature Photonics*, vol. 6, pp. 440-449, 2012.
[2] P.J. Delfyett et al., *IEEE. Journal of Lightwave Technology*, vol. 24, pp. 2701-2718, 2006.
[3] S. Koenig et al., *Nature Photonics*, vol. 7, pp. 977-981, 2013.
[4] S. Latkowski et al., *Applied Physics Letters*, vol. 92, pp. 081109, 2008.
[5] J. Faist et al., *Nanophotonics*, vol. 5, pp. 272-291, 2016.
[6] K. Sato, *Electronic Letters*, vol. 37, pp. 763-764, 2001.
[7] V. Panapakkam et al., *IEEE Journal of Quantum Electronics*, vol. 52, pp. 1-7, 2016.
[8] R. Rosales et al., *IEEE Journal of Selected Topics in Quantum Electronics*, vol. 17, pp. 1292-1301, 2011.
[9] M. Faugeron et al., *IEEE Journal of Selected Topics in Quantum Electronics*, vol. 19, pp. 1101008-1101008, 2013.
[10] J. Liu et al., *Optics Letters*, vol. 33, pp. 1702-1704, 2008.
[11] Z. G. Lu et al., *Optics Express*, vol. 16, pp. 10835-10840, 2008.
[12] S. Liu et al., *Electronic Letters*, vol 54, pp. 432-433, 2018.
[13] K. Merghem et al., *IEEE Journal of Quantum Electronics*, vol. 50, pp. 275-280, 2014.
[14] P. Bardella et al., *Optics Express*, vol. 25, pp. 26234-26252, 2017.
[15] F. Kéfélian et al., *IEEE Photonics Technology Letters*, vol 20, pp. 1405-1407, 2008.
[16] T. Gensty et al., *Optics Express*, vol. 13, pp. 2032-2039, 2005.
[17] R. Pawlus et al., *Optics Letters*, vol. 42, pp. 4259-4262, 2017.

Acknowledgements

The authors thank I. Krestnikov and his team from Innolume GmbH, Dortmund, Germany, for growing the QD wafer. Funding by the German Research Foundation and the Fondazione CRT and support by W. Elsäßer is acknowledged.

Detector-free bidirectional symmetric communication scheme based on compound states of two mutually coupled diode lasers

M. Weidmann[1], A. Herdt*[1], R. Phelan[2] and W. Elsäßer[1]

1 Technische Universität Darmstadt, Institut für Angewandte Physik, Schlossgartenstraße 7, 64289 Darmstadt, Germany
2 Eblana Photonics Ltd., 3 West Pier Business Campus, Dun Laoghaire, Co. Dublin, A96 A621 Ireland
**andreas.herdt@physik.tu-darmstadt.de*

Summary: We present a detector-free bidirectional symmetric communication scheme based on two mutually coupled 1550 nm discrete mode diode lasers. The information is encoded into compound states of the coupled laser system. The communication is established without additional detectors reading out only DC-voltage changes at both lasers under message exchange. The proof-of-principle experiment shows a good reliability demonstrated with an error-free transmission of more than 100 words.

1. Introduction

In the recent years a dramatic expansion of internet data traffic has been reported[1]. To provide high data rates in two directions via optical fibers, several methods have been developed. Most of them require both at each end a light source to transmit the data and a detector to receive the data[2]. Coupled semiconductor lasers - a system of two spatially separated nonlinear oscillators - are receiving major interest, because of a variety of interesting dynamical phenomena including chaos synchronization[3] and injection locking[4]. In order to realize a communication scheme without additional expensive detectors, i.e. the transmitter is also the receiver, we take advantage of a coupled injection locked semiconductor laser setup utilizing two 1550 nm discrete mode diode lasers (DL). In this remarkably simple scheme, the data is transmitted exploiting compound states of the coupled laser system containing upstream information of DL1 and downstream information of DL2 simultaneously. The data acquisition is accomplished by evaluating the compound state utilizing the DC-voltage change of both lasers with respect to their solitary, i.e. uncoupled voltage.

2. Experimental setup

Figure 1 schematically depicts the experimental setup with the mutually coupled 1550 nm discrete mode DLs. They are independently driven by a constant current source. The DC-voltages are individually measured by two external voltmeters. One current source, a voltmeter and one DL represent a combined receiver-transmitter (Rx / Tx) unit. The 2.25 m long coupling path contains a neutral density filter (NDF) to fine tune the coupling strength such that the injection locked DLs operate in a non-chaotic regime. For reference measurements the integrated shutter allows disconnecting the coupling path to measure the DC-voltage in non-coupled mode. With the polarization controller integrated in a 2 m fiber we provide polarization matching of both lasers. The control unit encodes the message into a series of bits using UTF-8 and transfers the bit series to the Rx / Tx units. It simultaneously receives the bit series of the Rx / Tx units and decodes them back into text.

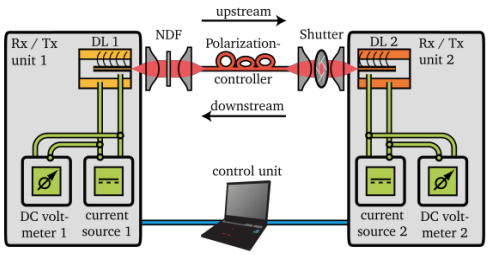

Figure 1: Schematic experimental setup showing the mutually coupled discrete mode DLs with receiver-transmitter (Rx / Tx) units (grey boxes), coupling/communication path (red) and control unit. We define traffic from Laser 1 to Laser 2 as 'upstream' and in the reverse direction as 'downstream'.

3. Communication principle

The so called locking range ΔLR is a bandwidth in the optical frequency detuning domain, where the optical frequencies of both lasers lock on a joint operation frequency ω_{op}[5] and the lasers occupy a compound state. If the lasers are driven with a constant current, the compound state causes a DC-voltage change with respect to the solitary voltage in both lasers. This voltage change can be adjusted by detuning the lasers optical frequency within the locking range, which is exemplarily visualized in Fig. 2.

To realize a unidirectional transmission from Rx / Tx unit 1 to unit 2, we set DL2 to a fixed current I_0. DL1 can either send "0" by setting its current to I_0 (i.e. $\Delta\omega_{\mathrm{op}} = 0$) or send "1" by setting its current to $I_1 > I_0$ (i.e. $\Delta\omega_{\mathrm{op}} > 0$). In these cases DL2 responds in a voltage change $\Delta U_{DL2} \simeq 0$ or $\Delta U_{DL2} < 0$. According to the keypad this yields a recovered message of "0" or "1", respectively. These voltage changes at DL2 with corresponding received bits are depicted with circles in Fig. 2a. This scenario can be interpreted as the case, where DL2 sends "0" and receives either "0" or "1" from DL1.

In the same manner it is possible to reverse the communication by interchanging DL2 with DL1 and setting the fixed current of DL1 to I_1. Therefore, this scenario represents the case, where DL1 sends "1" and receives either "0" or "1" from DL2.

With this knowledge, also a symmetric, simultaneous transmission of the bidirectional bits "00", "01", "10" and "11" can be established. The data recovery is then performed via an exclusive OR gate (XOR gate), where its first argument is the sent bit from the individual Rx / Tx unit and the second argument is a Boolean, which decides whether a voltage change at the Rx / Tx unit has been recognized or not.

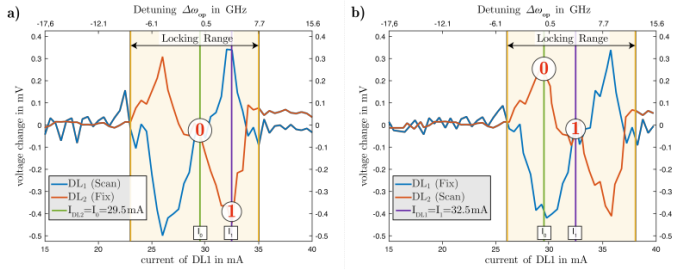

Figure 2: Exemplary voltage change of both lasers, when one DL scans its optical frequency across a fixed optical frequency of the second DL. The vertical line marks the fixed current of the DLs indicating its fixed solitary optical frequency **a)** in the case $I_{\mathrm{DL2}} = I_0$ and **b)** $I_{\mathrm{DL1}} = I_1$. The upper detuning x-axis is obtained by reference measurements of the optical spectrum of each laser operating solitarily. The detuning $\Delta\omega_{\mathrm{op}}$ is defined as the difference optical frequencies, when the DLs operate in solitary mode. The yellow area visualizes the locking range ΔLR. The circles with numbers depict the voltage change of DL2 receiving bits "0" or "1", respectively.

With this method we succeeded in transferring the words "vinorosso" in upstream direction and "pizzaiolo" in downstream direction both containing 72 bit. We found that this proof-of-principle data transmission scheme is remarkably reliable. We achieved error-free transmission for more than 100 words. The speed of the data transfer is limited in this experiment by the communication speed between control unit and current source. Therefore, the time to send a bidirectional bit amounts to 1.5s. In our setup this results in a bidirectional transmission speed of 1.3 bit/s. However, it is expected that data transmission speed can be significantly increased, because its maximum is only restricted by the time it takes to establish the compound state. This timescale is determined by the delay between the DLs (in our setup ~7.5 ns) and the internal timescales of the DLs (few ns).

4. Conclusions

We have demonstrated a detector-free bidirectional symmetric fiber-communication scheme based on two mutually coupled 1550 nm discrete mode diode lasers. It shows a remarkable reliability demonstrated with an error-free transmission of more than 100 words or 9800 bits. Using other types of semiconductor laser pairs, this proof of-principle experiment can be transferred to other wavelengths where detectors are expensive or even not available. The scheme can be significantly improved in order to perform much faster data transmission and could be applied especially for short distance transmission with nearly symmetric traffic.

5. References

[1] Index, Cisco Visual Networking. "Global mobile data traffic forecast update, 2012-2017." (2013).
[2] S. Chen et al., "Full-duplex bidirectional data transmission link using twisted lights multiplexing over 1.1-km orbital angular momentum fiber", Scientific Reports, vol. 6, 2016
[3] J. Mulet et al., "Synchronization scenario of two distant mutually coupled semiconductor lasers," Journal of Optics B-Quantum and Semiclassical Optics, vol. 6, pp. 97-105, 2004.
[4] H. Simos et al., "Intensity Noise Properties of Mid-Infrared Injection Locked Quantum Cascade Lasers: I. Modeling," IEEE Journal of Quantum Electronics, vol. 50, pp. 98-105, 2014.

Acknowledgements

Theoretical calculations for this research were conducted on the Lichtenberg high performance computer of the TU Darmstadt. Daan Lenstra for fruitful discussions on Injection Locking.

A Curved Lumped Element Electroabsorption Modulator Suitable For Flip-Chip Integration

N.P. Kelly[1]*, J. O'Callaghan[2], A. Gocalinska[2], K. Thomas[2], E. Peluchhi[2] and F.H. Peters[2]

1 Eindhoven University of Technology, Netherlands
2 Tyndall National Institute, Ireland
**n.p.kelly@tue.nl*

Summary: This work demonstrates a curved electroabsorption modulator based on a trapezoidal bend. This curved modulator design is compatible with flip-chip integration and packaging by using planar pedestal contact pads. The prototype was monolithically integrated with two DC sections to facilitate pre-packaged characterization. The device exhibited a DC optical extinction of >17 dBm over a 1 V range and an electro-optic 3 dB bandwidth of 11.75 GHz. This information was used to produce a 7.5 Gbps eye diagram, verifying the correct operation of this design. The device was fabricated using UV lithography and did not require any epitaxial regrowth.

1 Introduction

Interest in photonics integrated circuits (PICs) continues to grow due to the wide range of applications from short-distance data communications to long-haul optical transmission. Such PICs have been demonstrated using various techniques such as monolithic integration, epitaxial regrowth, quantum well intermixing and the hybrid/heterogeneous integration of InP and Si. One such hybrid approach involves the flip-chip bonding of III-V devices onto silicon substrates as outlined in [1]. InP based electroabsorption modulators (EAMs) are a key component of PICs as they offer high speed operation, a large extinction ratio and a low driving voltage. Lumped element EAMs are commonly favoured over their traveling wave counterparts for such applications due to their compact design and simpler layout. Therefore, a flip-chip compatible, lumped EAM is ideal for hybrid integration formats based on lateral coupling. Moreover, a device whose input and output were located on the same side of the chip would minimize integration complexity by simplifying the layout for optical coupling between it and the host silicon platform.

Small low loss optical waveguide bends has been identified as a critical component for achieving compact photonic devices and integrated circuits. An important consideration in designing these curved waveguides is the matching of the optical mode as it propagates through the bend. While constant curvature bends provide a short path length, they are optically lossy due to mode mismatching attributed to the abrupt change in curvature. Research has been published on the design and application of Euler bends [2], which apply a linearly changing radius of curvature to achieve low loss bends on a silicon platform. An alternative to Euler bends is a trapezoidal bend. These trapezoidal bends have a more rapid change of curvature than the equivalent Euler bend but a significantly smaller maximum curvature. This property gives the trapezoidal bend a shorter path length when applied to angles exceeding 120 degrees. A detailed geometrical description of these three bend types is given in [3].

2. Device design and characterisation

In this work, a curved electroabsorption modulator based on a trapezoidal bend is proposed and demonstrated. This lumped element EAM bends 180 degrees so that its input and output face the same direction. This alignment of the ends of the modulator results in the realization of a device which can be coupled from a single facet into a fiber or waveguide array, while maintaining a small footprint. This prototype EAM was monolithically integrated with two semiconductor optical amplifier (SOA) sections without the use of epitaxial regrowth. These sections were added to make the device compatible with our testing facilities and were lightly biased during testing to minimize absorption losses.

The device design centres around a 2.0 μm wide rib waveguide structure which penetrates through the quantum wells and into to N layers to provide high optical confinement. The EAM section is based on a 180-degree trapezoidal bend with an effective radius of curvature of 75 μm which equates to a device length of 200 μm. Two angled slots provide electrical isolation between the EAM and the adjacent 180 μm long SOA sections. The design utilizes a planar isolated pedestal GSG configuration with a pitch of 125 μm. The pedestals are electrically isolated by a trench which encircles the signal pad. These planar pedestals provide an excellent platform for flip-chip integration and packaging due to the planarization of the contacts and the ridge waveguide.
The epitaxial structure used for the EAM was based on the work reported in [4]. It contained eight compressively strained AlInGaAs quantum wells with a photoluminescence peak at 1510 nm and was grown on a semi-insulating InP substrate. A 70nm undoped AlInGaAs layer was added between the wells and the p layers to minimize valance band discontinuities, reducing photogenerated hole pile up. The quantum wells were grown on a 210 nm undoped

InGaAsP layer to create equal carrier transit times. This 420 nm think intrinsic region also reduced the capacitance of the waveguide. The fabrication process used is similar to that described in [5]. However, the signal pad was contacted to the EAM ridge by means of a bridge metal resting on Benzocyclobutene (BCB). This approach was favored over an airbridge structure which proved impractical due to the incompatibility of the required crystallographic dependent wet etch and the curved nature of the ridge design. The DC optical extinction of the device was shown to be >17 dBm over a 1 V range. An electro-optic 3dB bandwidth of 11.75 GHz was also recorded. The correct operation of this device was demonstrated by producing a 7.5 Gbps open eye diagram. Fabrication costs were minimized as the device is UV lithography compatible and does not require epitaxial regrowth.

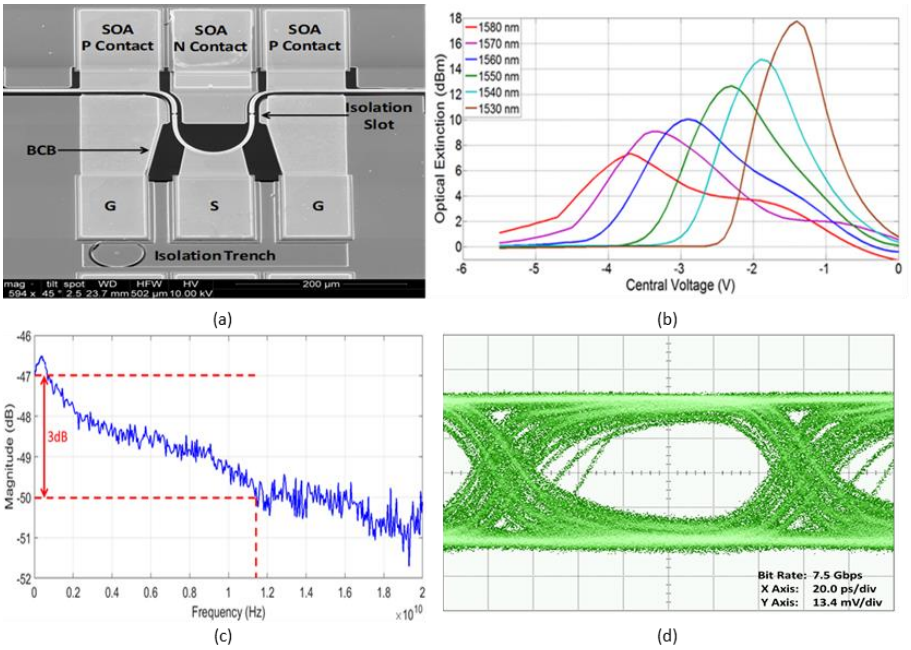

Figure 1: (a) Scanning electron microscope image of the device. (b) Optical extinction corresponding to a Vpp of 1 V for varying wavelength. (c) Electro-optic response of the electroabsorption modulator. (d) Experimentally observed 7.5 Gbps eye diagram.

4. Conclusions

This work has demonstrated a curved electroabsorption modulator based on a trapezoidal bend. The alignment of the optical input and output of this design coupled with the use of a planar isolated pedestal GSG configuration provides an excellent platform for flip-chip integration and packaging. The optical extinction and electro-optic 3 dB bandwidth were measured to be >17 dBm and 11.75 GHz respectively. The correct operation of this device was verified by producing a 7.5 Gbps eye diagram. The maximum bit rate from this device could be increased by reducing its bend radius which would shorten the device length, lowering the diode capacitance. Another possible improvement would be to reduce the parasitic capacitance of the RF pads by widening the isolation trench. The device was fabricated using UV lithography and did not require any epitaxial regrowth.

5. References

[1] S. Tanaka et al., "High-output-power, single-wavelength silicon hybrid laser using precise flip-chip bonding technology," Opt. Express, vol. 20, pp. 25057, 2012.
[2] M. Cherchi et al., "The Euler bend: paving the way for high-density integration on micron-scale semiconductor platforms," Proceedings of SPIE- The International Society for Optical Engineering 2014.
[3] R. Sheehan et al., "Bends in the Plane with Variable Curvature," Bull. Irish Math. Soc., vol. 78, pp. 61–80, 2016.
[4] C. L. M. Daunt et al., "Sub 10 ps Carrier Response Times in Electroabsorption Modulators Using Quantum Well Offsetting," IEEE J. Quantum Electron, vol. 48, pp. 1467–1475, 2012.
[5] C. L. M. Daunt et al., "Dielectric-Free Fabrication of Compact 30-GHz Photodetectors Using the Isolated Pedestal Contact Configuration" IEEE Photonics Technol. Lett., vol. 24, pp. 1082–1084, 2012.

Acknowledgements

This work was funded by Science Foundation Ireland (SFI) SFI12/RC/ 2276, SFI13/IA/1960.

Mean-field dynamics of a fully connected network of spiking neuromorphic Semiconductor lasers

Axel Dolcemascolo , Alexandre Miazek , Francesco Marino † , Romain Veltz ‡ , Stéphane Barland

Université Côte d'Azur-CNRS INPHYNI, 1361 route des Lucioles, Valbonne, France
† CNR - Istituto Nazionale di Ottica largo E. Fermi 6, I-50125 Firenze, Italy
‡ Université Côte d'Azur-INRIA MathNeuro Team, 2004 Route des Lucioles-BP 93, 06902, Sophia Antipolis, France

Summary: We analyze experimentally and theoretically the dynamics of an ensemble of about five hundred coupled spiking elements. We show that the fully connected network can behave as a low dimensional chaotic system.

1 Introduction

The collective behavior of large ensemble of chaotic or spiking systems is a key question in many fields of research in- cluding neurosciences, for instance through the many debates on the role of synchronization in epilepsy [1]. Fortunately, in some cases, it is possible to analytically reduce the dimension- ality of such complex systems and to analyze their collective dynamics via a considerably simpler mean field model (see e.g. [2], [3], [4]). In spite of these remarkable theoretical achievements though, actual experiments demonstrating exam- ples of reduced dimensionality dynamics are very rare. In this contribution, we analyse experimentally and theoretically a toy complex dynamical system consisting of hundreds of spiking optical devices, each of them mimicking the dynamics of chaotically spiking neurons [5]. We measure the bifurcations undergone by the fully connected network and demonstrate experimentally and analytically that the global behavior can be described to an excellent approximation with a model of much lower dimensionality.

2 Results

In this study we investigate an optical experiment in which a large number of semiconductor lasers are coupled from one- to-all to fully connected network configurations. This is an analogous experiment to having a fully connected network of spiking neurons, where the spikes are in the intensity of the emitted laser light. We achieve this global coupling by means of an electrical feedback loop: the intensity of the light emitted by a laser is re-injected into the laser control parameter via an optical to electrical converter and a nonlinear function. It was already shown that with such a feedback with one single laser it is possible to obtain a sequence of slow chaotic spiking as a result of an incomplete homoclinic scenario to a saddle-focus, where an exact homoclinic connection does not occur. This is due to the coexistence of three different characteristic time scales, which span about five orders of magnitude. Here we expand our population to about 500 semiconductor lasers and we study the emergence of chaos and synchronization when the order parameter of one laser drives the whole population (one to all coupling) and when the sum of several or even all laser signals drives the common bifurcation parameter of the array. In particular, we analyse the statistical distribution of laser intensity of sub-ensembles of the whole array depending on the region of the chaotic attractor which is considered and on control parameters such as the coupling strength and the operating point of the whole array. We also observe and characterize complex sequences of mixed-mode oscillations. Finally we are able to reproduce the experimental results with numerical simulations and analytic study of a detailed physical model of the laser spiking network, where the dynamics of each node is described in terms of (single- mode) semiconductor-laser rate equations and the coupling mechanism is provided by a common AC-coupled nonlinear feedback loop. Starting from this model, we derive and discuss the reduction of the dynamics to that of a simplified mean field model, which is able to well replicate and explain the behaviour of the whole population.

3 References

[1] P. Jiruska, M. de Curtis, J. G. Jefferys, C. A. Schevon, S. J. Schiff, and K. Schindler, "Synchronization and desynchronization in epilepsy: controversies and hypotheses," The Journal of physiology, vol. 591, no. 4, pp. 787–797, 2013.

[2] E. Ott and T. M. Antonsen, "Low dimensional behavior of large systems of globally coupled oscillators," Chaos: An Interdisciplinary Journal of Nonlinear Science, vol. 18, no. 3, p. 037113, 2008.

[3] D. Pazó and E. Montbrió, “From quasiperiodic partial synchronization to collective chaos in populations of inhibitory neurons with delay,” Physical review letters, vol. 116, no. 23, p. 238101, 2016.

[4] S. Chandra, D. Hathcock, K. Crain, T. M. Antonsen, M. Girvan, and E. Ott, “Modeling the network dynamics of pulse-coupled neurons,” Chaos: An Interdisciplinary Journal of Nonlinear Science, vol. 27, no. 3, p. 033102, 2017.

[5] K. Al-Naimee, F. Marino, M. Ciszak, R. Meucci, and F. T. Arecchi, “Chaotic spiking and incomplete homoclinic scenarios in semiconductor lasers with optoelectronic feedback,” New Journal of Physics, vol. 11, no. 7, p. 073022, 2009.

Optical frequency comb generation from semiconductor lasers using pulsed excitation and optical injection

A. Rosado[1]*, A. Pérez-Serrano[1], J.M.G Tijero[1], A. Valle[2], L. Pesquera[2] and I. Esquivias[1]

1. CEMDATIC-E.T.S.I. Telecomunicación, Universidad Politécnica de Madrid (UPM), 28040, Madrid, Spain
2. Instituto de Física de Cantabria, (CSIC-Universidad de Cantabria), 39005 Santander, Spain
**alejandro.rosado@upm.es*

Summary: We report on the generation of broad and flat Optical Frequency Combs in an optically injected 1550 nm laser diode using gain switching with pulsed excitation. Short optical pulses (40 ps) at a repetition frequency of 500 MHz are obtained, showing a low noise optical spectrum with 80 tones within 10 dB.

1. Introduction

An Optical Frequency Comb (OFC) Generator is a laser source emitting an equally spaced group of optical frequencies. OFCs have been used in numerous fields, such as optical communications [1], RF photonics [2] and infrared spectroscopy [3]. Relatively low repetition rate OFCs (100-1000 MHz) are specially suited for dual comb spectroscopic applications. OFC generation in semiconductor lasers can be achieved by different techniques, i.e., gain switching (GS), mode-locking and electro-optic external modulation [1]. Low repetition rate OFCs from GS semiconductor lasers using sinusoidal excitation have been reported for spectroscopic applications [4]. On the other hand, pulsed excitation GS has demonstrated ultra-short optical pulses [5], but, as far as we know, it has not been used for OFC generation. We have recently reported an experimental evaluation of the quality of OFC generated from GS semiconductor laser with and without Optical Injection (OI) [6]. In this work, we consider pulsed excitation to generate low repetition rate OFCs, and we demonstrate a high performance in terms of noise, flatness and bandwidth, for an optical-injected 1550 nm laser diode.

2. Experimental Setup

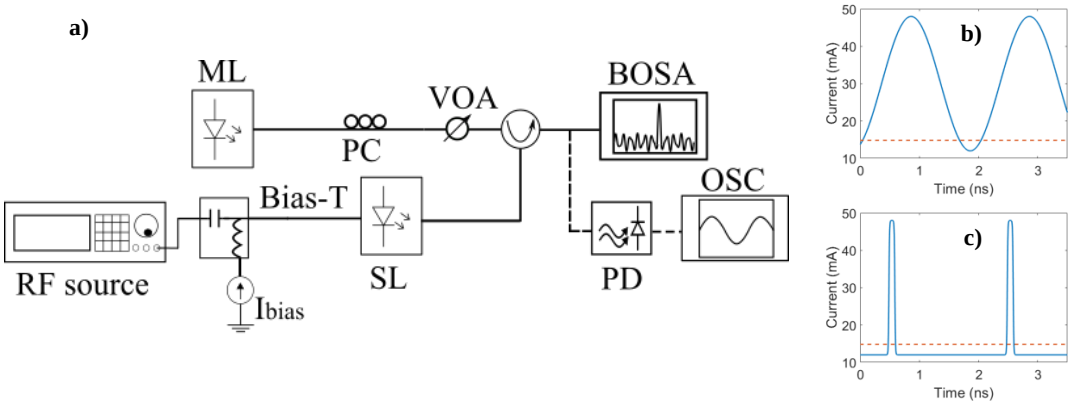

Figure 1. a) Schematics of the experimental setup. ML: Master Laser, SL: Slave Laser, PC: Polarization Controller, VOA: Variable Optical Attenuator, PD: Photodetector, OSC: Oscilloscope, BOSA: Brillouin Optical Spectrum Analyzer. Estimated total current though the SL under b) sinusoidal excitation and c) pulsed excitation. The red dotted line is the threshold current.

The experimental setup is shown in Fig. 1a). The OFC generator is based on a typical master-slave scheme. The master laser is a tunable laser which can be tuned along the C-Band with a linewidth ~ 75 kHz. The Slave Laser (SL), a Discrete Mode Laser (DML), is driven in GS operation using a combination of two signals: a bias current and, either a sinusoidal signal provided by a microwave/RF generator, or a 5% duty cycle square signal provided by a pulse pattern generator (Fig. 1c)). The repetition frequency is 500 MHz. The estimated temporal evolution of the injected current, calculated taking into account the input impedance of the laser [6] is shown in Figs. 1b) and 1c) for sinusoidal and pulsed excitation, respectively.

3. Results and discussion

Fig. 2 shows the temporal and the spectral responses of the laser under different regimes of operation. The temporal trace in Fig. 2a) corresponds to sinusoidal excitation without OI. In the lowest part of the negative cycle of the sinusoidal signal, the instantaneous current lays below threshold and the laser is switched off; when

the current rises above threshold an initial spike corresponding to GS can be observed, followed by a sinusoidal-like profile in which features reminiscent of the relaxation oscillations are apparent. The corresponding optical spectrum (Fig. 2d)) is not an OFC. As we reported in [6] at this repetition frequency OFCs appear only if the laser is not switched-off, i.e., under direct modulation conditions. Under pulsed excitation without OI a short optical pulse is generated (45 ps at Full Width Half Maximum FWHM), as is shown in Fig. 2b). The optical spectrum (Fig. 2e)) is wide and continuous without any discernible peaks, i.e., it is not an OFC. This is due to the lack of coherence between pulses, as each pulse is built-up from spontaneously emitted photons with random initial phases. Fig. 2c) corresponds to pulsed excitation with OI; it shows short optical pulses (40 ps at FWHM) similar to those of Fig. 2b). In this case, a broad and flat OFC is obtained (Fig. 2f)). This effect is due to the OI, as the externally injected photons are acting as the seed for the GS pulses, providing a common phase and therefore coherent emission. The OFC in Fig. 2f) has a very high Carrier to Noise Ratio (CNR), around 34 dB, and 80 tones within 10 dB, a factor 10 in comparison with the best value measured at this repetition frequency with sinusoidal excitation [6]. Furthermore, the flatness at 3 dB reaches 44 tones, indicating promising properties for spectroscopic applications.

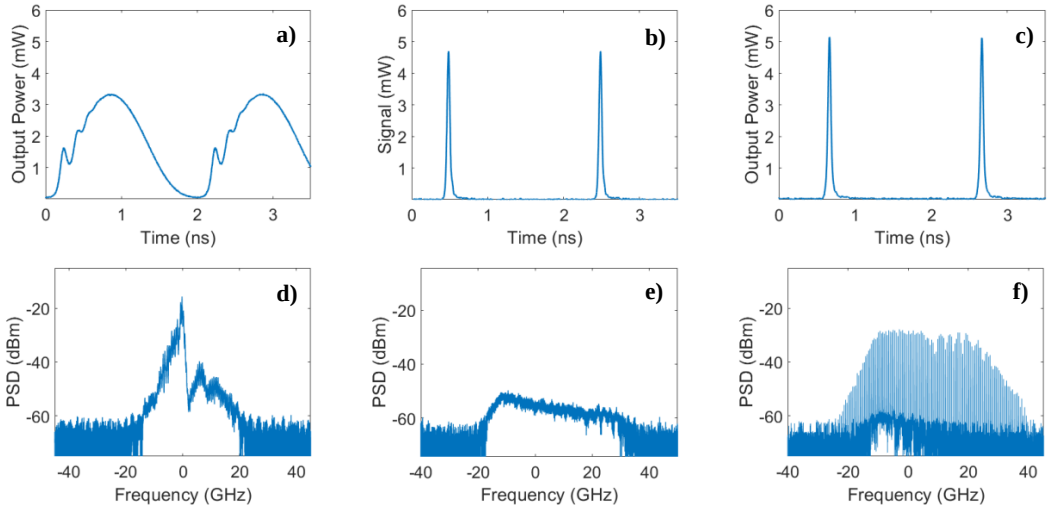

Figure 2. Temporal traces (upper row) and optical spectra (lower row) of the SL for different regimes of operation: a) and d): Sinusoidal excitation without OI; b) and e): Pulsed excitation without OI; c) and f): Pulsed excitation with OI.

4. Conclusions

Gain switching with pulsed excitation in combination with optical injection is demonstrated as an excellent technique to generate broad and flat OFCs with a relatively low repetition rate.

5. References

[1] Imran, M., Anandarajah, P. M., Kaszubowska-Anandarajah, A., Sambo, N., & Potí, L. "A survey of optical carrier generation techniques for terabit capacity elastic optical networks". IEEE Commun. Surv. Tutor., 20(1), 211-263, 2018.
[2] Torres-Company, V., & Weiner, A. M. "Optical frequency comb technology for ultra-broadband radio-frequency photonics". Laser. Photon. Rev., vol. 8, no. 3, pp. 368-393, 2014.
[3] Coddington, I., Newbury, N., & Swann, W. "Dual-comb spectroscopy". Optica, vol. 3, no. 4, pp. 414-426, 2016.
[4] Jerez, B., Martín-Mateos, P., Prior, E., de Dios, C., & Acedo, P. "Dual optical frequency comb architecture with capabilities from visible to mid-infrared". Opt. Exp., 24(13), 14986-14994, 2016.
[5] Chen, S., Yoshita, M., Sato, A., Ito, T., Akiyama, H., & Yokoyama, H., "Dynamics of short-pulse generation via spectral filtering from intensely excited gain-switched 1.55-μm distributed-feedback laser diodes". Opt. Exp., 21(9), 10597-10605, 2013.
[6] Rosado, A., Perez-Serrano, A., G. Tijero, J. M., Valle, A., Pesquera, L. & Esquivias, I., "Experimental study of optical frequency comb generation in gain-switched semiconductor lasers" Opt. Laser Technol., 108, 542-550, 2018

Acknowledgements

This work was funded by the Ministerio de Economia y Competitividad of Spain (COMBINA, TEC201565212-C3). A.R., A.P., J.M.G.T. and I.E. acknowledge support from Comunidad de Madrid (SINFOTON-CM, S2013/MIT-2790).

Dual-cavity optical self-feedback stabilization of a passively mode-locked quantum-well laser

Dominik Auth[1]*, Christoph Weber[1], Andreas Klehr[2], Andrea Knigge[2] and Stefan Breuer[1]

1 Institut für Angewandte Physik, Technische Universität Darmstadt, 64289 Darmstadt, Germany
2 Ferdinand-Braun-Institut, Leibniz-Institut für Höchstfrequenztechnik, 12489 Berlin, Germany
**dominik.auth@physik.tu-darmstadt.de*

Summary: Dual-cavity optical self-feedback stabilization of a monolithic passively mode-locked quantum-well laser is demonstrated. A long optical feedback cavity allows for reduction of the timing jitter to 330 as. Simultaneously, a short optical feedback cavity allows to tune the repetition rate by 1 GHz. Additionally, a complete radio-frequency sideband suppression is achieved.

1 Introduction

Monolithic passively mode-locked (PML) semiconductor lasers (SCL) with multi-GHz repetition rates (RR) emitting at wavelengths of around 1070 nm are attractive ultrafast sources for seeding ytterbium doped fiber amplifiers and for photonic communication at high data rates [1]. For these applications a low pulse train timing jitter (TJ) and a high amplitude stability as well as a broad RR tuning range of the emitted pulse train are necessary. In the emission wavelength range around 1070 nm, TJ and amplitude stability analysis for PML quantum-well (QW) lasers [2], modeling the impact of single cavity optical feedback (OFB) on the pulse train stabilization by a time-domain stochastic model [3] and RR tuning range dependencies on the OFB cavity length [4] were studied. To improve the TJ, self-feedback of the pulsed laser emission by an external-cavity OFB configuration can be explored on monolithic PML SCL [5]. Dual-cavity (DC) OFB has been investigated in [6, 7] and it was found to substantially reduce sidebands around the RR, induced by single cavity OFB. In this contribution, we experimentally study the impact of DC OFB by two fine-delay controlled optical cavities on the pulse RR and the TJ of a PML QW SCL emitting at 1070 nm in dependence on the OFB strength as well as the feedback delay.

2. QW Laser and DC OFB Set-up

The investigated PML QW laser is a monolithic multi-section ridge waveguide laser consisting of 30 individual 100 µm long electrically isolated sections with a ridge width of 4 µm. Individual sections are electrically connected to form one long gain and one absorber section, with a saturable absorber length amounting to 10% of the total cavity length. The active region consists of an InGaAs double QW structure embedded in GaAsP spacer layers. The facets are as-cleaved. At a gain current of 300 mA, an absorber reverse bias voltage of -1.2 V and a laser cooling block temperature of 20°C, the laser emits at a RR of 13.6 GHz and exhibits a pulse to pulse TJ of 83 fs obtained from the radio-frequency line-width [8]. The pulse width amounts to 8 ps. The developed DC OFB set-up is depicted in Figure 1. Two external cavities are chosen consisting of a very short free space cavity (1 - 2 times the optical laser cavity length) to achieve a broad RR tuning range [4] realized by a glass plate with a wedged back-surface mounted on a high-precision linear translation stage and a long fiber-based cavity (L_{mac} = 5.9 m) for improved TJ reduction. Another benefit of this DC OFB configuration in comparison to a single cavity OFB set-up is the capability of a complete suppression of noise-induced sidebands by the external OFB cavities.

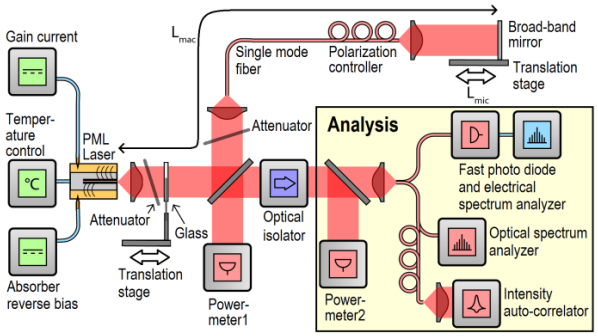

Figure 1: OFB set-up consisting of one short-cavity OFB arm composed of a semi-transparent glass and a long-cavity fiber-based OFB arm. The OFB strength is fine-controlled by variable attenuators based on neutral density filters.

3. Experimental Results & Discussion

The DC OFB configuration allows for a fundamental RR tuning range from 12.7 GHz to 13.9 GHz thus exceeding 1 GHz. A minimum pulse to pulse TJ of 330 as and complete sideband suppression is demonstrated

which constitutes an improvement by a factor 250 as compared to the laser without OFB. The RR tuning by the DC OFB set-up is depicted in Figure 2a colour coded as a function of both OFB fine-delay lengths. A horizontal and a vertical cut through the experimental map shows the influence of both OFB cavities on the RR. The short OFB cavity mainly determines the RR and also the transitions to higher harmonic mode-locking orders (HMLO) [9] depicted as white regime in Figure 2a. The laser can be tuned to the fourth HMLO which corresponds to a RR of 54.4 GHz. Intensity auto-correlation (AC) traces for a HMLO of 1,2,3 and 4 are given in Figure 2b. At particular settings in the fundamental mode-locking regime a full sideband suppression in the radio-frequency spectrum around the main RR line is achieved. Exemplary timing phase noise power spectral densities (TPN PSD) [3] are given in Figure 3. The orange curve shows non-ideal DC OFB settings with low sideband suppression and only a moderate TJ reduction. The red curve shows a considerable reduction in the TPN PSD and thus a high TJ reduction down to 330 as. Additionally a full sideband suppression is achieved.

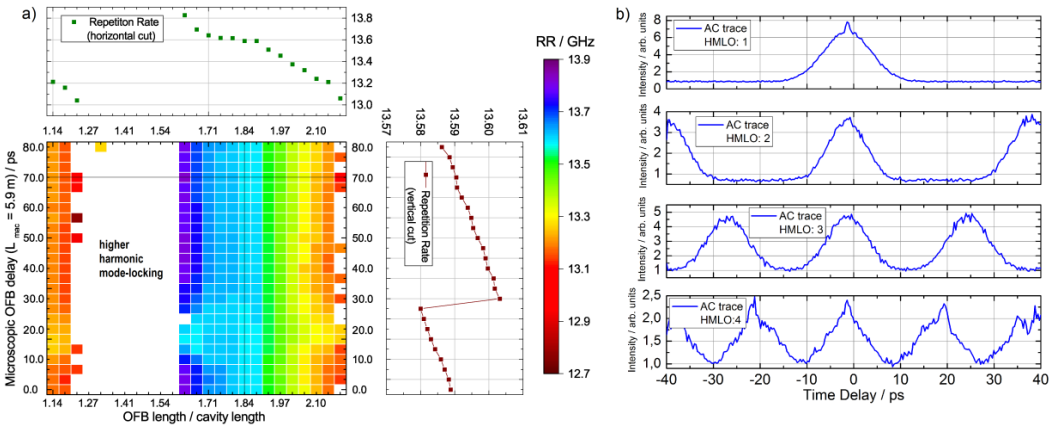

Figure 2: a) Repetition rate tuning for the DC OFB set-up. An overall tuning range exceeding 1 GHz is obtained. On the right, a vertical cut and on the top, a horizontal cut through the repetition rate map is depicted. b) AC traces for different HMLO.

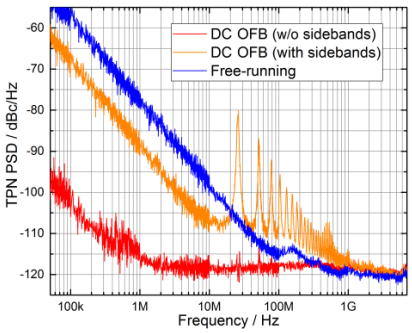

Figure 3: Exemplary TPN PSD spectra for DC OFB and in free-running operation.

4. Conclusions

In summary, a TJ reduction to 330 as and complete radio-frequency sideband suppression is achieved for a PML QW laser emitting at a RR of 13.6 GHz by DC OFB. The RR tuning range exceeds 1 GHz.

5. References

[1] Yamamoto, N., Sotobayashi, H., Akahane, K., et al., *Optics Express* **16(24)**, 19836-19843 (2008)
[2] Weber, C., Klehr, A., Knigge, A., et al., *IEEE Journal of Quantum Electronics* **54(3)**, 1-9 (2018)
[3] Drzewietzki, L., Breuer, S., and Elsäßer, W., *Optics Express* **21(13)**, 16142-16161 (2013)
[4] Auth, D., Drzewietzki, L., Weber, C., et al., *Electronics Letters* **54(6)**, 374-376 (2018)
[5] Rauch, S., Drzewietzki, L., Klehr, A., et al., *IEEE Journal of Quantum Electronics* **51(4)**, 1–7 (2015)
[6] Haji, M., Hou, L., Kelly, A. E., et al., *Optics Express* **20(3)**, 3268-3274 (2012)
[7] Nikiforov, O., Jaurigue, L., Drzewietzki, L.,et al., *Optics Express* **24(13)**, 14301-14310 (2016)
[8] Kefelian, F., O'Donoghue, S., Todaro, M. T., et al., *IEEE Photonics Technology Letters* **20(16)**, 1405-1407 (2008)
[9] Jaurigue, L., Krauskopf, B., Lüdge, K, *Chaos: An Interdisciplinary Journal of Nonlinear Science* **27(11)**, 114301 (2017)

Acknowledgements

Funding by the German Research Foundation and the TU Darmstadt (program: Ingenium) and support by W. Elsäßer is acknowledged.

Experimental characterization of transitions between locking regimes in a semiconductor laser with optical feedback and small amplitude current modulation

J. Tiana-Alsina, Carlos Quintero-Quiroz, M. C. Torrent and Cristina Masoller*

Departamento de Fisica, Universitat Politecnica de Catalunya, St. Nebridi 22, Terrassa 08222, Barcelona, Spain
**cristina.masoller@upc.edu*

Summary: We study entrainment in a semiconductor laser with optical feedback, operated in the regime where the laser randomly emits abrupt spikes. To quantify the quality of the entrainment of the optical spikes to periodic, small-amplitude pump current perturbations we use the success rate (SR) and the false positive rate (FPR). The SR counts the spikes that occur within a short time window after each perturbation, and the FPR counts the additional spikes that occur outside the window. We uncover parameter regions where the electric perturbations fully control the optical spikes, entraining them, such that the laser emits, shortly after each perturbation, one and only one spike (i.e., SR=1 and FPR=0). We also characterize the locking-unlocking transitions when the perturbation amplitude and frequency vary.

1 Introduction

The entrainment (or locking) phenomenon, by which an oscillator adapts its natural rhythm to an external periodic signal, is well-known in physics, chemistry, biology, etc. [1]; however, controlling an stochastic nonlinear system with a small-amplitude signal is a challenging task, and systems that allow for low-cost experiments are scarce. Here we study experimentally the entrainment of a semiconductor laser with optical feedback in the low frequency fluctuations (LFF) regime, to a weak external signal directly applied to the laser current. In the LFF regime the laser emits a spiking output: during a spike the intensity drops abruptly and then recovers gradually. The parameter region where the LFF regime occurs is quite wide, and includes a sub-region where the emitted spikes are consistent with events seeded by noise [2]. In this region, we aim to control the spikes via periodic, small-amplitude electric perturbations of the laser pump current.

To quantify the degree of entrainment we use receiver operating characteristic (ROC) curves obtained by plotting the success rate (SR, that counts the spikes that occur within a short time window after each perturbation) vs. the false positive rate (FPR, that counts the additional spikes that occur outside the window). ROC curves, first developed during World World II for detecting enemy objects, allow to quantify the diagnostic ability of a binary classifier as a function of its classification threshold, and are nowadays routinely used in machine learning algorithms.

2. Experimental setup and method of analysis

The experimental setup is as described in [3, 4]. A 685 nm semiconductor laser (Thorlabs HL6750MG) with feedback from an external cavity (7:2% threshold reduction, delay 5 ns) is modulated by using a function generator (Agilent 81150) and its output is sent to a photo-detector, an amplifier and a digital storage oscilloscope. The bandwidth of the dectection system is 1 GHz. Pulse-down periodic perturbations are applied to the laser current. The control parameters are the perturbation amplitude, frequency, and the dc value of the laser current, which controls the natural frequency of the spikes. For each set of parameters, 10^7 data points are recorded with 2 GS/s sampling rate, which allow to capture the intensity dynamics during 5 ms.

The intensity dynamics is characterised by the SR and the FPR. The SR measures the response of the laser per perturbation cycle: if the laser emits one spike after each perturbation, SR=1, if it emits one spike every two perturbations, SR=1/2, etc. Only spikes emitted within a detection window of duration τ = 15 ns are considered as spikes induced by the perturbation (the length of the window is chosen such that only one spike can be emitted within the window). The FPR measures the spikes which are emitted outside this window. FPR=0 indicates that the spikes are always emitted within the time interval τ after a perturbation, while FPR=1 indicates that the laser does not emit any spike within this time interval.

3. Results

Figure 1 displays typical examples of the intensity dynamics when the laser current is not perturbed (panel a), and when it is periodically perturbed (panels b-c) with 2.3% of the current dc value, and different perturbation frequencies. In panel (b) the frequency of the perturbations is lower than the natural frequency of the spikes and it is observed that after each perturbation the laser emits a spike, but in between perturbations the natural dynamics prevails and thus, most of the spikes are spontaneous (false positives). For a higher frequency, panel (c), locking 1:1 is observed since every perturbation triggers a spike. For a higher frequency, panel (d),

there is a transition between locking 1:1 and 2:1. In this region the spikes cannot follow the fast external perturbations and some spikes are delayed with respect to the perturbations. By further increasing the perturbation frequency, the spike rate adjusts such that there is one spike every two perturbations, panel (e).

Panel (f) displays the ROC curve that characterizes the transition to locking 1:1 when the perturbation amplitude is increased while the frequency is kept constant (14 MHz). We note that we reach perfect 1:1 locking (SR=1 and FPR =0) for a perturbation amplitude of 2.4%. Panel (g) displays the ROC curve for the transition when the perturbation frequency grows while the amplitude is kept constant (2.4%). Here, the transition from SR=1 and FPR=0 to SR=1/2 and FPR=0, as well as the transition from SR=1/2 and FPR=0 to SR=1/3 and FPR=0 are observed. During the transition from one locking regime to another, there is an increase of the number of false positives, followed by a decrease. The increase is due to the re-organization of the spikes: they cannot follow the external signal as it becomes faster, but, on the other hand, two periods of the signal is a too long time interval for only one spike.

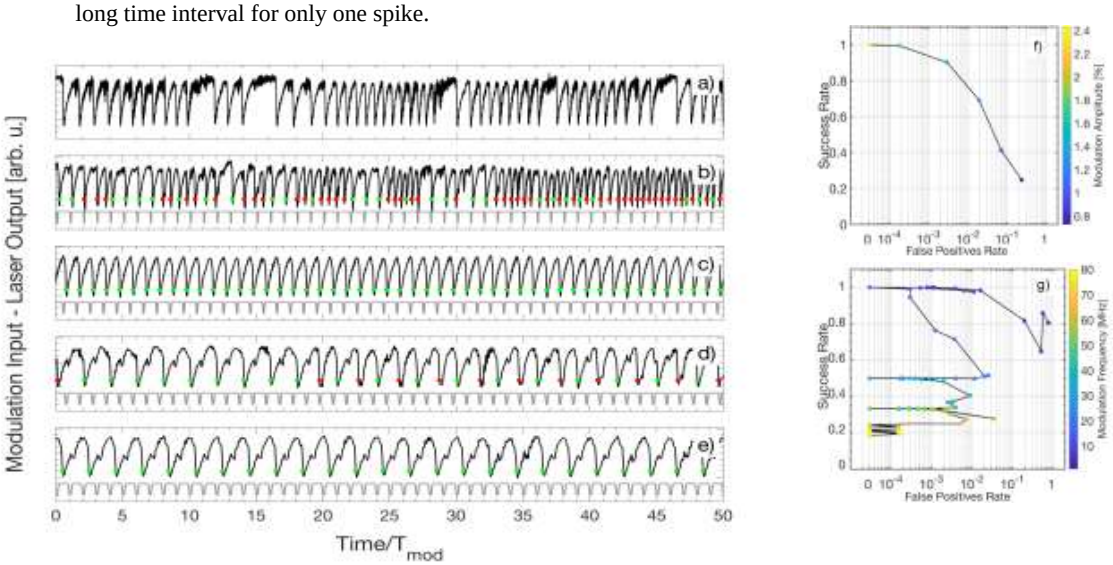

Figure 1. (a)-(d): Current perturbation (gray) and laser output intensity (black) vs. time. The green dots represent the spikes that occur shortly after a perturbation, while red dots mark the spikes that are considered not entrained to the current perturbations. Panel (a) shows the unforced dynamics; (b) shows the dynamics at low perturbation frequency (10 MHz); the perturbation amplitude is 2.3% of the current dc value. Panels (c), (e) display locking 1:1 and 2:1 for 20 MHz and 41 MHz respectively; panel (d) shows the transition between locking 1:1 and 2:1 observed at 30 MHz. The ROC curves in panels (f) and (g) allow tracking the transition to locking when (f) the perturbation amplitude increases (in color scale) or when (g) the perturbation frequency increases (in color scale). To represent in logarithmic scale the value FPR=0 we have set it to a small value (labeled as 0 in the x-axis)

4. Conclusions

We have proposed a novel technique, based on the ROC curve, to quantify the degree of entrainment of the laser spikes to the electric current perturbations. We have identified operation conditions such that the success rate (the number of spikes per perturbation cycle), is equal to 1, 1/2 or 1/3, while the false positive rate (the number of spikes which are not triggered by a perturbation), is equal to zero. Using the ROC curves we have uncovered different types of transitions: when the amplitude is increased there is a gradual transition to locked behavior, while when the frequency is increased, there are rather abrupt locked-unlocked transitions.

5. References

[1] A. Pikovsky, M. Rosenblum, J. Kurths, *Synchronization: a universal concept in nonlinear sciences* (Cambridge University Press, 2003).
[2] C. Quintero-Quiroz, J. Tiana-Alsina, J. Roma, M. C. Torrent, and C. Masoller, Sci. Rep. 6, 37510 (2016).
[3] J. Tiana-Alsina, C. Quintero-Quiroz, M. Panozzo, M. Torrent, and C. Masoller, Opt. Express 26, 9298 (2018).
[4] J. Tiana-Alsina, C. Quintero-Quiroz, M. Torrent, and C. Masoller, arXiv 1806.08950 (2018).

Acknowledgements

This work was supported in part by Spanish MINECO/FEDER (FIS2015-66503-C3-2-P). C. M. also acknowledges partial support from ICREA ACADEMIA, Generalitat de Catalunya.

Novel excitability and canard explosions in optically injected quantum dot lasers

M. Dillane[1,2], D. Goulding[2,3] I. Dubinkin[4], N. Federov[4], E.A. Viktorov[4,5] and B. Kelleher[1,2]

[1]*Dept. of Physics, University College Cork, College Road, Cork, Ireland*
[2]*Tyndall National Institute, Lee Maltings, Dyke Parade, Cork, Ireland*
[3]*CAPPA and Department of Mathematics, Cork Institute of Technology, Bishopstown, Cork, Ireland*
[4]*ITMO, St. Petersburg, Russia*
[5]Optique Nonlinéaire Théorique, Campus Plaine, CP 231, 1050, Bruxelles, Belgium

**Michael.dillane @tyndall.ie*

Summary: Optically injected quantum dot lasers are rich in non-linear dynamics and specifically of excitable phenomena. By varying 3 the control parameters - injection strength, detuning and pump current - multiple regimes of excitability can be found. Typical Type I regimes are observed. Type II behaviour can also be observed in this system and we show here that it arises from a canard explosion. We show that by utilising the unique ability of quantum dot lasers to lase from the first excited state, a new form of Type I excitability is obtained, which does not display accompanying 2π phase slips.

1 Introduction

InAs based Quantum Dot (QD) lasers have the unique ability among semiconductor lasers to lase from several distinct energy states. In particular, they can emit from the ground state (GS), the first excited state (ES) and simultaneously from both (SIM). Due to their inherent high damping of the relaxation oscillations, QDLs are also incredibly stable under external optical feedback and optical injection. Together, the two state lasing and enhanced stability lead to several novel regimes of non-linear dynamics and in particular, excitability.

Here we are concerned with unidirectional optical injection. A commercially available tunable laser acted as the master (ML) for the QD slave laser. Each of the three free-running regimes (GS, SIM and ES) were analysed under injection. In each case, regardless of the operating parameters, it was the GS that was injected. That is, the ML frequency was close to the GS. Even in the SIM and ES lasing regimes, for low detuning and weak injection, the ES could be completely suppressed and phase locked lasing from the GS only could be obtained.

2. Ground state only phenomena

For the GS only regime, both Type I and Type II excitability can be observed, depending on the injection strength. The Type I Adler-like regions are well known and have been well discussed in the literature [1-4] These Adler like pulses can be seen for both positive and negative detuning in the case of QD lasers. The Type II behaviour in this configuration has more recently been reported and is observed only with QD lasers. It relies on a hitherto unobserved optothermal coupling that leads to a square wave output. Theoretical models predict a bistability to exist in this region [2]. However, due to thermal effects, the bistability is broken and a deterministic cycle is instead found as shown in Fig. 1. The square wave regime is found to emerge from a canard explosion, the first observation of the phenomenon in this laser configuration.

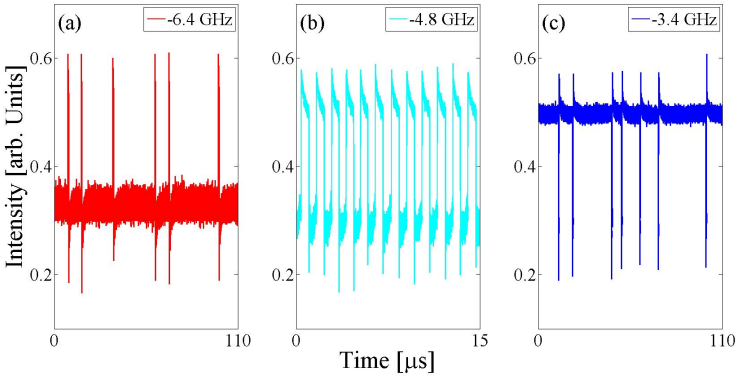

Figure 1: GS only high injection. (a) shows a non-periodic square pulse train, (b) shows a period square pulse train and (c) shows a non-periodic train of square dropouts.

3. Dual state phenomena

By operating the slave laser in the ES only but injecting at the GS frequency, novel dynamics can be obtained. For high injection strengths, optothermal coupling again arises and leads to extremely long lived antiphase, controllable bursting oscillations and slow passage effects as reported in [5]. Here we show that for low injection levels in this configuration, Type I excitability is obtained but of a never before seen, non-Adler variety. We show here a dual state excitability manifested by GS intensity dropouts of several ns duration accompanied by ES pulses shorter than 100 ps. The phase of these GS dropouts was obtained and shown to differ from the well-known 2π phase slips of the standard GS only injection configuration. Instead, the phase is bounded in this system. Further, there is evidence of a saddle focus in the phase trajectory leading to ringing oscillations in the GS dropout.

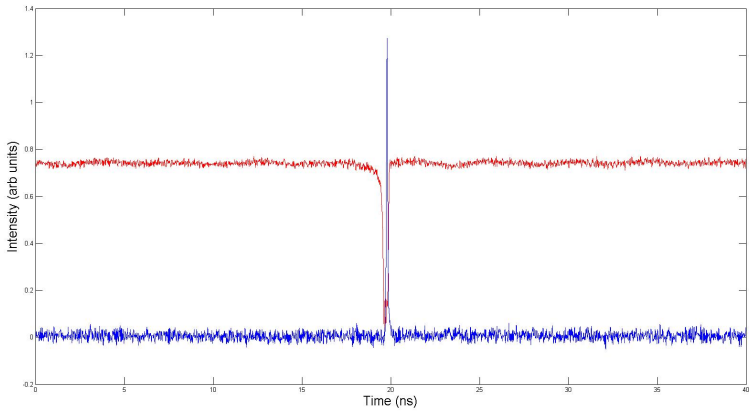

Figure 2: Non-Adler behaviour. The blue trace shows the ES intensity and the excitable pulse. The red trace shows the GS intensity with the corresponding drop out.

The excitable regimes found with QDLs are of great interest for neuromorphic studies – a multidisciplinary field of growing interest. Their ability to reproduce such a wide range of neuronal phenomena is unique and preliminary studies suggest that small networks of such devices could lead to stable, information processing units.

4. References

[1] S. Wieczorek, B. Krauskopf and D. Lenstra, Phys. Rev. Lett. **88**, 063901 (2002).
[2] T. Erneux, E. Viktorov, B. Kelleher, D. Goulding, S. Hegarty and G. Huyet, Opt. Lett. **35**, 937 (2010).
[3] B. Kelleher, C. Bonatto, G. Huyet and S.P. Hegarty, Phys. Rev. E **83**, 026207 (2011).
[4] B. Kelleher, D. Goulding, S.P. Hegarty, G. Huyet, D.-Y. Cong, A. Martinez, A. Lemaître, A. Ramdane, M. Fischer, F. Gerschütz and J. Koeth Opt. Lett **34**, 440 (2009).
[5] B. Kelleher, B. Tykalewicz, D. Goulding, N. Fedorov, I. Dubinkin, T. Erneux, E.A. Viktorov, Sci. Rep. **7**, 8414 (2017).

Multi-wavelength Analysis of Synthetic Tissue Samples by Optical Feedback Interferometry

M. Dabbicco*, M.C. Cardilli

Dipartimento Interuniversitario di Fisica "M. Merlin", Università degli Studi di Bari "Aldo Moro" and CNR-IFN, UOS Bari, via Amendola 173, 70126 Bari, Italy
**maurizio.dabbicco@uniba.it*

Summary: Optical feedback interferometry is being increasingly applied to imaging of both inorganic and organic samples, especially in the infrared spectral region where imaging detectors are expensive or bulky. We present an attempt to apply optical feedback interferometry (OFI) to multispectral analysis of polydimethylsiloxane (PDMS) with organic (starch) inclusions, covering the near- and mid-infrared spectrum. Absorption at the amide-I band in the MIR range, resulted in discriminating different starch concentration by OFI, whereas at the near infrared wavelengths, where the starch is not absorptive, OFI reported congruent signal amplitudes, in spite of diffusion by PDMS. Following the demonstration of OFI sensitivity to chemical absorption, chemical imaging of *in-vivo* tissues would become foreseeable.

1 Introduction

Visual inspection of skin is the primary and the sole screening method available today to dermatologists. Naked eye inspection is often supported by dermoscopy imaging [1], that provides better contrast over a wider spectral range. However, visible light is always being used and diagnosis mostly relies on the medical doctor expert skill. Suspicious cases of malignant lesions, such as melanoma, are most often treated only after the histological grading that required a preliminary biopsy. Histological sections are commonly stained by hematoxylin and eosin (HE stain) to provide the typical blue-pink colored tissue contrast at hands for the pathologist's diagnosis. Both of the above necessary steps, biopsy and staining, that are invasive, costly and time consuming could be replaced by the optical chemical imaging of the tissue acquired *in vivo* by reflectance microscopy.

In this context, chemical imaging refers to the identification and localization of molecules in a sample using light absorption as the contrast agent, instead of refraction or emission that conventional and luminescence microscopy rely on. It can be more effectively performed at mid infrared wavelengths (MIR) where organic molecules have their spectral signatures. Reflectance scanning confocal microscopy can be conveniently performed, at any wavelength, by optical feedback interferometry (OFI) [2]. OFI is a common path detectorless technique based on the laser self-mixing effect (LSM). In LSM, light emitted by the laser and back scattered by the sample, mix in the laser cavity providing a modulation signal conveniently acquired either by a photodetector, or by a voltage probe at the laser terminals [3], in the case of semiconductor lasers. In the infrared region, OFI has the advantage of being a very sensitive technique with respect to available detectors, to be practical also at wavelengths where efficient detectors are not yet available and to preserve the sample integrity, since LSM is a contactless reflectance technique. Additionally, OFI can be adapted to scanning microscopy reaching sub-wavelength spatial resolution [4] and confocal capability [5].

In this paper we present OFI imaging of synthetic tissue phantoms with dispersed potato starch organic molecules (PS). OFI imaging were collected at two wavelengths, one resonant with the starch's amide band around 6 μm, and the other in the starch transparency spectral region around 1 μm. Distinctive evidence of different starch concentration is provided by MIR OFI imaging, whereas NIR imaging, as well as visible inspection cannot distinguish among different samples.

2. Experimental

The samples are based on cured PDMS and are prepared using the Ayers's process [6]. *Sylgard*® 184 silicon elastomer kit, composed by the silicon matrix and a catalyst, acting as curing agent, was used to prepare the phantom base. We prepared the sample mixing 10ml of PDMS and 1ml of catalyst obtaining a volume of uncured PDMS phantom of 11 ml. The silicon matrix was divided into four equal parts to prepare pure cured PDMS phantoms, three of which then included potato starch at the concentration of 0.01 mg/g, 0.03 mg/g and 0.05 mg/g. The mixtures were manually mixed for 30 minutes and the uncured phantoms were placed in a vacuum chamber for 20 minutes to remove residual air bubbles. The phantoms were cured at room temperature for about 24 hours by placing the final mixtures in rectangular molds of 500μm depth and enclosing them between two plastic plates.

The samples were first characterized by transmittance spectroscopy using an FTIR spectrometer in the range 1538-8333 cm^{-1} (1.2 - 6.5 μm). Spectra are featureless in the NIR region, whereas show a wide absorption band

in the range 5.9-6.4 μm (for pure PDMS) and an additional narrow band (centered at 6.26 μm), whose absorption feature increases with concentration of the potato starch.

OFI was collected at the laser terminals of two semiconductor lasers: a low power dissipation Vertical Cavity Surface Emitting Laser (VCSEL) at 1.29 μm [7] and a Peltier cooled Quantum Cascade Laser (QCL) at 6.26 μm [8]. The laser beams were focused onto the sample by a parabolic mirror, after passing through a pinhole and a variable neutral filter.

Signal processing consisted of several steps: amplification, digital filtering, removal of DC offset, selection of fully completed fringes, fringe *shaping* in a triangle fashion. Height, slopes and full-width at half height were extracted from the *shaped* fringes and analyzeed in terms of averaged values, dispersion and uniformity across the sample surface.

3. Results

Three stripes of PDMS with different potato starch concentration were mounted side by side onto the same sample holder and scanned together by the VCSEL and the QCL. The voltage amplitude images of the three stripes are shown in Figure 1a (at 1.29 μm) and 1c (at 6.26 μm). The sample holder was scanned continuously along the horizontal axis and step scanned by 0.5 mm along the vertical axis. Mobile averages over the laser spot dimension were performed to account for the sample motion.

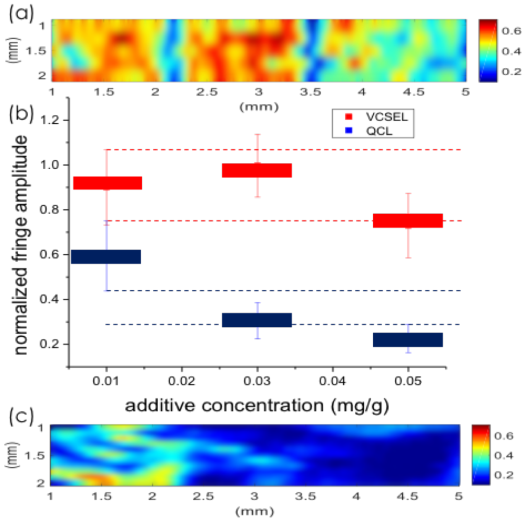

Figure 1: Signal amplitude distribution for the three PDMS samples with starch inclusion. Absolute amplitude scans at 1.29 μm (a) and 6.26 μm (c). (b) averaged amplitude over the three scanned areas. Dashed lines are guide to the eye.

In spite of the relatively large dispersion of the signal, the normalized voltage amplitude, shown in panel (b), pinpoints the role of the sample absorption coefficient in OFI imaging. The averaged signal over the scanned areas decreases for increasing potato starch concentration only at the amide-I absorption band (QCL wavelength). The same samples do not show relevant variations in the NIR region probed by the VCSEL, where potato starch is almost transparent.

4. Conclusions

Extraction of complex dielectric properties from reflection spectroscopy is a fairly complicated task [9, 10]. Recent attempts to use OFI for materials characterization resulted in a patent application [11], opening commercial scenarios for future developments. The selective sensitivity of optical feedback interferometry to absorption features in the molecular fingerprint region by commercially available QCL encourages further efforts to demonstrate chemical microscopy in reflectance by optical staining

5. References

[1] Vasefi1, et al., Sci. Rep. 2014, 4, 4924. **[2]** Rea, N.P., et al., Opt. Comm., 1996, 125, 158. **[3]** Lim, Y.L., et al., Proc. Of SPIE, 2016, 6038 **[4]** Lui, H.S., et al., Opt. Lett., 2014, 39 (9), 2629-2632. **[5]** Mowla, A., et al., Biomed. Opt. Expr. 2017, 8 (9), 4037. **[6]** Ayers, et al., Proc. of SPIE, 2008, 6870. **[7]** Cardilli, et al., Appl. Phys. Lett., 2016, 108, 031105. **[8]** Dabbicco, et al., IEEE J. Quant. Electron., 2003, 39, 701. **[9]** Dabbicco, et al., Sol. St. Comm., 2000, 114, 515. **[10]** Sun, J., et al., IEEE Access, 2018, 6, 8302. **[11]** Rakic, et. al., US Patent App. 14/913,507

Acknoledgements

Samples were prepared at INPT – Toulouse in the framework of EU COST-Action BM1205.

Semiconductor-based broad-band superluminescent diodes: a novel light source for photon correlation metrology: ghost imaging, ghost spectroscopy and ghost polarimetry

Wolfgang Elsäßer *, Patrick Janassek, and Sébastien Blumenstein

Institute of Applied Physics, Technische Universität Darmstadt,
Schlossgartenstrasse 7, 64289 Darmstadt (Germany)
**Corresponding author: Elsaesser@physik.tu-darmstadt.de*

Summary: We exploit photon bunching of broad-band amplified spontaneous emission light emitted by semiconductor-based superluminescent diodes. We demonstrate ghost metrology applications as ghost imaging and ghost spectroscopy based on the spatial and spectral correlations of these classically correlated photons. We conclude by discussing further perspectives and possibilities of photon bunching for ghost metrology applications as e.g. ghost polarimetry.

1 Introduction

Ghost imaging (GI) is by far not a "spooky action" but rather a photon correlation imaging modality based on the fundamentals of quantum optics, either realized with entangled photons in the quantum GI version or with bunched photons from classical thermal sources. In contrast to conventional imaging systems, GI exploits intensity correlations of light to retrieve an image of an object. Ghost Imaging (GI) or photon-correlation imaging is one of the recent topics of quantum optics. After the first demonstration in 1995 with entangled photon [1] also classical GI [2,3] has been demonstrated with light emitted by rather complex, bulky thermal light sources. The name GI results from the fact that the image is formed by light which has never interacted with the object. Hereby, the total intensity of the transmitted or reflected light of an illuminated object and the spatially resolved intensity of a highly (position)-correlated reference beam which itself has never interacted with the object, are detected. The information of both intensities alone is not enough to form an image of the object. However, correlating the two intensities in terms of the intensity autocorrelation or second order correlation yields an image, the ghost image.

2. Ghost metrology: ghost imaging and ghost spectroscopy - concepts, results and discussions

Very recently, we introduced to the field of ghost modalities a novel, extremely compact ultra-miniaturized superluminescent diode (SLD) source [4] emitting at 1250nm based on Amplified Spontaneous Emission (ASE). In a classical GI experiment we exploit the full in-coherence of light as requested for classical GI, namely in 1st order coherence being spectrally broad-band, in 2nd order coherence exhibiting Hanbury-Brown & Twiss photon bunching with a correlation coefficient of two and being spatially incoherent due to the dynamic mode filamentation of the broad-area waveguide structure.

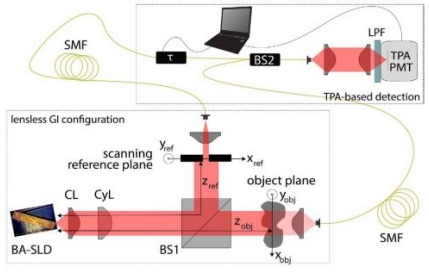

Fig. 1 Experimental set-up for the realization of a ghost imaging with classical light form a superluminescent diode

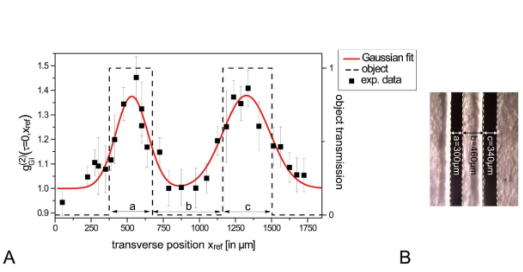

Fig. 2 Ghost Image (part A) of a double slit object (as shown in part B) in terms of the second order correlation coefficient $g^{(2)}(\tau)$, i.e. the ghost image

Here, the presentation will start with the discussion of the experimental results of investigations of the second order coherence of SLDs, i.e. demonstrating the fundamental photon bunching. We then proceed to the basics of ghost modalities by illustrating the key elements of GI with classical correlated light emitted by super-luminescent diodes with the set-up schematically shown in Fig.1 and demonstrate ghost imaging results of a macroscopic double slit transmission object as depicted in Fig. 2.

We then extend the field of ghost modalities in analogy to this classical spatial GI principle with classical light to ghost spectroscopy. We propose and realize a first ghost spectroscopy (GS) experiment with classical light by exploiting spectral correlations of light emitted by a broad-band semiconductor-based superluminescent diode (SLD) and demonstrate the applicability of this ghost modality in a real-world proof-of-principle experiment by measuring a ghost absorption spectrum $\alpha(\lambda)$ of the characteristic absorption features of chloroform at 1214nm, i.e. a ghost spectrum [5]. Figure 3 shows the schematic realization of this set-up and Fig. 4 shows the proof-of-principle demonstration experiment with the ghost absorption spectrum of chloroform.

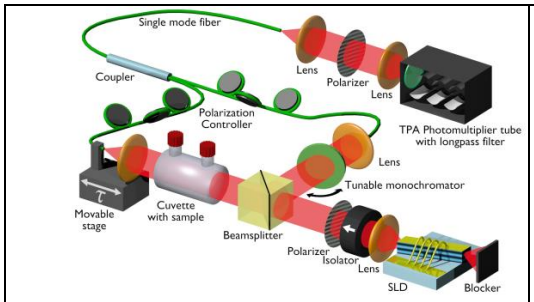

Fig. 3 Experimental set-up for the realization of a ghost spectroscopy experiment at the absorption line of chloroform.

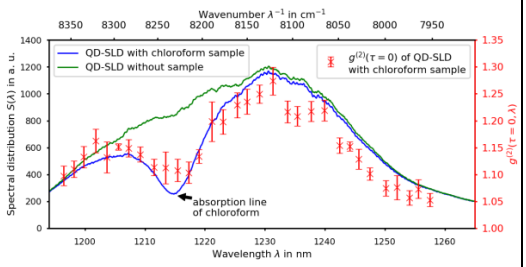

Fig. 4 Ghost spectrum of an absorption feature of chloroform at 1215nm measured with the set-up of Fig.3. (SLD spectrum (green), conventionally measured absorption spectrum of chloroform(blue, both left scale) and ghost spectrum (red) obtained via the spectral intensity correlation (right scale))

3. Conclusions

This is the first time, that ghost spectroscopy has been realized with a broad-band semiconductor-based light source by exploiting the spectral correlations of a broad-band thermal semiconductor light source. Finally, we shall discuss further perspectives and possibilities of photon bunching in amplified spontaneous emission light suggesting the realization of ghost polarimetry (GP) by exploiting polarization correlations [6]. We are convinced that this amplified emission source concept and the pursued and exploited analogy between ghost imaging and ghost spectroscopy will further fertilize the field, thus allowing to develop a deeper understanding of the experimental scheme and even leading to other ghost metrology protocols.

4. References

[1] T. B. Pittmann, Y. H. Shih, D. V. Strekalov and A. V. Sergienko, Phys. Rev. **A 52**, R3429(R) (1995).
[2] R. S. Bennink, S. J. Bentley and R. W. Boyd, Phys. Rev. Lett. **89**, 113601 (2002).
[3] F. Ferri, D. Magatti, A. Gatti, M. Bache, B. E. and L. A. Lugiato, Phys. Rev. Lett. **94**, 183602 (2005).
[4] S. Hartmann and W. Elsäßer, Sci. Rep. **7**, 41866 (2017)
[5] P. Janassek, S. Blumenstein, and W. Elsäßer, Phys. Rev. Appl. **9**, 021001 (2018)
[6] P. Janassek, S. Blumenstein, and W. Elsäßer, Opt. Lett. **43**, 883 (2018)

Acknowledgements

This work has been supported by the Deutsche Forschungsgemeinschaft (DFG). We gratefully acknowledge the excellent technological realization of the SLDs by M. Krakowski (III-V labs) and I. Krestnikov (Innolume) within the framework of the EU project “FAST-DOT”.

Improved feedback stability of semiconductor nanolasers by inclusion of a Fano mirror

Thorsten S. Rasmussen[1]* and Jesper Mørk[1]

1, Dept. of Photonics Engineering, Technical University of Denmark
**thsv@fotonik.dtu.dk*

Summary: The photonic crystal Fano laser is presented, including the laser structure and theoretical model. The model is utilised to investigate numerically the sensitivity of the laser to external feedback with respect to the stability of the output signal, and the results are compared to the well-known behaviour of conventional Fabry-Perot-type lasers. The conventional operational regimes are observed, including continuous-wave, periodic modulation, pulse generation and chaos. However, it is then demonstrated how the narrowband reflectivity of the Fano mirror works to filter de-stabilising frequency components, leading to significantly better operational stability, so that the sensitivity toward external feedback is drastically improved.

1. Introduction

Photonic crystal (PhC) lasers are promising light sources for applications in photonic integrated circuits such as on-chip signal processing [1], with much progress being made towards thresholdless lasing [2] and integration onto silicon [3]. Recently, a novel type of PhC laser was realised by replacing one of the conventional laser mirrors by a Fano resonance, which creates a narrow resonance in the reflection spectrum [4]. This Fano laser (FL) showed desirable properties such as pinned single-mode lasing and self-pulsing [5], and it has been predicted that the laser has a modulation bandwidth greatly exceeding that of conventional lasers [6].

One particular issue for on-chip applications of semiconductor nanolasers is the lack of a readily available optical isolator, since it is well established that semiconductor lasers in particular suffer from high sensitivity to external feedback [7]. Even extremely weak external feedback on the order of -30 dB can lead to dynamic instabilities and chaos, undermining the operational reliability [8]. In this work, we compare the feedback stability of the Fano laser using an iterative travelling-wave model to the results for a conventional Fabry-Perot (FP) laser, as modelled using the well-known Lang-Kobayashi (LK) model for lasers with external feedback, and find that the Fano laser is significantly more resilient towards feedback-induced instabilities.

2. Fano laser structure and model

The Fano laser is realised in an InP photonic crystal membrane structure, as a line-defect waveguide with a nearby point defect H0 nanocavity, as shown in figure 1**(a)**. One laser mirror is created by termination of the waveguide, while the other mirror is formed by Fano interference due to the coupling of the continuum of waveguide modes to the discrete mode of the nanocavity.

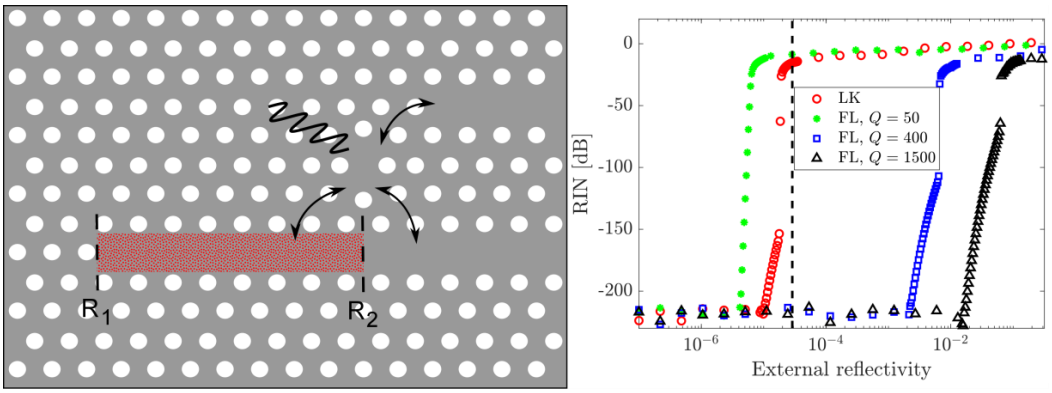

Figure 1: **(a)** Fano laser structure. The grey region is an InP membrane, and the white circles represent air holes. The laser mirrors are indicated, as are the coupling channels into and out of the nanocavity. The red dots represent the quantum dot active material. **(b)** Calculated relative intensity noise as function of the external power reflectivity for both the conventional laser (red circles) and the Fano laser (green, blue, black). As the quality factor of the Fano laser increases, so does the feedback stability, due to the narrowing of the mirror linewidth, far outperforming the conventional laser. The dashed black line indicates an analytical prediction for the onset of coherence collapse for the Lang-Kobayashi model.

This coupling leads to a narrow resonance in the reflection spectrum with a bandwidth inversely proportional to the Q-factor of the nanocavity. The active material of the laser consists of InGaAs quantum dots embedded in the membrane, and the device is pumped optically.

The dynamics of the Fano laser are modelled using an iterative travelling wave model, where the evolution of the laser cavity field is coupled to the nanocavity field, as described by coupled-mode theory, in order to account for the dynamic interference phenomenon that forms the laser mirror [4].

3. Feedback dynamics and stability comparisons

Figure 1**(b)** shows the calculated relative intensity noise (RIN) of the laser as a function of the external amplitude reflectivity for both the FP laser and Fano lasers with different Q-factors of the nanocavity. All other parameters are identical, including mirror reflectivity, laser threshold, and pump power. The RIN is calculated as

$$\mathrm{RIN} = \frac{\delta P^2}{\langle P \rangle^2} \tag{1}$$

where δP is the standard deviation of the output power and $\langle P \rangle^2$ is the square of the mean power. In the low Q-limit the FL curve approaches the LK curve. This agrees well with theory, where the FL model converges to the LK model if the feedback is weak and the nanocavity field can be adiabatically eliminated. As such, the green curve is essentially a convergence check, while the blue and black curves represent realistic FLs. We note here that spontaneous emission noise is excluded from the analysis, so that the RIN calculated by equation (1) is purely deterministic and is used to quantify the stability of the laser.

As the quality factor of the nanocavity is increased, the bandwidth of the mirror resonance decreases and the evolution of the FL RIN curve changes significantly. In particular, it is evident that the dramatic increase in RIN that signifies the onset of instabilities and chaos requires a significantly larger external reflectivity when the quality factor of the nanocavity is increased to realistic values. This significant increase in stability is attributed to the Fano mirror functioning as a narrowband filter, which decreases in linewidth as the quality factor is increased. As such, additional frequency components do not stay in the laser cavity to be amplified, retaining the narrow linewidth and stable operation even for large levels of feedback.

Generally, the shape and evolution of the RIN curves depend strongly on a number of parameters, including the pumping strength, delay time, and linewidth enhancement factor, but in all cases the Fano laser has a much lower feedback sensitivity than conventional FP lasers. For some parameter combinations, the difference in external feedback level for the conventional and Fano lasers at the onset of instability is orders of magnitude, showing how the nanocavity dynamics serve to strongly damp any fluctuations. This effect can also be observed by looking directly at the small-signal IM response, as in [6], where it was demonstrated how the IM response of the FL is damped in proportion to the quality factor of the nanocavity. This agrees with results for conventional lasers, where increased damping improves stability [7].

4. Conclusions

The Fano laser was presented, and it was demonstrated how the replacement of a conventional Fabry-Perot mirror by a Fano resonance in a photonic crystal laser may lead to improved feedback stability due to the strong dispersion of the Fano mirror. This was illustrated by calculations of the evolution of the relative intensity noise as the external feedback increases, showing how the onset of instabilities and chaos occur at a much higher external feedback for Fano lasers. The improved stability was attributed to the narrow bandwidth of the Fano mirror, which scales with the quality factor of the nanocavity, as was also observed for the feedback sensitivity.

5. References

[1] D. A. B. Miller, "Device requirements for optical interconnects to silicon chips," Proc. IEEE **97**, 1166–1185 (2009)
[2] Y. Ota et al., "Thresholdless quantum dot nanolaser," Opt. Express **25**, 19981–19994 (2017)
[3] G. Crosnier et al., "Hybrid Indium phosphide-on-silicon nanolaser diode" Nat. Photonics **11**, 297 (2017)
[4] J. Mork et al, "Photonic crystal fano laser: Terahertz modulation and ultrashort pulse generation," Phys. Rev. Lett. **113**, 163901 (2014).
[5] Y. Yu et al, "Demonstration of a self-pulsing photonic crystal fano laser," Nat Photon **11**, 81–84 (2017)
[6] T. S. Rasmussen et al, "Modes, stability, and small-signal response of photonic crystal Fano lasers", Opt. Express **26**(13) (2018)
[7] K. Petermann, "External optical feedback phenomena in semiconductor lasers", IEEE JQE **1** (2) (1995)
[8] J. Mork et al, "Chaos in semiconductor lasers with optical feedback: Theory and experiment", IEEE JQE, **28**(1):93-108 (1992)

Acknowledgements

Authors acknowledge financial support from Villum Fonden through the NATEC Center of Excellence.

Spontaneous and stimulated emission in nanoscale light sources

A. Fiore[1]*, B. Romeira[1], V. Dolores-Calzadilla[1], A. Higuera-Rodriguez[1], D. Heiss[1] and M.K. Smit[1]

1 Institute for Photonic Integration, Eindhoven University of Technology, 5600 MB Eindhoven, The Netherlands
**a.fiore@tue.nl*

Summary: NanoLEDs and nanolasers are both being considered as low-power sources for optical interconnects. In this talk some fundamental aspects related to light emission in these nanoscale sources will be reviewed. First, experimental results on nanoLEDs coupled to optical waveguides on Si will be presented. The role of surface recombination and effective passivation methods will be discussed. In the second part of the talk, the ultimate limits to scaling in LEDs and lasers will be analyzed, using a simple theoretical model. Particular attention will be given to the role of the mode volume scaling on the spontaneous and stimulated emission rates and therefore on the modulation bandwidth.

1 Introduction

Short-distance optical interconnects require optical sources operating efficiently at low output powers. As lasers are only efficient above threshold, and the threshold current scales with the volume of the active region, miniaturization of semiconductor lasers has been a hot topic in research, with a race towards sub-micrometer lasers [1]. However, making a small and efficient laser is challenging, and the alternative option of efficient nano-light-emitting diodes (nanoLEDs) is also under investigation. While the efficiency of conventional LEDs is limited by the fact that only a fraction of spontaneously emitted photons can be collected, the modification of the spontaneous emission rates occurring in a wavelength-sized cavity can in principle offer a solution. Indeed, the spontaneous emission rate scales as the inverse of the mode volume, and, in the case of a spectrally narrow emitter, with the quality factor of the cavity, leading to large enhancements for small and low-loss cavities (the so-called Purcell effect). Additionally, emission into other, unwanted modes can be suppressed in small cavities. This has led to the expectation that nanoLEDs could be both efficient and fast. Moreover, the enhancement of the spontaneous emission rate also has consequences for the shape of the light-current curve in a nanolaser, leading to the disappearance of a clear threshold. NanoLEDs and nanolasers are often modeled by introducing the Purcell enhancement factor and/or the spontaneous emission coupling factor as ad-hoc parameters, while they are intrinsically connected to the physical cavity parameters, such as mode volume, cavity linewidth and emitter's homogeneous and inhomogeneous linewidth. In particular, the deep connection between spontaneous and stimulated emission rates (Einstein's relations) should always be explicitly considered when modeling the effect of mode volume reduction in a nanolaser.

2. Experimental results

We will first discuss the experimental characterization of a nanoLED, designed to be efficiently coupled to an on-chip waveguide on an InP-on-Si platform [3]. It provides waveguide-coupled output powers in the ~20 nW range and a sub-ns electro-optical response. We show that the main limiting factor in the efficiency is represented by surface recombination, and we discuss a passivation method which allows reducing the surface recombination velocity by two orders of magnitude in InGaAs nanoscale active regions [4].

3. Modeling

We discuss a simple rate equation model which treats spontaneous and stimulated emission rates on the same footing and thereby captures the main features of size scaling in nanoLEDs and nanolasers [5]. The effect of homogeneous and inhomogeneous broadening of the semiconductor active medium is also explicitly taken into account. The main conclusions are that the Purcell enhancement factor is strongly reduced and becomes close to one in realistic structures, due to linewidth broadening, and that the enhancement of the *stimulated* emission rate (i.e. increase in modal gain) with mode volume has the most prominent effect in the static and dynamic characteristics of nanolasers. The expected modulation bandwidths for different nanolaser designs will be discussed.

5. References

[1] M.T. Hill and M.C. Gather, "Advanced in small lasers", Nature Photonics, Vol. 8, pp. 908-918, 2014
[2] E. M. Purcell, “Spontaneous emission probabilities at radio frequencies,”, Phys. Rev., Vol. 69, p. 681, 1946.
[3] V. Dolores-Calzadilla et al., "Waveguide-coupled nanopillar metal-cavity light-emitting diodes on silicon", Nature Comm., Vol. 8, p. 14323 (2017)

[4] A. Higuera-Rodriguez et al., "Ultralow Surface Recombination Velocity in Passivated InGaAs/InP Nanopillars", Nano Lett. Vol. 17, pp. 2627-2633, 2017
[5] B. Romeira and A. Fiore, "Purcell Effect in the Stimulated and Spontaneous Emission Rates of Nanoscale Semiconductor Lasers", IEEE J. Quantum Electron., Vol. 54, p. 2000412, 2018

Acknowledgements

This research was supported by the EU FP7 project NAVOLCHI (288869), the ERC project NO LIMITS, NanoNextNL, a micro- and nano-technology program of the Dutch Ministry of
Economic Affairs and Agriculture and Innovation and 130 partners, the Marie Skłodowska-Curie fellowship NANOLASER (2014-IF-659012) and the Dutch Gravity program "Research Centre for Integrated Nanophotonics"

Understanding the emergence of non-equidistant multi-pulse emission in passively mode-locked VECSELs

J. Hausen[1]*, S. Meinecke[1], B. Lingnau[1] and K. Lüdge[1]

1 Technische Universität Berlin, Hardenbergstraße 36, 10623 Berlin, Germany
**hausen@campus.tu-berlin.de*

Summary: Mode-locked semiconductor lasers are widely used for the generation of short pulses. If the amplifying and the absorbing material are embedded in a V-shaped external cavity, new multi-pulse solutions emerge. We theoretically model the device by multi-delay differential equations and apply numeric integration as well as path-continuation to understand the underlying bifurcation scenarios. Our investigations predict various parameter regions with complex non-equidistant pulse emission that emanate by repositioning the gain chip. We show that the degree of multi-stability increases with the cavity size and that the new solutions emerge from the fundamental mode-locking solution in a series of saddle-node bifurcations.

1 Introduction

Mode-locked lasers are exceptional sources for the generation of short pulses of light. Depending on the operation conditions different dynamical regimes, ranging from Q-switching to high-order harmonic mode-locking, exist and are well understood for monolithically integrated devices [1][2]. However, if the amplifying and the absorbing material are embedded in an external cavity (VECSEL) with a V-shaped geometry, e.g. done to obtain pulses with a duration of 100fs and repetition rates in the GHz ranges [3], new solutions with multiple non-equidistant pulses emerge [4][5][6]. We investigate the device as shown in Fig.1a from a dynamical point of view and analyse the underlying bifurcations leading to the various dynamical regimes. A special focus is set to the cavity geometry, i.e. the influence of the delays/length of the optical arms.

2. Bifurcation analysis

To understand the underlying mechanisms of these new non-equidistant pulse train dynamics (pulse clusters) and to unravel the respective bifurcation scenario, we derive a system of multi-delay differential equations from a travelling wave approach including the electric field and charge-carrier dynamics in the gain/absorber chip. After introducing a variable transformation [7], we obtain a system with three delays, which in turn depend on the gain chip position relative to the outcoupling facet/absorber and the total cavity roundtrip time (see Fig.1a).

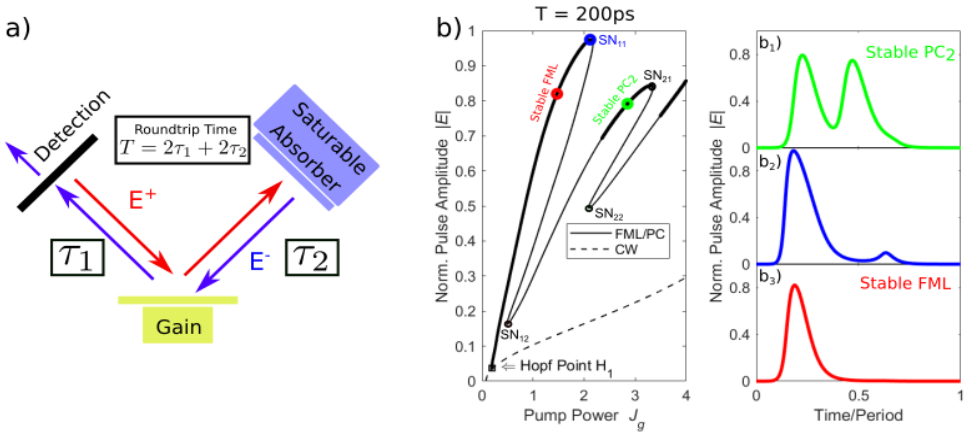

Figure 1: a) V-shaped cavity geometry with forward (backward) propagating field E^+ (E^-) indicated as blue (red) arrows. b) Path continuation of the fundamental periodic mode-locking (FML) branch (solid line) emerging from the continuous wave solution (CW, dashed line). Pulse cluster solutions (PC shown in b_1) emanate from the FML solution (shown in b_3) in a series of saddle-node bifurcations (SN), where an additional a side pulse appears (shown in b_2) which grows in amplitude with increasing pump power.

Taking into account the dynamical variables of the electric field E and the integrated carrier densities of the gain G and the absorber Q the DDE system reads as follows:

$$\dot{E} = -\gamma E(t) + \gamma\sqrt{\kappa}E(t-T)e^{\frac{1-i\alpha_g}{2}(G(t-T+2\tau_2)+G(t-T))+(1-i\alpha_q)Q(t-T)}$$
$$\dot{G} = J_g - \gamma_g G(t) - (e^{G(t)}-1)\{|\ E(t)\ |^2 + |\ E(t-2\tau_2)\ |^2\ e^{2Q(t-2\tau_2)+G(t-2\tau_2)}\} \quad \text{Eq.(1)}$$
$$\dot{Q} = J_q - \gamma_q Q(t) - r_s(e^{2Q(t)}-1)e^{G(t)}\ |\ E(t)\ |^2$$

The evoking dynamics in turn depend on the gain bandwidth γ, the pump current J_g, the unsaturated absorption J_q, the carrier recovery rate in the gain γ_g and absorber γ_q section, the ratio of the saturation energies r_s, the mirror losses at the facet κ and the amplitude phase coupling coefficients of gain α_g and absorber α_q section. While the model given in Eq.(1) is able to accurately describe the dynamics, it is simple enough to allow for a comprehensive bifurcation analysis. On that account we apply numeric integration techniques as well as the path continuation software DDE-biftool for delay differential equations. Specifically, we study the dependencies of the dynamics and bifurcations on the pump parameter J_q, the gain bandwidth γ, the cavity roundtrip time T and the gain chip position (τ_1 and τ_2).

Our investigations predict various parameter regions with complex non-equidistant pulse trains and a high degree of multi-stability, that critically depend on the cavity configuration. Furthermore, our bifurcation analysis leads to an in-depth understanding of the emerging multi-pulse solutions and shows that they emanate from the fundamental mode-locking solution, which branches off the continuous wave emission solution branch (CW) in the Hopf-point H_1 as indicated in Figure 1b. Subsequent saddle-node (SN) and torus bifurcations (T) lead to changes in stability of the pulse clusters and furthermore pulses are added to the cluster. This can be seen in Fig.1b where stable regions of pulse cluster emission are marked and examples of pulse shapes along the branch are shown. Higher numbers of pulses are created with increasing pump power and cavity roundtrip time. With an increasing roundtrip time (starting from 200ps), the fundamental mode locking solution as well as the pulse cluster solutions detach from the H_1 branch and become independent, i.e. not connected to the remaining solutions.

3. Conclusions

We model a V-shaped cavity passively mode-locked laser using a system of delay differential equations in which the delays depend on the spatial position of the laser components. We find pulse clusters emerging from the continuous wave solutions in the first Hopf bifurcation. Their stability and number of pulses in the cluster is changed in a series of subsequent torus and saddle-node bifurcations. Increasing the cavity roundtrip time while maintaining a symmetric positioning of the components, leads to a detaching of the lower order pulse cluster solutions and to an emergence of higher order pulse clusters with several pulses per cluster. Breaking the symmetry of the cavity by repositioning the gain chip shifts the stability to higher order pulse clusters.

5. References

[1] L. Jaurigue, Springer, "Passively Mode-Locked Semiconductor Lasers", Springer, 2017.
[2] Vladimirov et al., "Nonlinear Laser Dynamics – From Quantum Dots to Cryptography". K. Lüdge, Wiley, 2011.
[3] P. Klopp et al., "Mode-locked InGaAs-AlGaAs disk laser generating sub-200fs pulses, pulse picking and amplification by a tapered diode amplifier", Opt.Express 17(13), 10820, 2009.
[4] D. Waldburger et al., "Multipulse instabilities of a femtosecond SESAM-modelocked VECSEL", Opt. Express **26**, 21872, 2018.
[5] S. Link et al., "Coherent beam combining and noise analysis of a colliding pulse modelocked VECSEL", Opt. Express 25(16), 19281, 2017.
[6] T. Malica et al., "Mapping the dynamical regimes of a SESAM mode-locked VECSEL with long cavity using time series analysis", Opt. Express 26(13), 16624, 2018.
[7] L. Lücken et al., "Reduction of interaction delays in networks", Europhys. Lett. 103, 10006, 2013.

Acknowledgements

We acknowledge the funding of the German Research Foundation (DFG) within the SFB787.

Master equation for modelocking in lasers with fast gain recovery

A. M. Perego[1], B. Garbin[2], F. Gustave[3], S. Barland[3], F. Prati[4] and G. J. de Valcárcel[5]*

1 Aston Institute of Photonic Technologies, Aston University, Birmingham B4 7ET, United Kingdom
2 The Dodd-Walls Centre for Photonic and Quantum Technologies, The University of Auckland, Auckland 1142, New Zealand
3 Université Côte d'Azur, CNRS, INPHYNI, F-06560 Valbonne, France
4 Dipartimento di Scienza e Alta Tecnologia, Università dell'Insubria, via Valleggio 11, 22100 Como, Italy
5 Departament d'Òptica, Universitat de València, Dr. Moliner 50, 46100 Burjassot, Spain
**german.valcarcel@uv.es*

Summary: We present a theoretical framework that allows accurate master equation modelling of coherent effects in modelocked lasers with fast gain, where the well-known Haus theory fails. The novel master equation contains the Risken-Nummedal-Graham-Haken coherent instability and reproduces well the experimental dynamics of pulses generated by a semiconductor laser with external cavity, modelocked through periodic loss modulation.

1. Introduction

The paradigmatic model describing modelocking in lasers, Haus master equation [1,2], holds under the hypothesis that the gain recovery time is much larger than the cavity roundtrip time. Such limitations impose severe constraints on Haus theory applicability to semiconductor or quantum cascade lasers, where the gain recovery time can be in general faster, being even close to the picosecond or shorter.

We have developed a novel theoretical approach that allows deriving master equations for modelocking in lasers valid beyond the Haus limit, while agreeing perfectly with Haus equation in the parameters region where the latter applies. In particular we present here a master equation for active modelocking that captures the Risken-Nummedal-Graham-Haken coherent instability, claimed to be at the basis of modelocking and frequency comb generation in some semiconductor lasers, like quantum cascade lasers.

Experiments confirm quantitatively the predictions of our model in the case of a modelocked semiconductor laser, capturing both the pulse shape and the stability region of the pulses.

2. Coherent effects in mode-locking

A key point of our approach is the splitting of the gain into a slow component, which doesn't display variations on the cavity roundtrip timescale, and a fast component. Our model consists in a dynamical equation for the electric field envelope coupled to another one for the slow gain component, while the fast gain component follows adiabatically (is dynamically slaved to) the other two variables. It is the fast gain component that carries coherent effects information. The master equation has been derived from Maxwell-Bloch equations; by employing an improved adiabatic elimination technique, we have been able to incorporate in our model the full coherent effects arising from the light-matter interaction inside the gain medium. We show that indeed such coherent effects become relevant for the dynamics of pulses when the gain lifetime approaches the cavity roundtrip time.

By preserving features characterizing light-matter interaction our model perfectly captures the coherent Risken-Nummedal-Graham-Haken instability [3,4] being hence able to model spontaneous modelocking.

3. Experimental test

We have performed experiments in a ring cavity resonator using a bulk semiconductor amplifier as a gain medium while modelocking operation has been achieved through modulation of losses performed using a Mach-Zehnder modulator. We have performed different series of experiments under different harmonic modelocking orders. This approach allows us varying the effective cavity roundtrip time by more than one order of magnitude without changing the cavity setup [5]. Here we show results corresponding to a cavity roundtrip time on the order of the nanosecond, which is comparable to the estimated value of the gain recovery time. Even in this case Haus theory is unable to account for the experimental observations. In particular two key features completely absent in Haus theory are well captured by our model: the pulse shape deviates from Gaussian (exhibiting different shapes according to the amount of applied detuning: asymmetric bell-shape, pulses with one or more bumps, and sech-like pulses) and is asymmetric with respect to the action of modulator frequency detuning with respect to resonance.

4. Conclusions

Our novel master equation, whose predictions have been successfully verified experimentally, is a compact model that can be easily integrated numerically and can be potentially generalized to a great variety of modelocking techniques (pump current modulation, saturable absorber, Kerr-lens, and spontaneous modulation instability: Benjamin-Feir and Risken-Nummedal-Graham-Haken instability).

Potential applications of our new model may be found in describing modelocking dynamics in semiconductor and quantum cascade lasers being much more compact than the full set of Maxwell-Bloch equations.

5. References

[1] H. A. Haus, "A Theory of Forced Mode Locking," IEEE J. Quantum Electron. **11**, 323 (1975).
[2] H. A. Haus, "Mode-locking of lasers," IEEE J. Sel. Top. Quantum Electron. **6**, 1173 (2000).
[3] E. Roldán et al., "Multilongitudinal mode emission in ring cavity class B lasers", in *Trends in Spatiotemporal Dynamics in Lasers. Instabilities, Polarization Dynamics, and Spatial Structures*, edited by O. Gomez-Calderón and J. M. Guerra (Research Signpost, Trivandrum, India, 2005) pp. 1-80, https://arxiv.org/abs/physics/0412071.
[4] C. Y. Wang et al., "Coherent instabilities in a semiconductor laser with fast gain recovery," Phys. Rev. A **75**, 031802(R) (2007).
[5] M. Pang et al., "All-optical bit storage in a fibre laser by optomechanically bound states of solitons," Nature Photon. **10**, 454 (2016).

Near field analysis of broad-area high-power laser diode using nonlinear bidirectional beam propagation method

A. Maina* and C. Coriasso

Prima Electro S.p.A., via G. Schiaparelli 12, 10148 Torino, Italy
**alberto.maina @primaelectro.com*

Summary: A modelling tool based on a nonlinear finite-difference bidirectional Beam Propagation Method (BPM) was developed to study the optical filamentation of the near field in high-power broad-area laser diodes. The near-field pattern, resulting from the multimode laser waveguide in the slow-axis direction, can show strong peaks whose optical density could exceed the Catastrophic Optical Mirror Damage (COMD) threshold. A control of the optical filamentation at the design stage is thus of utmost relevance to fabricate highly reliable high-power semiconductor lasers.

1 Introduction

Semiconductor lasers emitting in the 9xx nm range whose optical output power significantly exceed 10W are commonly used for many applications including fiber-laser pumping and direct-diode material processing. In order to manage high optical powers, these devices necessarily have a broad-area multimodal active waveguide in the lateral direction (*slow-axis*) causing optical filamentation of the lateral far- and near-field by self-focusing mechanism and mode instability [1], see Fig. 1(a). The waveguide is single mode in the vertical direction (*fast-axis*), where the optical confinement is due to the epitaxial heterostructure embedding the quantum well active layer. The main issue associated with the slow-axis near-field filamentation pattern is the possible presence of peaks whose optical density can reach several tens of MW/cm^2 causing high facet-temperature spots followed by COMD [2].

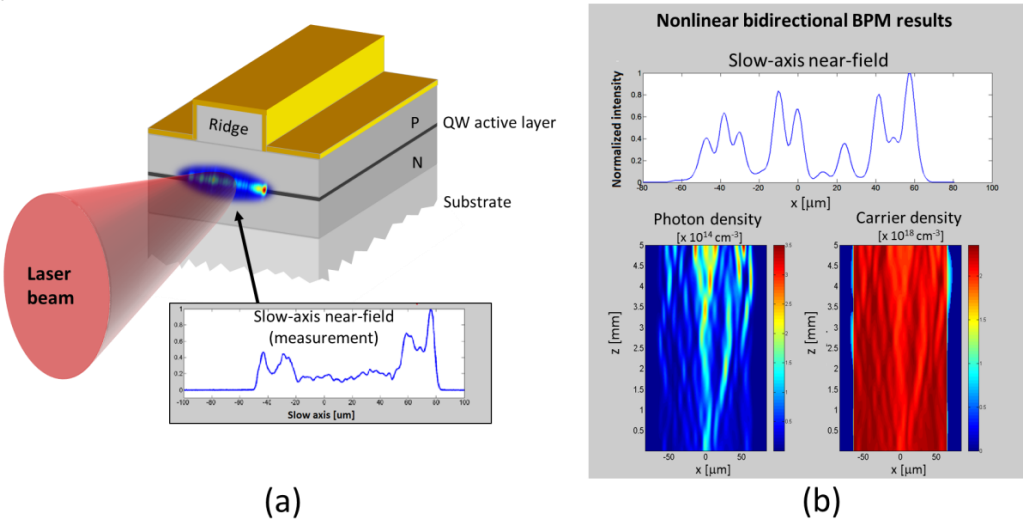

Figure 1: (a) slow-axis near field of a high-power broad-area semiconductor laser, (b) modelling results

In order to address the issue at the device design stage we have developed a numerical tool based on the nonlinear finite-difference bidirectional BPM. The tool was used to identify laser structure changes affecting the near-field pattern with the goal of reducing the strongest peaks, thus increasing the laser-facet reliability.

2. High power laser structure

Our laser epitaxial structure consists of a single 8nm InGaAs/AlGaAs QW embedded between asymmetric GRIN-SCH AlGaAs layers. It was grown by MOCVD on a n-doped (100) 2-degree-off GaAs substrate. The QW and the cladding layer's thickness, doping, and composition were designed to achieve a reduced vertical and lateral far-field width (FWHM@1/e^2 < 58^o $\perp$, 12^o $\|$), an high differential efficiency (> 1 W/A) and a low series resistance (< 20mΩ). Low optical losses (< 0.8cm^{-1}) allowed a 5mm cavity length and lateral optical confinement was provided by a broad area ridge waveguide structure 130µm wide. A low reflective (~2%) and a high reflective (> 95%) mirror coatings were applied to laser facets, after protection with a proprietary passivation technology. Fabricated chips were mounted in 90W multi-emitters for CW fiber-laser pumping.

3. Modelling tool and results

The numerical tool, developed with a Matlab and Fortran code, is based on the Crank-Nicholson scheme solution for the finite-difference bidirectional BPM including the transfer-matrix method to account for reflectivity at the numerical-grid points [3, 4]. A model of the quantum-well's non-linear complex refractive index [5] and the photon-carrier rate equation are self-consistently included in the calculation scheme. The propagation equations for the BPM are:

$$\frac{\partial \psi^{+}}{\partial z} = i\hat{\beta}\left(\sqrt{1+\frac{1}{\hat{\beta}^2}\left(k_0^2\hat{n}^2-\hat{\beta}^2+\frac{\partial^2}{\partial x^2}\right)}-1\right)\psi^{+}$$

and its time-reversed for the counter-propagating field ψ^{-}, where the squared-root operator is evaluated using the Padè approximants [3]. The tool allows the calculation of the optical property variations, the carrier density and the nonlinear electromagnetic field propagation along the resonant cavity at varying injected currents, see fig. 1(b). Nonlinear effects like the Spatial Hole Burning (SHB) and the induced transparency in waveguide surrounding regions are numerically reproduced. The tool has been used to calculate the near field pattern, showing a qualitative agreement with the experimental findings. In particular, we observed the highest-intensity peak location toward waveguide edges, where COMD statistical frequency shows a maximum. We studied, both experimentally and numerically, the flattening of the near-field profile by increasing the waveguide optical confinement by means of the ratio between the average intensity and the maximum peak, see fig.2. In order to evaluate the mode distribution (Parseval's coefficients) contributing to the emitted field, a modal decomposition of the calculated field was performed.

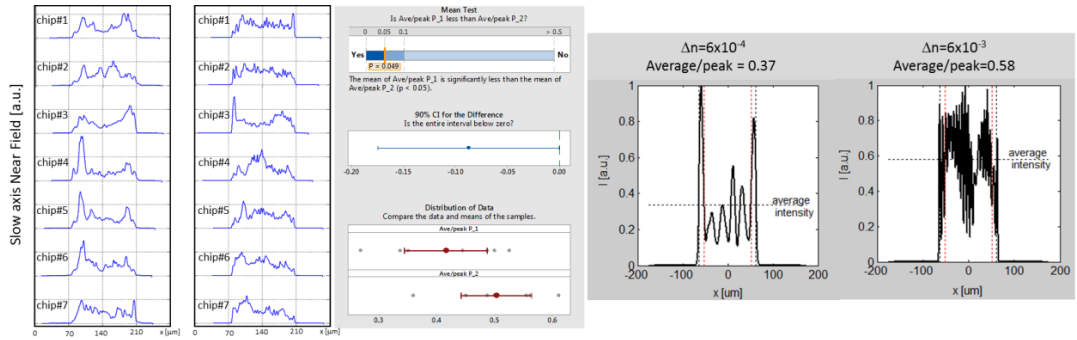

(a) Near field measurements: (left) Process PE102 ($\Delta n=4x10^{-4}$), (right) Process PE104 ($\Delta n=2x10^{-3}$)

(b) Two-sample t-test between average/peak for processes PE102 and PE104

(c) Nonlinear bidirectional BPM results: near field and relevant average/peak values for a low confining and a high confining waveguide

Figure 2: Slow-axis near-field measurements of laser chips belonging to wafer processes with different optical confinement (a), statistical comparison of average/peak values (b) and numerical calculations (c)

5. Conclusions

The nonlinear finite-difference BPM is a powerful tool to study and control the optical filamentation of the high-power broad-area semiconductor-laser slow-axis near-field. The effect of the optical confinement was investigated. Future analysis will be focused on other structure parameters and waveguide-side geometry in order to control the mode distribution. Future developments of the tool could consider the photoelastic and the thermorefractive effects in order to reproduce realistic behaviour of mounted laser devices under CW operation.

5. References

[1] H. Wenzel, "Basic aspects of high-power semiconductor laser simulation", IEEE J. Sel. Topics Quantum Electron., Vol. 15, pp.1502913, 2013
[2] M. Bou Sanayeh et al., "The physics of catastrophic optical damage in high-power AlGaInP laser diodes," Proc. SPIE 6997, Semiconductor Lasers and Laser Dynamics III, 699703, 2008
[3] H. Rao et al., "A Bidirectional Beam Propagation Method for Multiple Dielectric Interfaces", IEEE Photon. Technol. Lett., vol. 11, pp. 830-832, 1999
[4] J. P. Leidner, "Spatial and Spectral Brightness Enhancement of High Power Semiconductor Lasers", PhD Thesis (University of Rochester), ISBN: 9781321749861, 2015
[5] D. Campi et al., "Optical nonlinearities in multiple quantum wells: Generalized Elliott formula", Phys. Rev. B, Vol. 51, pp. 10719-10728, 1995

Acknoledgements

The authors gratefully acknowledge the whole Diode Fab Team of Prima Electro, led by R. Paoletti, and in particular P. Gotta and M. Rosso for providing devices and experimental support.

Numerical model of small signal modulation response for vertical-cavity surface-emitting lasers

M. Wasiak[1]*, P. Śpiewak[1], E. Pruszyńska-Karbownik[1], M. Gębski[1], P. Komar[1], J. A. Lott[2] and R. P. Sarzała[1]

1 Institute of Physics, Lodz University of Technology, Łódź, Wólczańska 219, 90-924, Poland

2 Institute of Solid State Physics and Center of Nanophotonics, Technische Universität Berlin, Hardenbergstraße 36, Berlin, Federal Republic of Germany

**michal.wasiak@p.lodz.pl*

Summary: We present our new model of small signal modulation (SSM) response curves for vertical-cavity surface-emitting lasers. This model takes into account electrical, optical and recombination processes. All the necessary parameters are calculated using numerical models without the necessity of fitting to experimental data. The SSM curves calculated using this model show a good prediction of subsequent experimental results and thus the model is valuable for VCSEL design and integrated system modeling.

1. Introduction

Vertical-cavity surface-emitting lasers (VCSELs) are commonly used as the light emitters in optical data communication systems. In such applications it is crucial that a laser's output can be modulated with very high frequencies of the order of GHz or tens of GHz. The small signal modulation (SSM) experiment is one standard method to measure the intrinsic SSM bandwidth and thus to determine the laser's ability to switch between low and high optical output emission states as a function of the input electric modulation frequency. Here we present results of our new model designed to calculate small signal modulation response characteristics, that is applicable to all VCSEL designs and if expanded may as well be valuable for the modelling and deign of vertical-external-cavity surface-emitting lasers (VECSELs)

2. Model

The laser's optical response to a voltage modulation depends on three primary factors:

1) the electrical properties of the laser;

2) the photon-carrier dynamics in the active region; and

3) the quality factor of the optical cavity.

A model addressing the first factor has already been developed in the Photonics Group at the Lodz University of Technology [1]. The quality factor of a cavity can be calculated using an optical model that finds optical modes and their complex wavelengths. A model describing photon-carrier dynamics based on two rate equations for semiconductor lasers is presented in, for example [2]. Our model uses a modification of the theory given in [2], but instead of fitting the parameters of this model to experiment, we calculate the parameters based on the results given by our computer model of continuous-wave operation of semiconductor lasers [3]. A model that does not require any fitted parameters enables an analysis of the impact of different and limitless modifications of the device structure with the goal of optimizing certain performance parameters and device figures-of-merit before the actual device fabrication.

3. Results

We model a GaAs-based, oxide-confined VCSEL designed and fabricated at TU Berlin [4]. First we simulate the static light-current-voltage (LIV) characteristics. Then, all the necessary parameters used in the dynamic model are calculated for the chosen values of the driving current. Figure 1 presents simulated SSM response curves (that is, scattering parameter magnitude S_{21} versus frequency) for the modelled VCSEL structure at three different values of the driving bias current. When the current increases, the resonance peak shifts towards higher frequencies, its height decreases, and the -3dB frequency (defined as the SSM bandwidth) increases. This in agreement with what is observed in experimental VCSEL S_{21} curves.

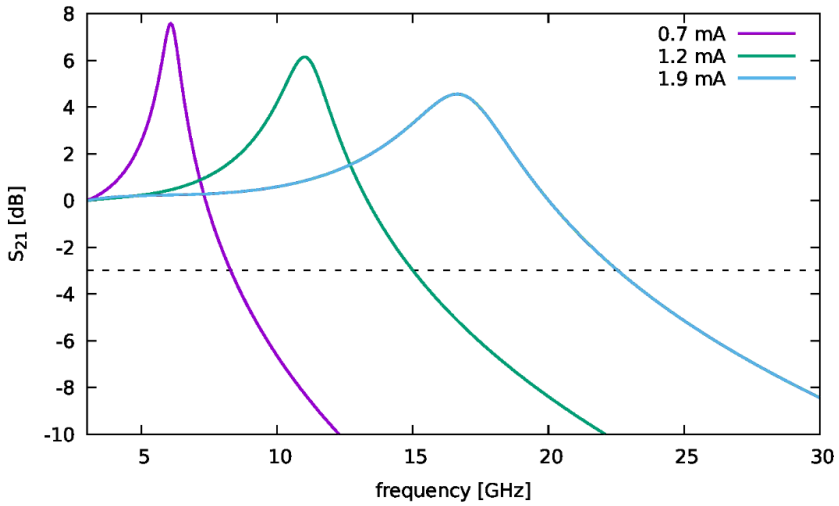

Figure 1: Calculated SSM response curves for different values of the driving current for a 4.2 μm oxide aperture diameter VCSEL produced by TU Berlin [4]. The dashed black line shows the -3dB level.

4. Conclusions

We have developed a model that allows us to calculate the SSM response curves for VCSELs without the need to fit the model to experimental results. We obtained qualitative agreement with experimental results, thus making our model highly vaulable for use in comparing and testing VCSEL designs and VCSEL geometries before accepting the expense and time of growing the epitaxial wafers and processing the VCSELs.

5. References

[1] M. Wasiak *et al.*, "Numerical model of capacitance in vertical-cavity surface-emitting lasers," Journal of Physics D: Applied Physics 49.17, 2016.

[2] R. P. Sarzała *et al.*, "Comprehensive self-consistent three-dimensional simulation of an operation of the GaAs-based oxide-confined 1.3-μm quantum-dot (InGa) As/GaAs vertical-cavity surface-emitting lasers", Optical and Quantum Electronics, 36(4), pp. 331-347, 2004.

[3] L. A. Coldren and S. W. Corzine, "Diode lasers and photonic integrated circuits", Chapter 5 Dynamic Effects, John Wiley & Sons, New York, NY, 1995.

[4] N. Haghighi, *et al.*, "Simplicity VCSELs", Proceedings of SPIE, Vol. 10552, 2018.

Acknowledgement

This work has been supported by Polish National Science Centre grant no. 2016/21/B/ST7/03532.

Impact of the laser structure and driving current on the modulation properties of a 980 nm GaAs-based VCSEL

E. Pruszyńska-Karbownik[1]*, P. Śpiewak[1], P. Komar[1], J. A. Lott[2], and M. Wasiak[1]

1 Institute of Physics, Lodz University of Technology, Łódź, Wólczańska 219, 90-924, Poland
2 Institute of Solid State Physics and Center of Nanophotonics, Technische Universität Berlin, Hardenbergstraße 36, Berlin, Federal Republic of Germany

**email:emilia.pruszynska-karbownik@p.lodz.pl*

Summary: We present results of numerical calculations of small signal modulation response for GaAs-based, oxide-confined vertical-cavity surface-emitting lasers. The results show that the VCSEL's -3 dB small signal bandwidth increases with driving current and its dependence on the cavity quality factor for a fixed value of the current is non-monotonic.

1. Introduction

Small and compact optical data transfer systems are replacing traditional data communication solutions in many applications, most especially in very short-reach and integrated systems. Semiconductor VCSELs, because of their small size, high efficiency, and the fact that they can be directly modulated at very high frequencies are widely developed for applications such systems. The modulation properties of a diode laser are determined by numerous factors that may depend on both the laser's construction and on the operating conditions.

A model developed by the Photonics Group at the Lodz University of Technology allows us to calculate the small signal modulation (SSM) response of vertical-cavity surface-emitting lasers (VCSELs). It is an extension of the existing static model [1,2,3]. Using this new SSM model we analyse the impact of the driving current and modifications of the VCSEL's epitaxial structure on the modulation properties.

2. Results

The modelled VCSEL is a GaAs-based, oxide-confined VCSEL emitting at around 980 nm [4]. Figure 1 shows the -3 dB bandwith f_{3dB} calculated for a laser structure with 15.5 pairs of the top distributed Bragg reflector (DBR) mirror as a fuction of the driving bias current. We use a variable high frequency modulation voltage on top of the bias voltage. Figure 2 presents results of simulations of SSM response of VCSELs differing from the above structure only in the number of the top DBR pairs. As one can see, for a fixed value of the driving current of 1.2 mA there is a maximum of the bandwidth.

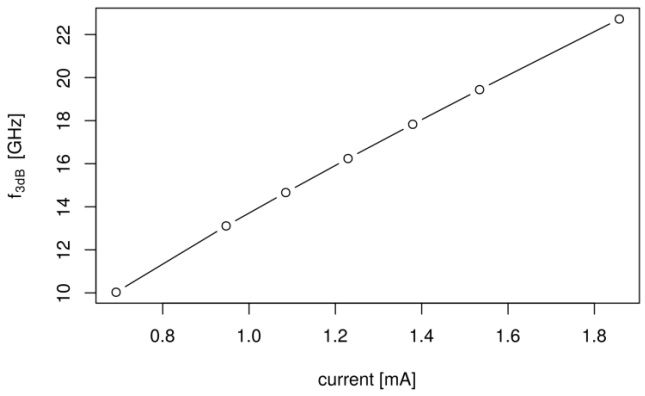

Figure 1: The simulated -3 dB small signal modulation bandwidth (f_{3dB}) as a function of the bias current in a 980 nm VCSEL with 15.5 top coupling DBR pairs.

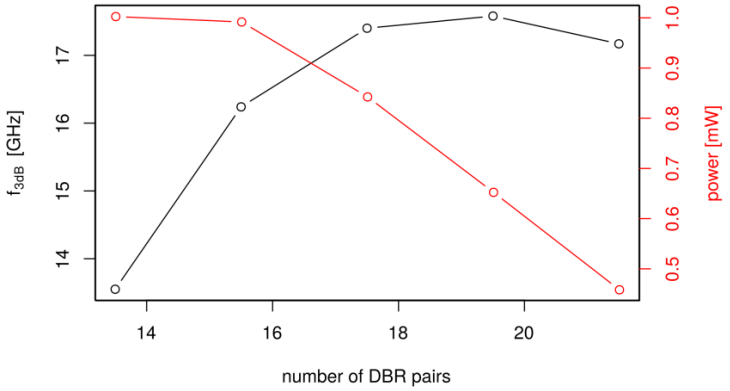

Figure 2: The simulated -3 dB small signal modulation bandwidth (f3dB) and the simulated emitted optical power as functions of the number of the top DBR pairs for the driving bias current of 1.2 mA.

3. Conclusions

The results of our calculations show that the f_{3dB} of a VCSEL increases with bias current, which is in line with general experimental observations. However, the dependence of f_{3dB} on the number of top DBR pairs (and hence the cavity Q-factor) is less trivial. There is a number of DBR pairs for which the -3 dB bandwidth has a maximum and this is not correlated with the maximum value of the emitted optical power.

4. References

[1] R. P. Sarzała *et al.*, "Comprehensive self-consistent three-dimensional simulation of an operation of the GaAs-based oxide-confined 1.3-μm quantum-dot (InGa) As/GaAs vertical-cavity surface-emitting lasers", Optical and Quantum Electronics, 36(4), pp. 331-347, 2004.

[2] M. Wasiak *et al.*, "Numerical model of capacitance in vertical-cavity surface-emitting lasers," Journal of Physics D: Applied Physics 49.17, 2016.

[3] M. Dems *et al.*, "PlaneWave Admittance Method — a novel approach for determining the electromagnetic modes in photonic structures ," Optics Express 13(9), pp. 3196-3207, 2005

[4] N. Haghighi, *et al.*, "Simplicity VCSELs", Proceedings of SPIE, Vol. 10552, 2018.

Acknowledgement

This work is supported by the Polish National Science Centre grant no. 2016/21/B/ST7/03532.

Coupled-Bloch-Wave Analysis of PhC Lasers

Marco Saldutti,[1]* Jesper Mørk[2], Paolo Bardella[1], Ivo Montrosset[1] and Mariangela Gioannini[1]

[1] *Dipartimento di Elettronica e Telecomunicazioni, Politecnico di Torino, Corso Duca degli Abruzzi 24, Torino, Italy*

[2] *DTU Fotonik, Department of Photonics Engineering, Technical University of Denmark, Ørsteds Plads, DK-2800 Lyngby, Denmark*

* *marco.saldutti@polito.it*

Abstract: A coupled Bloch-wave approach is employed to analyze active photonic-crystal (PhC) waveguides and cavities. The impact on group index of a generally complex refractive index perturbation is discussed. This perturbation couples the otherwise independent Bloch modes and limits the maximum attainable slow-light enhancement of gain.

1 Introduction

A major advantage of photonic crystal (PhC) line-defect waveguides is the slow-light (SL) enhancement of gain per unit length. In particular, PhC lasers based on line-defect waveguides, having ultralow threshold current, are ideal candidates for energy efficient light sources in high density PhC integrated circuits [1,2]. A rigorous, but computationally demanding approach to analyze PhC lasers is solving Maxwell-Bloch equations by a finite-difference-time-domain (FDTD) technique [3]. An alternative approach is represented by coupled-mode theory. In this work, we employ the theoretical approach of [4] to model an active PhC waveguide and we further exploit it to study a PhC laser in the frequency-domain as made up of an active PhC waveguide and two mirrors. In particular, we push further the formulation of [4] to generally take into account both a real and imaginary refractive index perturbation; therefore, we explicitly derive the Bloch modes of the perturbed waveguide and discuss the impact of the refractive index perturbation on their dispersion relation. Consistently with the rigorous, non-perturbative approach of [5], we show that the maximum attainable SL gain-enhancement is limited by the gain itself. These results could be also useful in further investigations of the impact of the gain-induced coupling on the threshold gain properties of PhC lasers.

2. Numerical model

The forward- $(+)$ and backward-propagating $(-)$ Bloch modes of the unperturbed, reference waveguide in the frequency-domain are denoted by $\boldsymbol{E}_{0,\pm}(\mathbf{r},\omega)=\mathbf{e}_{0,\pm}(\mathbf{r},\omega)e^{\pm ik_z(\omega)z}$, where $\mathbf{e}_{0,\pm}(x,y,z)=\mathbf{e}_{0,\pm}(x,y,z+a)$, with k_z propagation constant and a the PhC lattice constant. By expanding the electric field as $\mathbf{E}=\psi_+(z,\omega)\boldsymbol{E}_{0,+}+\psi_-(z,\omega)\boldsymbol{E}_{0,-}$, two coupled differential equations for $\psi_\pm(z,\omega)$ are derived [4]:

$$\begin{cases}\frac{\partial\psi_+(z,\omega)}{\partial z}=i\kappa_{11}(z,\omega)\psi_+(z,\omega)+i\kappa_{12}(z,\omega)e^{-i2k_z(\omega)z}\psi_-(z,\omega)\\ -\frac{\partial\psi_-(z,\omega)}{\partial z}=i\kappa_{21}(z,\omega)e^{i2k_z(\omega)z}\psi_+(z,\omega)+i\kappa_{11}(z,\omega)\psi_-(z,\omega)\end{cases}\qquad(1)$$

The self- and cross-coupling coefficients induced by the generally complex refractive index perturbation are written as $\kappa_{11;12;21}(z,\omega)=P\left[(\omega/c)\left(n_g(\omega)/n_s^2\right)/2\right]\Gamma_{xy,11;12;21}(z,\omega)$, where n_s and n_g are the slab material refractive index and the unperturbed waveguide group index, while P is a scaling factor depending on the refractive index perturbation. Specifically, $P\cong 2[n_s\Delta n_s+in_s\Delta n_i]$, where Δn_s and $\Delta n_i=-(c/\omega)\,g_0/2$ are, respectively, the real and imaginary refractive index perturbation, with g_0 being the active material gain. Confinement factors $\Gamma_{xy,11;12;21}(z,\omega)$ are given by

$$\Gamma_{xy,11}(z,\omega)=\frac{a\int_S\epsilon_0 n_s^2|\mathbf{e}_0(\mathbf{r},\omega)|^2F(\mathbf{r})\mathrm{d}S}{\int_V\epsilon_0 n_b^2(\boldsymbol{r})|\mathbf{e}_0(\mathbf{r},\omega)|^2\mathrm{d}V}\qquad\Gamma_{xy,12}(z,\omega)=\frac{a\int_S\epsilon_0 n_s^2\left[\mathbf{e}_{0,-}(\mathbf{r},\omega)\cdot\mathbf{e}_{0,+}^*(\mathbf{r},\omega)\right]F(\mathbf{r})\mathrm{d}S}{\int_V\epsilon_0 n_b^2(\boldsymbol{r})|\mathbf{e}_0(\mathbf{r},\omega)|^2\mathrm{d}V}$$

with $\Gamma_{xy,21}=\Gamma_{xy,12}^*$; V is the volume of a PhC supercell, S the transverse section at z and $n_b(\mathbf{r})$ the background refractive index, whereas $F(\mathbf{r})=1\,(=0)$ in the slab (holes). Due to the z-periodicity of $\mathbf{e}_{0,\pm}$ and $F(\mathbf{r})$, the coupling coefficients are periodic with z. By putting $\psi_\pm=c^\pm e^{\mp ik_z z}$, equations in (1) are turned into a system of two coupled differential equations in $c^\pm(z,\omega)$ with periodic coefficients. Therefore, $c^\pm$ at the input and output of the generic N_{th} cell are related by $[c_N^+(\omega)\;\;c_N^-(\omega)]^{\mathrm{T}}=\mathbf{T}_a(\omega)[c_{N-1}^+(\omega)\;\;c_{N-1}^-(\omega)]^{\mathrm{T}}$, where $\mathbf{T}_a$ is the unit cell transmission matrix. The eigenvectors $\boldsymbol{u}_1=[u_{11}\quad u_{21}]^T$ and $\boldsymbol{u}_2=[u_{12}\quad u_{22}]^T$ of $\mathbf{T}_a$ are the Bloch modes of the perturbed waveguide. The corresponding eigenvalues are $\lambda_{1,2}=e^{\pm i\phi_B(\omega)}$. Therefore, ϕ_B is the phase-shift per cell of $\boldsymbol{u}_1$ and $\boldsymbol{u}_2$, i.e. the dispersion relation of the Bloch modes of the perturbed waveguide. Consequently, the perturbed waveguide group index is readily obtained as $n_{g,pert}(\omega,P)=c\,\mathrm{Re}\{\partial\phi_B(\omega,P)/\partial\omega\}$. Within this approach, a PhC laser of N cells consists of the cascade of an active PhC waveguide and two mirrors (see inset of Fig. 2b). The waveguide transmission matrix is $\mathbf{T}_a^N$, while the mirrors are modelled, for simplicity, with a frequency-independent reflection coefficient. The cavity loop gain (LG) is computed as the product, at a given reference plane, of the left and right field reflectivity.

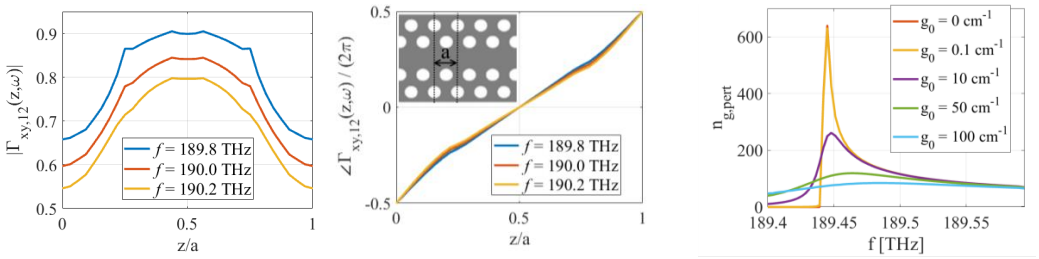

(a) (b) (c)

Fig.1. (a) Magnitude and (b) phase of $\Gamma_{xy,12}$, at different frequencies, for the same line-waveguide of PhC lasers in [2]; inset in (b): unit cell reference planes. (c) Group index of the perturbed waveguide with $\Delta n_s = -0.001$ and various g_0 values.

3. Simulation results

The unperturbed, reference structure is the passive line-defect waveguide on which the PhC lasers realized in [2] are based. Magnitude and phase of the corresponding $\Gamma_{xy,12}(z,\omega)$ are shown in Fig. 1a and 1b at different frequencies. On this basis, the impact of a generally complex refractive index perturbation on the waveguide group index can be analyzed, as shown in Fig. 1c. Firstly, we consider the case a purely real refractive index perturbation, i.e. $\Delta n_s = -0.001$ and $g_0 = 0$. The group index diverges at $f \cong 189.45$ THz, which is the band-edge of the perturbed waveguide, and is zero at smaller frequencies. Indeed, these frequencies correspond to the stopband of the perturbed waveguide. Secondly, we gradually add gain to the same waveguide. As g_0 increases, the group index is gradually reduced in the passband of the waveguide with purely real refractive index perturbation, thus limiting the SL gain-enhancement; on the contrary, it gradually increases in the stopband, where the previously evanescent Bloch modes have now become propagative. This is consistent with results reported in [5].
With this coupled Bloch-wave approach, we have then modelled the PhC lasers presented in [2], with the left and right mirror reflectivity set to $r^2 = 0.98$. The inset of Fig. 2b displays a scheme of the cavity, with the field reflectivity from the left facet towards the cavity denoted by $r_{eq,R}$. The threshold condition is the level $1/r$, corresponding to the horizontal line in Fig. 2a. The red spots track the longitudinal resonant mode M_1, with frequency $f = 191$ THz, as it approaches the lasing onset at $g_0 = 16.2\ \mathrm{cm}^{-1}$. The frequency shift of mode M_1 towards the SL region as the cavity length increases (Fig. 2c) is consistent with the experimental [2] and numerical [3] trends.

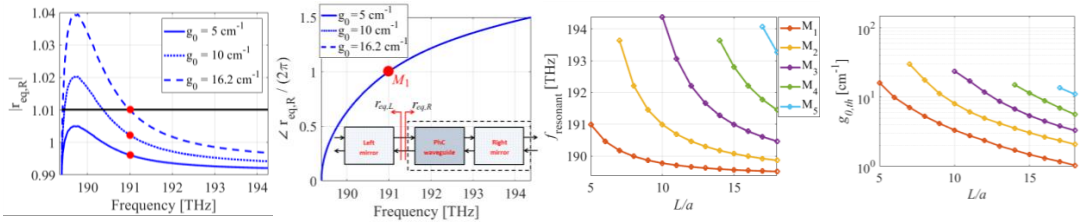

(a) (b) (c) (d)

Fig. 2. Magnitude of $r_{eq,R}$, at different g_0, for $L = 5a$; black line is level $1/r$. (b) Phase of $r_{eq,R}$; inset: scheme of the cavity. (c) Mode frequencies versus cavity length. (d) Threshold gain for the onset of lasing of the various modes.

4. Conclusions

In conclusion, the impact on group index of both a real and imaginary refractive index perturbation has been analyzed. This analysis could be useful for future investigations of the lasing mode threshold gain properties of PhC lasers.

5. References

[1] S. Matsuo et al., IEEE J. Sel. Top. Quantum Electron., 19, 4, (2013).
[2] W. Xue et al., PRL, 116, 063901 (2016).
[3] J. Cartar et al., PR, A 96, 023859 (2017).
[4] Y. Chen et al., PR. A 92, 053839 (2015).
[5] J. Grgić et al., PRL, 108, 183903 (2012).

Computer modeling of a nitride tunnel junction VCSEL

P. Śpiewak*, M. Wasiak and R. P. Sarzała

Institute of Physics, Lodz University of Technology, Łódź, Wólczańska 219, 90-924, Poland
**patrycja.spiewak@edu.p.lodz.pl*

Summary: We present numerical simulations of a nitride VCSELs (Vertical-Cavity Surface-Emitting Lasers) created at the University of California, Santa Barbara (UCSB). These structures have dual dielectric DBRs (Distributed Bragg reflector). The results show how the construction and material parameters like: the length of the resonator, absorption in n-GaN influence the laser threshold parameters and the emitted power. We considered also different values of the efficiency of carriers injection into the active area.

1. Introduction

Operation characteristics of the existing structures of nitride VCSELs do not yet meet commercial requirements. In VCSELs with dielectric DBRs, it is important to ensure an efficient heat transfer mechanism. Effective heat transfer can be obtained by using lasers with long resonators, which have thick n-GaN layer. This thick n-GaN layer enables better heat spreading. On the other hand, a long resonator causes large losses due to optical absorption, which has an adverse effect on the optical properties of the device.

We present numerical simulations of nitride VCSELs created at the University of California, Santa Barbara (UCSB) [1]. Our results show how: the length of the resonator and absorption within it influences the laser performance. The calculations were done using a self-consistent thermal-electrical-recombination-optical model developed by the Photonics Group at the Lodz University of Technology [2].

2. Simulated Structure

The analyzed structure is designed to emit a 405 nm wavelength. The original structure had a 23λ resonator. Both DBRs are made of Ta_2O_5/SiO_2. Because the bottom DBR is made of dielectric materials, the n-type contact is in the form of a gold ring surrounding this DBR. Such bottom contact helps also to remove heat from the laser. The active area consist of two 14 nm/1nm InGaN/GaN quantum wells (QWs). The electrical aperture of analyzed structure is confined by lateral Al ion implanted areas. Scheme of this structure is presented in Figure 1. The length of the resonator was changed by reduction the thickness of the n-GaN layer above the active area.

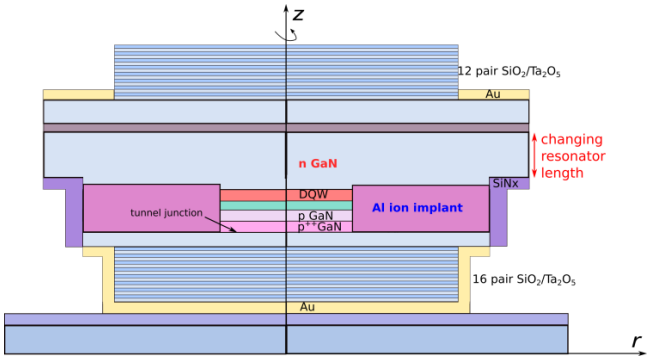

Figure 1: Scheme of the analyzed structure of nitride VCSEL.

3. Sample results

Figure 2 presents experimental and simulation current-voltage (*I-V*) characteristics for the analyzed structure. Figure 2 also show light-current (*L-I*) characteristics for lasers with 10λ and 20λ resonators of 23.5 cm^{-1} absorption in n-GaN layer. The five values of carrier injection efficiency into the active area (η_{inj}): 60%, 65%, 70%, 80%, 90% are considered. For shorter resonator (10λ), the maximal output power is more than two times higher than for the long resonator (20λ).

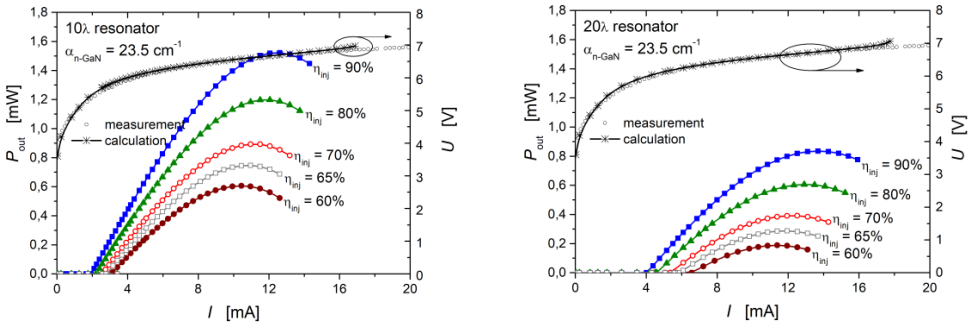

Figure 2: LIV characteristics for 10λ (left) and 20λ (right) resonators for different injection efficiency, the absorption in n-GaN layer is $\alpha_{n\text{-}GaN} = 23.5\ cm^{-1}$. *U*(*I*) measurement characteristics are from [1].

4. Conclusions

Our above-threshold analysis shows that absorption in n-GaN has great influence on the laser performance, because the resonator is built mainly from n-GaN. Whereas lasers with thicker resonators have lower thermal resistances, the increased absorption deteriorates the emitted power.

[1] Charles A. Forman, et al., Forman, Charles A., et al. "Continuous-wave operation of m-plane GaN-based vertical-cavity surface-emitting lasers with a tunnel junction intracavity contact", Appl. Phys. Lett. 112, 111106, 2018.
[2] R. P. Sarzała, et al., "Comprehensive self-consistent three-dimensional simulation of an operation of the GaAs-based oxide-confined 1.3-μm quantum-dot (InGa) As/GaAs vertical-cavity surface-emitting lasers", Opt. Quantum Electron., vol. 36, no. 4, pp. 331–347, 2004.

Acknowledgements

This work has been partially supported by Polish National Science Centre (2016/21/B/ST7/03532) and the Polish Ministry of Science and Higher Education.

A Multiphysics Electro-thermo-opto VCSEL Simulator

A. Tibaldi[1]*, F. Bertazzi[1,2], M. Goano[1,2], M. Daubenschüz[3], R. Michalzik[4], and P. Debernardi[1]

1 Istituto di Elettronica e di Ingegneria dell'Informazione e delle Telecomunicazioni, Consiglio Nazionale delle ricerche c/o Politecnico di Torino, Corso Duca degli Abruzzi 24, 10129, Torino, Italy [(TO) necessary? Saves an entire line in 2]
2 Dipartimento di Elettronica e Telecomunicazioni, Politecnico di Torino, Corso Duca degli Abruzzi 24, 10129, Torino, Italy
3 Philips GmbH, U-L-M Photonics, Lise-Meitner Straße 13, 89081, Ulm, Germany
4 Institute of Functional Nanosystems, Ulm University, Albert-Einstein-Allee 45, 89081, Ulm, Germany
**alberto.tibaldi@ieiit.cnr.it*

Summary: Since the lasing operation of vertical-cavity surface-emitting lasers results from the interaction of electrical carrier transport, optical and thermal effects, a realistic model should include each of them and their interplay. Aiming to such an achievement, this paper presents our in-house Vcsel Electro-opto-thermal Numerical Simulator VENUS, consisting of the 3D vectorial optical code VELM, a model for the quantum well optical response, a heat equation solver and a quantum-corrected drift-diffusion simulator. Each of these components and their coupling strategy is described, and the resulting model is validated through the comparison with experimental results.

1 Introduction

After consolidating their dominating role in several mass applications like laser mice and datacom, vertical-cavity surface-emitting lasers (VCSELs) are becoming key components in several other fields such as smartphone 3D cameras and LiDAR systems [1, 2, 3]. This fascination of the market for VCSELs is caused by their inexpensiveness, reliability, testability and low power consumption, which make them ideal for use in portable devices. Unfortunately, the VCSEL design is a rather complex task. In fact, most of the commercially available devices have been designed by means of extensive trial-and-error prototyping campaigns. An obvious alternative to such inefficient and expensive approaches is given by computer-aided design (CAD) techniques aimed at replacing several experimental prototyping steps with simulations, cutting down the design costs.

In an effort to advance in this field, in this work we introduce our VCSEL Electro-opto-thermal [see above] NUmerical Simulator (VENUS). To this aim, the main model constituents are described in Section 2, while Section 3 presents some preliminary results.

2. Description of the model

VENUS consists of four main building blocks: the 3D vectorial Vcsel ELectroMagnetic (VELM) optical code, a model describing the optical response of the active region, a heat equation solver and a quantum-corrected drift-diffusion simulator.

VELM is based on expanding the electromagnetic field in each VCSEL layer in terms of the cylindrical waves of a reference medium, and all the variations with respect to it are accounted for by coupled mode theory, allowing to describe the transverse details of the structure. From the coupling matrix it is possible to obtain a transfer matrix for each layer, and then the transfer matrix of the whole device. By enforcing continuity conditions at the terminating interfaces and by requiring the round-trip self-consistency it is possible to obtain an eigenproblem, whose solutions are the VCSEL modal wavelengths and losses, and the field profiles.

The *optical response* of the quantum wells (QWs), i.e., the stimulated gain, the spontaneous emission and the carrier-induced refractive index variation, is carried out by applying Fermi's golden rule on the QW sub-bands. These sub-bands are calculated by a $\mathbf{k} \cdot \mathbf{p}$ finite element method applied to a 1D nanostructure, where the Hamiltonian is reduced to 4×4 (including the electrons, heavy and light holes, and the split-off band) by the axial approximation.

The *thermal problem* requires to deal with regions characterized by different physical behaviors: the substrate, where a quasi-linear temperature increase occurs, and the active region, which is characterized by steep temperature variations. Starting from this observation, we developed a numerical scheme based on the spectral element method. This is based on decomposing the problem domain into subdomains, where basis functions characterized by different orders are defined. In such a way, it is possible to approximate the solution with different resolutions in the different subdomains, optimizing the model accuracy and computational efficiency. The heat sources included in the model are the Joule effect, capture heating, optical absorption, non-radiative recombinations and Thomson/Peltier effects.

The *carrier transport* model must be chosen as a trade-off between the desired accuracy for the description of the active quantum regions, where the electro-optical interactions take place, and the computational resources required to simulate the whole device, including distributed Bragg reflectors (DBRs) and the substrate; this led

to the choice of the drift-diffusion framework. In addition to the "standard" Poisson and carrier continuity equations, a special treatment of quantum regions is introduced, which is based on separating carriers into two sub-populations: bulk carriers, whose transport is described by standard drift-diffusion, and bound carriers, which are distributed along the confinement direction according to their envelope wave functions and can move freely in the lateral directions.

Finally, the electrical and optical models are coupled by means of photon rate equations, accounting for spontaneous and stimulated emission processes obtained from the active region optical response.

3. Preliminary results

Figure 1 reports some preliminary results obtained with VENUS. The room-temperature simulated device is an oxide-confined 5 μm aperture multi-mode VCSEL realized at Philips Photonics. Good agreement is achieved between simulations (solid blue curves) and experiments (reported in red). Future papers will deal with additional calibration of the VENUS model parameters, especially investigating their temperature dependence, and its application to novel devices.

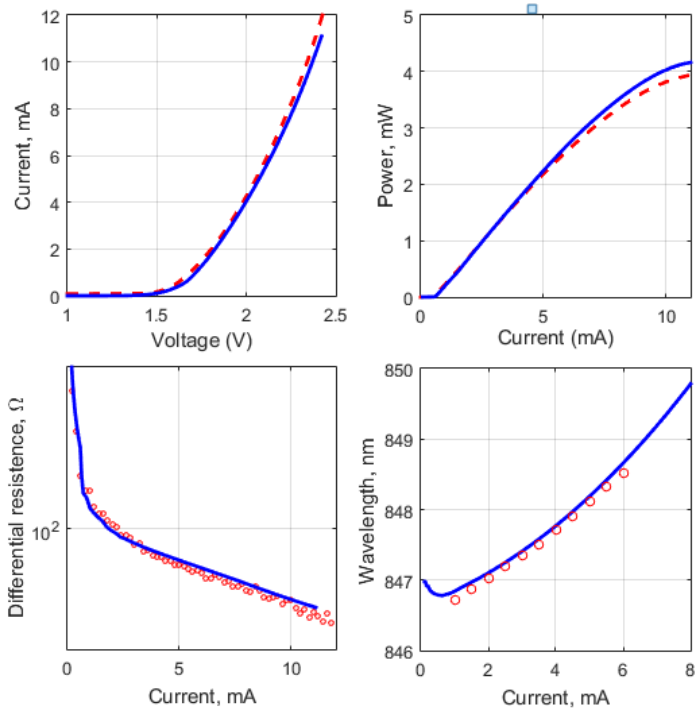

Figure 1: Comparison of main simulation and experimental results. Top left: current-voltage characteristics, top right: light-current characteristics; bottom left: differential resistance versus current. The wavelength versus current curve (bottom right) is shown for the fundamental mode and on a reduced current span due to a limited set of experimental spectra. Simulations and measurements are indicated with blue (full lines) and red colors, respectively.

4. References

[1] R. Michalzik, ed., "VCSELs: Fundamentals, Technology and Applications of Vertical-Cavity Surface-Emitting Lasers," *Springer-Verlag*, Berlin, 2013.
[2] K. J. Ebeling, R. Michalzik, and H. Moench, "Vertical-cavity surface-emitting laser technology applications with focus on sensors and three-dimensional imaging," *Jpn. J. Appl. Phys.*, vol. 57, pp. 08PA02-1–11, 2018.
[3] H. Moench, M. Carpaij, P. Gerlach, S. Gronenborn, R. Gudde, J. Hellmig, J. Kolb and A. v. d. Lee, "VCSEL based sensors for distance and velocity," Proc. SPIE 9766, pp. 97660A-1–16, 2016.

Acknowledgements

We would like to thank our colleagues from Philips Photonics Ulm for valuable discussions and support.

New type of vertical-cavity surface-emitting laser incorporating a monolithic high contrast grating mirror

M. Gebski[1, 2]*, J. A. Lott[1], and T. Czyszanowski[2]

1. Technische Universität Berlin, Institut für Festkörperphysik, Berlin, Federal Republic of Germany
2. Lodz University of Technology, Institute of Physics, Photonics Group, Łódź, Poland
**marcin.gebski@p.lodz.pl*

Summary: We present the first electrically-injected vertical-cavity surface-emitting laser (VCSEL) incorporating a monolithic high-contrast grating (MHCG) outcoupling mirror. Thanks to the MHCG mirror, this new type of VCSEL is thinner by 20 % with respect to the standard distributed Bragg reflector (DBR) VCSEL. Moreover, the device is a semiconductor-only device, since the MHCG mirror doesn't require a low refractive index material in the laser cavity, unlike the generic high-contrast grating (HCG) mirror VCSEL. Our VCSELs show continuous wave (CW) operation up to 75 °C and single-mode emission from threshold to rollover. Additionally, the devices show remarkable thermal stability expressed by a thermal resistance close to the record value of 0.6 W/K.

1. Introduction

Vertical-cavity surface-emitting lasers (VCSELs) are widely used in optical communication, laser printers, and optical mice. The state-of-the-art devices are of a standard design where a very short (optically about one wavelength) cavity is embedded between two high power reflectance ($R \geq 0.98$) distributed Bragg reflectors (DBR). Such a design can easily be realized for a relatively low price in the gallium arsenide (GaAs)/aluminum-gallium arsenide (AlGaAs) material system where a very low lattice mismatch and similar thermal properties of those materials enable the MOVPE growth of monolithic laser cavities. Unfortunately, the emission wavelength from GaAs-based devices is limited to ~600 - 1100 nm range by the available active regions (excluding 1310 and 1550 nm dilute-nitride VCSELs on GaAs). To extend the emission wavelength range beyond this region, VCSELs should be made based on different materials such as gallium nitride (GaN, ~390-580 nm), indium phosphide (InP, ~1.3-1.6 μm), or gallium antimonide (GaSb, ~1.8-4 μm). For those materials however, there are no lattice-matched, high R DBRs available.

As a solution for this problem, we proposed in [1] a monolithic high-contrast grating (MHCG) as a VCSEL mirror. The MHCG is a special kind of a wide class of subwavelength grating reflectors (SGR). It can be designed to provide very high R for any wavelength from ultraviolet (UV) to infrared (IR). It can be made of most of the common semiconductors used in optoelectronics [2]. The very same idea (called GIRO-grating reflector) was first proposed by Goeman *et al.* in [3], and later experimentally verified by Lee *et al.* in [4]. Unlike the high refractive index contrast gratings (HCG), the MHCG doesn't require low refractive index material below the grating and hence can be monolithically integrated with the rest of a VCSEL cavity creating an all-semiconductor cavity without any air-gap or dielectric layer under the grating. In this work we present the first experimental realization of a new type of VCSEL with a hybrid MHCG and DBR top mirror emitting at 980 nm. Since the MHCG can be designed for any wavelength in, for example GaN, InP, Si, or GaSb, the same idea can be used to make a VCSEL emitting from the UV to the IR.

2. Design and experiment

In Figure 1a we present the simulated one-dimensional optical field intensity distribution and the real part of the refractive index profile in the top-most part of the 980 nm MHCG-DBR VCSEL. The first layer from the surface is undoped GaAs in which an MHCG mirror is patterned (marked in grey) followed bythin undoped InGaP lattice-matched to a (p+)GaAs etch-stop layer, a (p)GaAs phase-matching spacer layer (that also spreads injected current), followed in turn by a 5.5 period (p)GaAs/AlGaAs DBR, a λ/2-thick optical cavity, and a 37 period (n)GaAs/AlGaAs bottom DBR (only the first two periods of the bottom DBR are shown). In Figure 1b we show a top down scanning electron microscope (SEM) image of a processed MHCG-DBR VCSEL with an oxide-aperture-diameter ϕ ~16.5 μm. The MHCG grating is designed to provide R ~0.99 at 980 nm for TM-polarized light (thus the only non-zero component of the electric field is perpendicular to the MHCG stripes). The period, fill factor (defined as the stripe width divided by the grating period), and grating height are 500 nm, 0.45, and 241 nm, respectively. The (u)GaAs layer is patterned by electron beam lithography and dry-etched using reactive ion etching (RIE) to form the MHCG. Next, we process the VCSELs using our standard planar techniques including UV lithography, RIE mesa etching, selective thermal oxidation in water vapor at 420 °C, lift-off metallization, and BCB planarization.

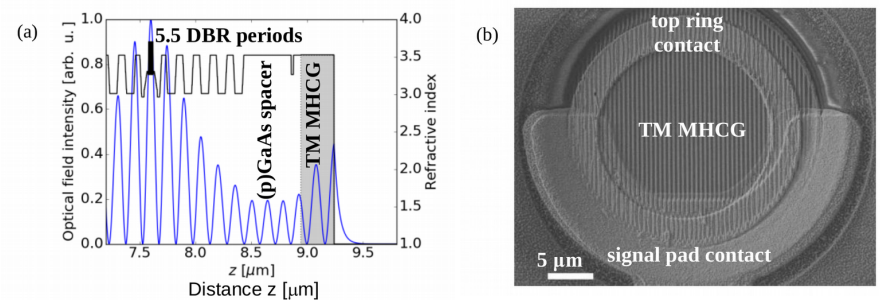

Figure 1. a) Simulated one-dimensional optical-field intensity on resonance and real refractive index profile of the 980 nm MHCG-DBR VCSEL; and b) scanning electron micrograph of the VCSEL, showing the TM-polarized MHCG, top surface p-metal ring contact, and part of the anode p-metal signal pad contact.

In Figure 2a we show the static L-I-V curves of one of the devices with ϕ ~16.5 μm taken at temperatures from 15 to 75 °C in 10 °C steps. The maximum optical output power at rollover is 450 μW at a forward bias current of 27 mA at 15 °C. The minimum threshold current is 7 mA at 15 °C. The emission spectra at 15 to 75 °C is shown in Figure 2b. The VCSEL emits with two-lateral modes from threshold to rollover. We obtain single-lateral-mode emission for our VCSELs with ϕ ~13.5 μm and explain in the presentation the relationship between ϕ, the MHCG design and the modal emission.

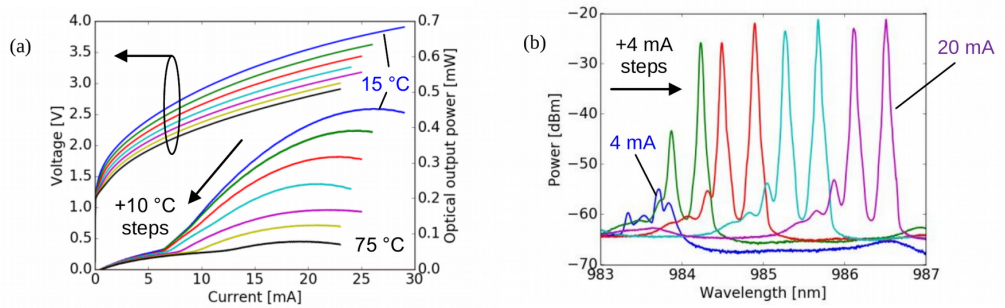

Figure 2. a) Continuous wave (CW) L-I-V characteristics of a 980 nm MHCG-DBR VCSEL with an estimated oxide aperture diameter of ϕ ~16.5 μm at temperatures from 15 to 75 °C in 10 °C steps; and b) 25 °C CW emission spectra for the VCSEL in a) at forward bias currents of 4 to 20 mA in 4 mA steps.

3. Conclusions

We present a new type of VCSEL with a hybrid MHCG and DBR top coupling mirror. Since most of the top DBR mirror is substituted by the MHGC we manage to decrease the overall thickness and volume of the device by ~20 %. Our VCSELs show CW quasi-single-mode and double-mode emission for ϕ ~13.5 and 16.5 μm, respectively, from threshold to rollover, for temperatures from 15 to 75 °C. The devices show a very high thermal stability which is expressed by a near record small thermal resistance of 0.6 K/W. Since the MHCG can be designed to provide a very high-power reflectance at any wavelength, the results presented in this work can be extrapolated to wavelengths different from 980 nm.

4. References

[1] M. Gębski, *et al.*, "Monolithic subwavelength high-index-contrast grating VCSEL," *IEEE Photonics Technol. Lett.* vol. 27, no. 17, pp. 1953-1956, Sep. 2015.

[2] M. Gębski, *et al.*, "Monolithic high-index contrast grating: a material independent high-reflectance VCSEL mirror," *Optics Express*, vol. 23, no. 9, pp. 11674-11686, 2015.

[3] S. Goeman, *et al.*, "First demonstration of highly reflective and highly polarization selective diffraction gratings (GIRO-gratings) for long wavelength VCSELs," *IEEE Photonics Technol. Lett.*, vol. 10, no. 9, pp. 1205–1207, Sep. 1998.

[4] J. Lee, *et al.*, "Polarization dependent GaN surface grating reflector for short wavelength applications," *Optics Express*, vol. 17, no. 25, pp. 22535–22542, Dec. 2009.

Acknowledgements

This work is supported by the German Research Foundation via the Collaborative Research Center 787 and partially supported by the Polish National Science Centre (PNSC) through the project OPUS 2014/15/B/ST7/05258. M. Gębski acknowledges support from the PNSC within the projects PRELUDIUM 2013/11/N/ST7/02826 and ETIUDA 2015/16/T/ST7/00514.

Trade-off in High Bandwidth versus High Optical Output Power in 980 nm VCSELs

N. Haghighi[1]*, G. Larisch, and J. A. Lott

Institute of Solid State Physics, Technical University Berlin,
Hardenbergstrasse 36, D-10623, Berlin, Federal Republic of Germany
**nasibeh.haghighi@tu-berlin.de*

Summary: Vertical-cavity surface-emitting lasers with relatively large aperture diameters of an estimated 12 to 16 μm emitting at about 980 nm exhibit room temperature small-signal modulation bandwidths of 24 to 23 GHz and maximum optical output powers of 19 to 25 mW.

1. Motivation and Experiment

Emerging applications for vertical-cavity surface-emitting lasers (VCSELs) include time-of-flight sensing for focusing, light-detection and ranging for automobile and drone proximity sensing, three-dimensional imaging and tracking for smartphones, and free-space optical interconnections for data centers, mesh networks, and backhaul networks. We envision low-cost and highly flexible VCSEL-based free-space optical links with data capacities of 10-100 Gb/s across distances of meters to several kilometers. We thus require light sources with moderate to large optical output power and simultaneously moderate to large bandwidth. We increase the optical output power of VCSELs by increasing their aperture diameters (ϕ), by using arrays of VCSELs, or both. In contrast we increase the small-signal modulation bandwidth of VCSELs by decreasing their ϕ. We investigate the optical power-bandwidth trade-off in VCSELs that are similar to our earlier *Simplicity* designs [1-4]. We now use a bottom distributed Bragg reflector (DBR) with predominantly binary (GaAs/AlAs) periods and we use 15.5 periods of $Al_xGa_{1-x}As$ (x=0.0 and 0.9) in our top coupling DBR to boost our optical output power. We achieve a record room temperature small-signal modulation bandwidth (f3dB) of of 23 GHz for our ϕ~16 μm 980 nm VCSELs.

2. Results

In Figure 1 (left) we show the static light-output-power vs. current (LI) and current-voltage (I-V) characteristics for our VCSELs with ϕ~4 μm and ϕ~16 μm at ~25°C (room temperature - RT). We estimate ϕ based on: 1) selective oxidation tests performed prior to VCSEL fabrication including scanning electron microscopy imaging; 2) the measured emission spectra and LIV characteristics; and 3) our experience gained from device fabrication cycles. We characterize groups of 16 VCSELs, where each group forms one column on our processed quarter-wafer piece. The top Mesa 1 diameter is 18, 18.5, 19, 19.5, 20, 21, 22, 23, . . ., 31 μm in each column, and the device-to-device pitch is 600 μm. We oxidize all VCSELs simulataneously such that the VCSEL with an 18 μm Mesa 1 diameter has ϕ~2.5 μm. For the ϕ~16 μm VCSEL with a 31 μm Mesa 1 diameter at 25°C the maximum L-I slope efficiency is ~0.95 W/A and the maximum optical output power at rollover is about 26 mW. The peak optical output power of the ϕ~4 μm VCSEL with a 19.5 μm Mesa 1 diameter is about 7 mW at 25°C. The maximum external differential quantum efficiency $\eta = (q\lambda_o/hc)\cdot(\Delta L/\Delta I)$ for all 16 VCSELs in the given column is within 0.67 to 0.75.

In Figure 1 (right) we show the measured emission spectra for three of the VCSELs: 1) above threshold for the ϕ~4 μm VCSEL; 2) just at threshold for the ϕ~10 μm VCSEL; and 3) just below threshold for the ϕ~16 μm VCSEL (the RT fundamental LP01 lasing mode of this VCSEL is at 985.3 nm). The ϕ~4 μm VCSEL at RT emits in a quasi-single-mode near theshold, whereas all larger VCSELs emit in multiple-modes at all bias forward currents above threshold.

In Figure 2 (left) we show the small-signal modulation response (i.e. the S21 curves) at 25°C of the ϕ~16 μm VCSEL at RT at bias currents of 10.75, 20.50, and 33.50 mA. The maximum f3dB is 23.2 GHz. In Figure 2 (right) we graph the maximum f3dB versus ϕ. The bandwidths vary from about 31 GHz for the smallest VCSELs to record values of 22-23 GHz for the largest ϕ~15 and 16 μm VCSELs where the peak output power is ~22 and 26 mW. Also in Figure 2 (right) for the given static bias current that gives us the maximum f3dB we plot the resultant static optical output power taken from the L-I-V as a function of ϕ.

3. Conclusions

Our new *Simplicity* 980 nm VCSEL design with a predominantly binary (AlAs/GaAs) bottom DBR to improve heat dissipation gives us a record maximum room temperature bandwidth of about 23 to 24 GHz for large oxide aperture VCSELs with ϕ~16 to 12 μm, respectively. We anticipate further improvements in both maximum f3dB and maximum optical output power for our VCSELs by employing novel electrically-parallel array geometries.

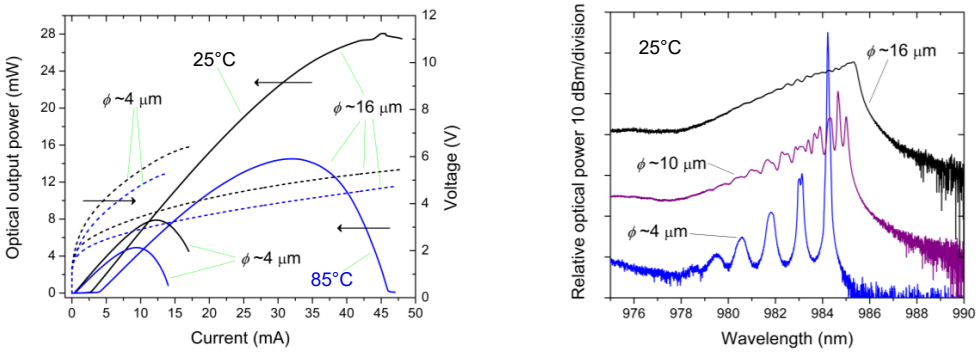

Figure 1: (left) Optical output power (solid lines) and voltage (dashed lines) versus current for VCSELs with ϕ~4 and 16 µm at 25°C (black lines) and 85°C (blue lines). The ϕ are estimated to be ±1 µm. (right) Emission spectra at 25°C for 980 nm VCSELs: a) above threshold for ϕ~4 µm (blue line); b) at threshold for ϕ~10 µm (purple line); and c) just below threshold for ϕ~16 µm (black line).

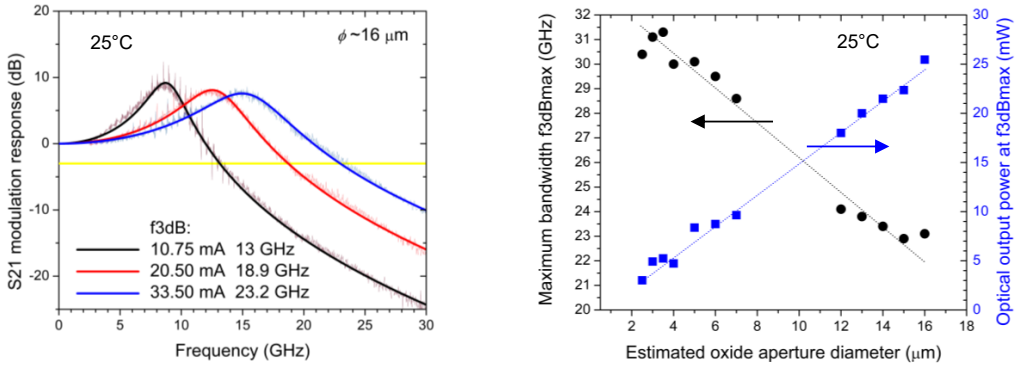

Figure 2: (left) Small-signal modulation response (S21) at three increasing static bias currents for a 980 nm VCSEL with ϕ~16 µm at 25°C. (right) Maximum -3 dB small-signal modulation bandwidth f3dBmax (circles) versus ϕ (±1 µm) for 980 nm VCSELs at 25°C and static optical output power at the bias current giving f3dBmax (squares).

4. References

[1] N. Haghighi et al., "Small oxide-aperture-diameter 980-nm VCSELs," WeP3, Proceedings International Nano Optoelectronic Workshop, Tianjin and Qian'an, People's Republic of China, 04-12 August 2017.
[2] J. A. Lott, "Simplicity VCSELs," Proceedings 7th Workshop on Physics and Technology of Semiconductor Lasers, Krakow, Poland, 15-18 October 2017.
[3] R. Rosales et al., "30-GHz bandwidth with directly current modulated 980-nm oxide-aperture VCSELs," IEEE Photonics Technol. Lett., vol. 29, no. 23, pp. 2107-2110, December 2017.
[4] N. Haghighi et al., "High bandwidth versus high optical output power in 980 nm VCSELs," HL 36.7, German Physical Society (Deutsche Physikalische Gesellschaft - DPG) Spring Meeting, Berlin, Germany, 11-16 March 2018.

Acknowledgements

This work is supported by the German Research Foundation (Deutsche Forschungsgemeinschaft - DFG) via the Collaborative Research Center (Sonderforschungsbereich) 787.

Electrically-pumped wafer-fused VECSELs emitting at 1550-nm wavelength range

A. Mereuta[1]*, A. Caliman[2], A. Rudra[1], G. Suruceanu[2], and Eli Kapon[1]

[1]*Ecole Polytechnique Fédérale de Lausanne (EPFL), 1015 Lausanne, Switzerland*
[*]*alexandru.mereuta@epfl.ch*
[2]*LakeDiamond SA, Rue Galilée 7, 1400 Yverdon-les-Bains, Switzerland*

Summary: We report on the design, fabrication and characterization of electrically pumped vertical external cavity surface emitting lasers (EP-VECSELs) emitting at 1550-nm wavelength range. We demonstrate up to 20-mW CW output power at 15°C from devices with 50-µm aperture, which represents to our knowledge the highest power value reported so far for EP-VECSELs in the 15XX-nm wavelength band.

1. Introduction

Vertical-external-cavity surface emitting lasers (VECSELs) emitting in the 1.3-1.6-µm waveband are useful in applications such as optical pumping, gas spectroscopy, and frequency doubling. Significant progress has been achieved in this area with optically pumped devices [1,2], while long wavelength electrically pumped VECSELs are so far limited up to 6-mW of continuous wave (CW) emission power [3,4], mainly due to their complexity of fabrication and testing.

Here we report on 1.55-µm EP-VECSELs, fabricated by wafer fusion and using flip-chip bonding. Lasing up to 20-mW of CW output power was reached from devices with 50-µm aperture at 15°C by employing 7 InAlGaAs compressively strained QWs and using InP-based partial DBR for differential resistance reduction.

2. Design and fabrication

The schematic presentation of the mirror gain structure of the 1550-nm EP-VECSEL is shown on Figure 1. The InP-based active region, grown by MOVPE, includes one group of 7 InAlGaAs strained compensated QWs placed in an antinode of the electric field distribution, an n^{++}/p^{++} InAlGaAs tunnel junction (TJ), an InAlAs/InP p-n junction, a top n-InP-spacer, and a bottom n-InP current spreading layer. The aperture size is defined by the diameter of the tunnel junction that injects carriers into the active region. In this work different TJ diameters, from 10 to 100-µm, were defined by lithography and have been overgrown with n-InP in a second growth step on the same wafer.

By applying the wafer fusion technique [5], the active region is sandwiched between a top low reflectivity 6 pair-InAlGaAs/InP n-type DBR (partial DBR) and an undoped bottom high reflectivity 21 pair - AlAs/GaAs DBR, both grown by MOVPE on (100) InP and GaAs substrates, respectively, with the stop band centered at ~1550-nm.

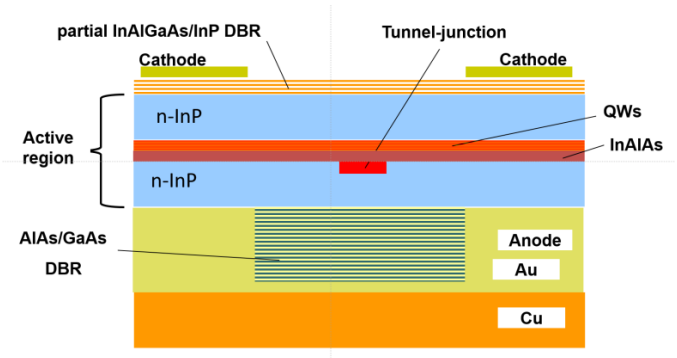

Figure 1. Schematic cross-section of the wafer-fused EP-VECSEL gain-mirror structure.

After selective GaAs substrate removal, the DBR-side of the fused-structure was structured and metalized with Ti/Au_2 and parts of wafer of approximately 10x10-mm^2 size were mounted onto a copper heatsink. Then, the InP substrate was selectively removed and an n-contact to the top DBR with a window on top of each regrown TJ was formed. The chips were separated by selective chemical etching.

3. Device performance

The gain mirror assembly was aligned with a highly reflective spherical (radius of curvature of 50mm) dielectric mirror, to form a stable planar-concave Fabry-Perot external cavity, as described in [4]. The selected cavity length of about 49 mm allows for the largest variation of cavity mode size on chip. The EP-VECSELs devices were tested with different output couplers (OCs) with transmission values of 10% and 3% under CW operation.

The CW light-current-voltage characteristics (LIVs) measured with a 3% and 10% OC at 15ºC for a device with 20-µm TJ aperture are depicted in Figure 2a. The threshold current values are less than 7- and 9-mA, measured with 3 and 10% OC scheme, respectively. The maximum emission power of approximately 7-mW was reached for the configuration with 3% OC at approximately 60-mA pumping current, while for the 10% OC scheme the maximum power was only ~5-mW. Such a behavior was observed for all measured chips; i.e., by using OC with higher transmission coefficient both the emission power and threshold current degrade, indicating that optimal measuring configuration has not been reached yet. On Figure 2b the CW light-current (LI) characteristics of two devices with TJ apertures of 40 and 50-µm and 3% OC are shown. The maximum power of ~20-mW was reached with the 50-µm TJ device at 15ºC and at 180 mA driving current, while the 40-µm VECSEL showed ~15-mW of emission power. The measured spectra (not shown here) show that lasing wavelength is in the ~1555-1565-nm range on devices from different places on wafer and the emission occurs in multimode regime.

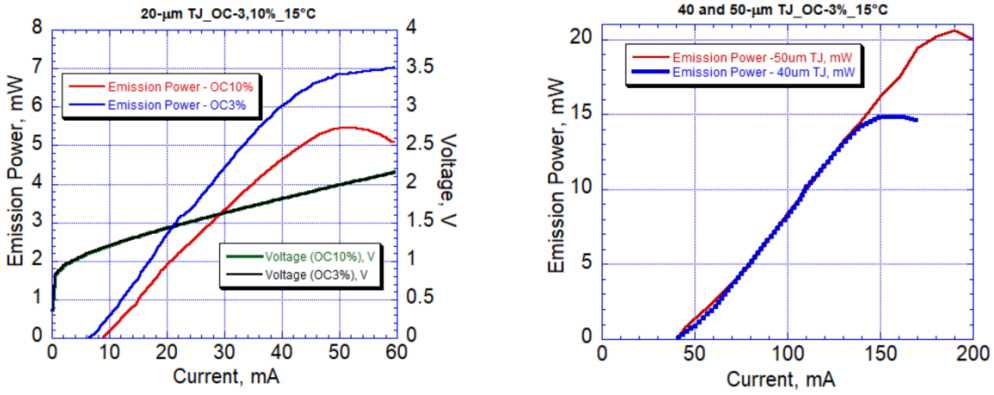

a) b)

Figure 2. The CW LIVs for a device with 20-µm TJ aperture, 3 and 10% output couplers (a); and LI characteristics for 2 different VECSELs with 40 and 50-µm TJ apertures and with 3% OC.

4. Conclusions

We report on the design, fabrication and characterization of EP-VECSELs emitting at 1550-nm wavelength range. We demonstrate up to 20-mW of CW output power from devices with 50-µm aperture at 15°C, which represents to our knowledge the highest power value reported so far for EP-VECSELs in the 15XX-nm wavelength band, but significantly lower compared with 1-µm wavelength EP-VECSELs (~0.5-1W), grown on GaAs substrates. Further improvements in the device performance are expected through the optimization of the pumping scheme and device design.

5. References

[1] T.Leinonen et al., "33 W continuous output power semiconductor disk laser emitting at 1275 nm", Optics Express, v.25, No.6, pp.7008-7013, 2017.
[2] J. Lyytikäinen et al., IEEE Phot.Tech. Lett., "High-Power 1.48 µm Wafer-Fused Optically Pumped Semiconductor Disk Laser", v.23, No.13, pp.917-919, 2011.
[3] A. Bousseksou et al. "Fabrication and characterization of 1.55 μm single transverse mode large diameter electrically pumped VECSEL," Opt.Quantum Electron., vol. 38, pp. 1269–1278, 2006.
[4] A.Caliman et al. "14XX nm-wavelength electrically-pumped VECSELs fabricated by wafer fusion", Optics Express, vol.21, No.11, pp.13668-13675, 213.
[5] A. Sirbu et al. "Wafer-fused heterostructures: application to vertical cavity surface-emitting lasers emitting in the 1310 nm band," Semicond. Sci. Technol., vol.26, No.1, pp. 014016-014022, 2011.

Acknowledgements

This work was supported by ANR-FNS IDYLIC Project.

Nanoscale devices for Optical Integration

D. Huffaker

Ser Cymru Chair, Advanced Materials and Devices, Cardiff University, Wales CF24 3AA
Professor, California Nano-Systems Institute, UCLA, Los Angeles, California 90095, US
HuffakerDL@cardiff.ac.uk

Nanostructure remain an attractive approach to integration of III-V semiconductor materials on silicon or silicon-on-insulator (SOI) substrates especially to realize low-consumption, small-footprint and high speed photonic devices. Due to the mismatches in lattice constants and thermal expansion coefficient between III-V materials and silicon, thick metamorphic buffer layers are typically employed to confine threading dislocations in the buffer layers and achieve good material quality. Alternatively, wafer bonding techniques are also widely used to integrate active media on silicon platforms.

Here, we provide a global overview of monolithic integration of III-V semiconductor nanowires on SOI platforms by catalyst-free selective-area epitaxy (SAE) using MOCVD. We will also focus on our own enabling technology for monolithic nano-LEDs, nanolasers and nanophotodetectors compatible with silicon photonic platforms, since the nanoscale footprint enables the defect-free growth on lattice-mismatched substrates without the need of Au catalysts that contaminate silicon. Here we discuss full details of the InGaAs nanowires from seeding through heterostructure, doping and passivation which yield 100 % vertical growth and excellent uniform dimensions. Advancing from nanowire growth on planar SOI layers, the growth of nanowire arrays on 3D structured SOI substrates with 1D/2D gratings, waveguides, and couplers are also demonstrated, which represents a way toward practical nanowire-based optical links.

1.55 µm Quantum Dot Lasers and Amplifiers with High Temperature Stability

Johann Peter Reithmaier[1], Gadi Eisenstein[2]

[1]Technische Physik, Institute of Nanostructure Technologies and Analytics (INA), CINSaT, University of Kassel 34132, Germany
[2]Departm. of Electrical Engineering and Russell Berrie Nanotechnology Institute (RBNI), Technion – Israel Institute of Technology, Haifa, Israel

The major performance data of optoelectronic devices show usually a strong temperature dependence due to carrier redistribution from ground to excited states. This is even more severe in smaller bandgap materials such as InP based compounds addressing telecom emission wavelengths at 1.55 µm.

With atomic-like gain material, such as quantum dot (QD) material, one can expect strong improvements due to delta-like density of states distribution. In an ideal case of large enough energy splitting between ground and exited states the carrier distribution stays the same independent of the operation temperature resulting in constant performance of lasers, i.e. temperature independent threshold conditions, differential efficiency and modulation properties.

The talk will give an overview about the most recent progress in the development of InP-based QD gain material for directly modulated laser diodes, semiconductor optical amplifiers (SOA) and widely tunable narrow linewidth lasers for coherent communication.

A major breakthrough in QD material was the significant reduction of the inhomogeneous linewidth broadening to 17 meV (low-T photoluminescence) for a single QD layer caused by a reduced dot size distribution [1]. Based on this new generation of QD material temperature stable lasers with high characteristic temperatures (T_0 = 140 K, T_1 > 900 K) for threshold and differential efficiency, respectively, could be obtained [2]. Due to a high optical gain of up to 100 cm^{-1}, short cavity lasers with a length of 230 µm could be modulated up to 35 GBit/s [3]. Based on the same QD gain material, semiconductor optical amplifiers were fabricated showing similar high temperature performance, which allow a temperature independent operation between 20 and 100 °C without significant deterioration [4].

For coherent communication, narrow linewidth lasers are needed as reference for signal detection. QD laser material exhibits a symmetric gain function resulting in rather low linewidth enhancement factors (< 1) in comparison to quantum well lasers (typically > 3-4). Due to this low linewidth enhancement factor the laser linewidth in distributed feedback (DFB) QD lasers could be reduced by about one order of magnitude to a record value of 110 kHz. Results of a widely-tunable (46 nm) narrow-linewidth light source based on a DFB laser array with an integrated SOA will be also presented [5].

The authors would like to thank the financial support via the EU project SEQUOIA, the BMBF-project MONOLOP and the Israel Science Foundation.

[1] S. Banyoudeh, J. P. Reithmaier, “High-density 1.54 µm InAs/ InGaAlAs/InP(100) based quantum dots with reduced size inhomogeneity,” J. Cryst. Growth **425**, 299-301 (2015).

[2] A. Abdollahinia, S. Banyoudeh, A. Rippien, F. Schnabel, O. Eyal, I. Cestier, I. Kalifa, E. Mentowich, G. Eisenstein, J.P. Reithmaier, "Temperature Stability of Static and Dynamic Properties of 1.55 µm Quantum Dot Lasers", Optics Express 26, 6056 (2018).

[3] S. Banyoudeh, A. Abdollahinia, V. Sichkovskyi, O. Eyal, G. Eisenstein, J.P. Reithmaier, "Temperature-Insensitive High-Speed Directly Modulated 1.5 µm Quantum Dot Laser", IEEE Photon. Technol. Lett. **28**, 2451 (2016).

[4] O. Eyal, A. Willinger, S. Banyoudeh, F. Schnabel, V. Sichkovskyi, V. Mikhelashvili, J.P. Reithmaier, and G. Eisenstein, "Static and dynamic characteristics of an InAs/InP quantum-dot optical amplifier operating at high temperatures", Optics Express 25, 27262 (2017).

[5] A. Becker, V. Sichkovskyi, M. Bjelica, A. Rippien, F. Schnabel, M. Kaiser, O. Eyal , B. Witzigmann, G. Eisenstein, and J.P. Reithmaier, "Widely Tunable Narrow-Linewidth 1.5 µm Light Source Based on a Monolithically Integrated Quantum Dot Laser Array", Appl. Phys. Lett. 110, 181103 (2017).

Energy-efficient VCSELs for 200+ Gb/s optical interconnects

Gunter Larisch[1]*, Ricardo Rosales[2], James A. Lott[2], and Dieter Bimberg[1,2]

1 Bimberg Chinese-German Center of Green Photonics
Changchun Institute of Optics, Fine Mechanics, and Physics (CIOMP), Chinese Academy of Sciences (CAS)
3888, Dongnanhu Road, Changchun 13033 People's Republic of China
** larisch@ciomp.ac.cn*
2 Center of Nanophotonics, Institute of Solid State Physics, Technische Universität Berlin,
Berlin D-10632, Federal Republic of Germany

Summary: Vertical-cavity surface-emitting lasers (VCSELs) for 200+ Gbit/s single fiber data transmission systems with an energy to data ratio (EDR) of only 320 fJ/bit are presented. Tuning the cavity photon lifetime is demonstrated to lead to an increase of the data rate in concert with a reduction of the EDR. Error-free back-to-back data transmission at 50+ Gbit/s for 980 nm VCSELs is presented first. Our VCSELs emitting at 850 nm, 880 nm, 910 nm, and 940 nm, the present IEEE 802.3 coarse wavelength multiplexing standard, across OM5 multimode fiber thus enable 200+ Gbit/s error-free transmission.

1. Introduction

The energy required to transmit information as encoded optical and electrical data bits within and between electronic and photonic integrated circuits, within and between computer servers, within and between data centers, and ultimately across the earth from any one point to another clearly must be minimized. This energy spans from typically tens of picojoules-per-bit to well over tens of millijoules-per-bit for the intercontinental distances. We seek to meet the exploding demand for information within the terrestrial resources available, but more importantly as a common-sense measure to reduce costs and to become stewards of a perpetual Green Internet. The concept of a Green Internet implies a collection of highly energy-efficient, independent, and ubiquitous information systems operating with minimal impact on the environment via natural or sustainable energy sources. A key enabling optical component for the Green Internet is the vertical-cavity surface-emitting laser (VCSEL). We present our research on energy-efficient VCSELs, being sources for optical interconnects and optical fiber data communication, operating at bit rates exceeding 50 Gbps with energy efficiencies approaching 100 fJ per-bit.

2. Link performance and laser physics

The most important application of the lasers presented here is large data transmission bit rate across optical fibers. The most important parameters defining their performance are the maximum error-free bit rate *BR* ($BR = \text{number of transmitted bits/time}$**)** and the energy to data ratio *EDR* ($EDR = V \cdot A/BR$), with *V* bias voltage and *A* bias current [1].

We use standard single mode rate equations to describe the laser diode physics. Their solution yields the transfer function ($H(f) = \frac{f_R^2}{f_R^2 - f^2 + j\left(\frac{f}{2\pi}\right)\gamma} \cdot \frac{1}{1 + j\left(\frac{f}{f_p}\right)}$, with the relaxation resonance frequency (f_R), damping (γ), and parasitic cut off frequency (f_p) [2]. The value of *H(f)* decreases with increasing frequency (*f*). The frequency where *H(f)* is reduced by 3 dB defines the bandwidth f_{3dB}. According the Shannon-Hartley Theorem laser performance and laser physics are connected by the spectral efficiency *M*, where ($BR = M \cdot f_{3dB}$) [3].

To increase f_{3dB}, the bandwidth needs to be increased. Using highly strained multiple quantum wells in the active region increases the gain. Reducing the cavity length to $\lambda/2$ and shrinking the aperture diameter reduces the active volume [4]. We furthermore tune the cavity photon lifetime by adding a thin layer of SiN to the top mirror surface. An error-free data transmission rate of 52 Gbit/s for NRZ measurements, presently limited by our test equipment, is observed for all of our lasers [5]. Tuning the photon lifetime decreases our VCSEL's energy consumption at 50 Gbit/s by about 25%. The parameters of optical data transmission depend equally on the properties of the passive fiber and the receiver. Receivers that are more sensitive enable larger distances and/or lower energy consumption per bit. Larger receiver cut-off frequencies enable additionally larger data rates. Presently the IEEE802.3 standard asks for lasers emitting at the four wavelengths of 850 nm, 880 nm, 910 nm, and 940 nm, enabling a quadrupling of the data rate across the same optical fiber by using lasers with similar properties. We use here the novel wideband OM5 multimode fiber (MMF) to ensure *M*(*f*,*P*) is independent of the emission wavelength.

Our VCSELs are grown by MOVPE on 0-degree off {001}-oriented GaAs substrates and emit at 850, 880, 910, 940, and additionally at 980 nm at room temperature (RT). We use AlGaAs distributed Bragg reflector (DBR) mirrors with compositionally-graded interfaces. The quantum well active region consists of five compressively-

strained InGaAs quantum wells surrounded by either strain-compensating GaAsP barrier layers or by unstrained AlGaAs barrier layers (depending on the desired emission wavelength), all in half-lambda-thick optical cavities.

3. Measurement results

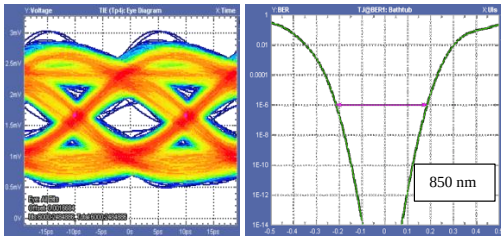

Figure 1: The eye diagram (left) and bit error ratio (right) for a back-to-back data rate of 50 Gbit/s of an ~3 µm oxide aperture diameter VCSEL emitting at 850 nm, which is representative of all our devices.

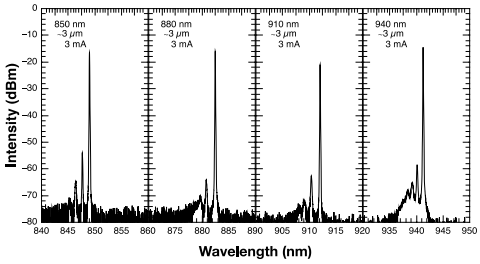

Figure 2: Emission spectra of four VCSELs emitting at 850, 880, 910, and 940 nm with oxide aperture diameters of ~3 µm biased at 3 mA. All VCSELs show a SMSR > 30 dB and are thus single mode.

Figure 1 shows the result of a non-return to zero (NRZ) data transmission experiment across a 2 m OM5 MMF that has been used for all the experiments. Fig. 1 has been taken with a Tektronix 70 GHz real time oscilloscope and a 33 GHz optical probe. Since the lasers at all wavelengths show very similar bandwidths and output power also the data transmission results are the same. This eye diagram and BER of an 850 nm laser is representative for all wavelengths. By multiplexing our four wavelengths, a transmission rate of 200+ Gbit/s can be achieved.

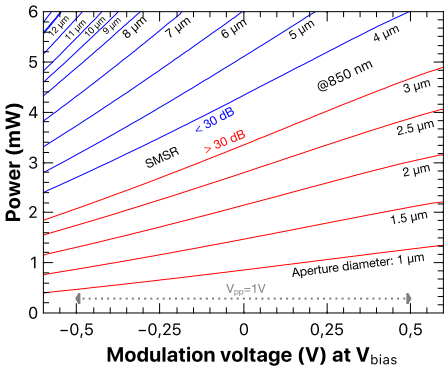

Figure 3: Output power versus modulation voltage at a bias V_{bias} in the middle of the linear L-V regime.

All lasers at all wavelengths have a very large slope efficiency of 1 W/A with a very linear LI-curve. So even small aperture diameter lasers with single mode emission shown in Figure 2 have a large optical output power of nearly 3 mW. Fig. 3 shows the optical output power versus the modulation voltage for our complete variety of oxide aperture diameters for a bias V_{bias} in the middle of the linear L-V regime. These lasers are thus well suited for long distance fiber transmission and higher order modulation formats like PAM 4. The photon lifetime tuning employed for the 980 nm lasers might enable still large bandwidths and larger optical power.

4. Conclusion

200+ Gbit/s data transmission via multiplexing 850, 880, 910, 940 nm single mode emitting VCSELS is presented. The linearity of the L-I-characteristics will easily allow larger data rates e.g. via PAM 4. The EDR is as low as 320 fJ/bit, thus well suited for long distance fiber transmission.

5. Acknowledgements

This work was supported by Dr. Wu Bo of Huawei Technologies Co., Ltd. The authors acknowledge Felix Lenze, John Marinnan, and Ahed Abedrabuh of Tektronix GmbH, Germany for providing high frequency measurement equipment.

6. References

[1] P. Moser *et al.*, "81 fJ/bit energy-to-data ratio of 850 nm vertical-cavity surface-emitting lasers for optical interconnects," *Applied Physics Letters*, vol. 98, no. 23, pp. 231106-1–3, 2011.

[2] L. A. Coldren and S. W. Corzine, *Diode lasers and photonic integrated circuits*, (Wiley series in microwave & optical engineering). New York, NY, USA: John Wiley & Sons, 1995, pp. xxiii, 594.

[3] C. E. Shannon, "Communication in the presence of noise," *Proceedings of the IRE*, vol. 37, no. 1, pp. 10-21, 1949.

[4] P. Wolf, P. Moser, G. Larisch, W. Hofmann, and D. Bimberg, "High-speed and temperature-stable oxide-confined 980-nm VCSELs for optical interconnects," *IEEE Journal of Selected Topics in Quantum Electronics*, vol. 19, no. 4, pp. 1–7, 2013.

[5] G. Larisch, P. Moser, J. A. Lott, and D. Bimberg, "Large bandwidth, small current density, and temperature stable 980-nm VCSELs," *IEEE Journal of Quantum Electronics*, vol. 53, no. 6, pp. 1-8, 2017.

Heterogeneous multi-wavelength quantum-dot light sources on silicon

Di Liang[1]*, Geza Kurczveil[1], Chong Zhang[1], Antoine Descos[1], Yingtao Hu[1], Marco Fiorentino[1], and Raymond Beausoleil[1]

1 Hewlett Packard Labs, 1501 Page Mill Road, Palo Alto, California, USA
**di.liang@hpe.com*

Summary: Wavelength division multiplexing (WDM) is a major technology innovation landmark to enable successful commerical deployment of the long-haul optical communicaiton systems. Rapid increasing bandwidth demand in datacom applications

1 Introduction

Increasing demands for data bandwidth and photonic link cost in data centers and high-performance computing (HPC) are primary driving forces to develop integrated photonics on silicon. Several emerging applications like AI, Lidar, 5G wireless, IoT, sensing and many more will be immediate beneficiaries for such a highly integrated, low-cost photonic platform as soon as standardized volume manufacturability is realized. Aggregated bandwidth per fiber can be boosted by increasing the data rate per wavelength or adding more channels, eventually migrating to dense wavelength division multiplexing (DWDM)

Robust operation in a temperature fluctuating environment has been a major technical challenge for light sources, particularly the integrated ones on silicon-on-insulator (SOI) substrate. Thus 1qantum-dot (QD) materials regained much interest recently to improve laser performance robustness at elevated temperature for its 3D carrier confinement. Other superior material properties, e.g., immunity to material defects, wider optical gain bandwidth, lower noise and better tolerance to external optical feedback, also favor material integration and laser device operation.

2. Heterogeneous WDM QD light sources

In this talk, we will review our recent progress to develop two types of on-chip lasers around 1.31 μm InAs QD materials on a heterogeneous platofrm. Comb lasers and single-wavelength microring lasers (array) are designed for different application scenarios in HPC. We recently demonstrated the first QD comb laser with seamless optical coupling to on-chip Si waveguide circuits [1]. They also showed up to 100 ^{o}C cw operation with minimal lasing efficiency degradation. 15 low-noise channels (left figure below) with 100 GHz channel spacing are mesaured on a fully integrated version. 13 of them have power varation within 3 dB and 14 of them show error-free ($<10^{-12}$) operation at 10 Gb/s (limited by the measurement tool) external modulation [2, 3]. With further improvement in design and fabrication, 40 or more channels are expected from one comb laser. Convenient integration with an array of external high-speed modulators will deliver Tb/s-level data communications among major data ports in HPC.

Fabricated compact microring lasers with 50 μm diameter operate at very low threhsold around 1-3 mA with 1 mW maximum output power, and cw lasing up to 70 ^{o}C stage temperature [4]. While much larger optical gain bandwidth can support multiple main lasing wavelength with similiar power level, i.e., very small side-mode surpression ratio (SMSR), single-wavelength can be achieved at certain bias as shown in the right figure below. They have been directly modulated up to 15 Gb/s, a record for silicon-based O-band QD lasers to our best knowledge. Low-noise, open eye digrams after transmission through 4.2 km single-mode fiber at room-temperature and back-to-back transmsion at 50 ^{o}C, both at 12.5 Gb/s, are shown as well. Further improvement is expected with smaller device dimension and higher optical confinement, or employment of a novel metal-oxide semiconductor (MOS) capacitor for photon lifetime modulation [5]. An array of such lasers with slightly different dimension along just one bus waveguide can conveninently form a compact multi-wavelength tranmistter to provide tens to several hundreds Gb/s data transmission between nodes in a server rack within a high performance computer (HPC) or data center.

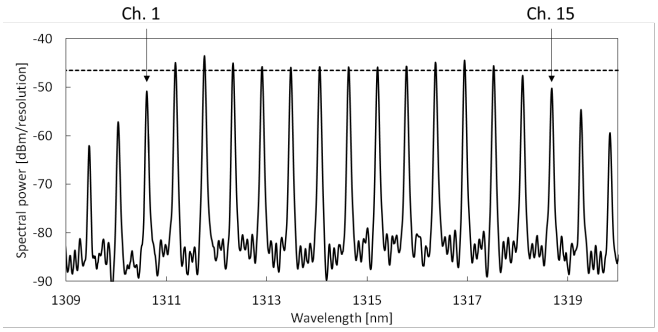

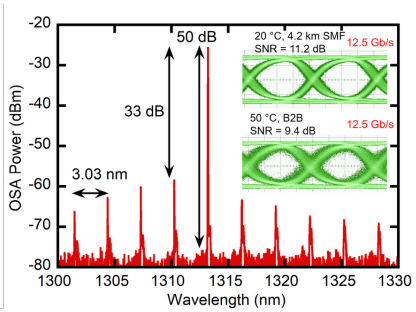

3. References

[1] G. Kurczveil et al., "Robust hybrid quantum dot laser for integrated silicon photonics," *Optics Express,* vol. 24, pp. 16167-16174, 2016.
[2] G. Kurczveil et al., "Error-free operation in a hybrid-silicon quantum dot comb laser," *Photonics Technology Letters,* vol. 30, pp. 71-74, 2018.
[3] G. Kurczveil et al.,"On-chip Hybrid Silicon Quantum Dot Comb Laser With 14 Error-Free Channels," in *ISLC* Santa Fe, NM, USA, 2018.
[4] C. Zhang et al.,"High Speed QDs Microring Lasers on Silicon," in *ECIO* Valencia, Spain, 2018.
[5] D. Liang et al.,"A Fully-integrated Multi-λ Hybrid DML Transmitter," in *OFC* San Diego, CA, USA, 2018, p. Th3B.5.

Photonic engineering of high performance quantum cascade lasers at Terahertz frequencies

M. Vitiello

NEST, CNR – Istituto Nanoscienze and Scuola Normale Superiore, Italy

Terahertz (THz) technology has prompted in the last decade a major surge of interdisciplinary researches, inspiring fundamental insights and amazing applications in microscopic and macroscopic systems. Being a transition region between electronics and photonics, between component sizes that are smaller and larger than the radiation wavelength, the THz frequency "gap" offers unusual possibilities in borrowing concepts and technologies from fundamentally different worlds.

Recent technological innovation in photonics and nanotechnology is now enabling Terahertz frequency research to be applied in an increasingly widespread range of applications. In this perspective, the availability of compact THz devices that are convenient single frequency, high-power, low divergent and narrow linewidth laser sources, is matching increasing demand for spectroscopic applications encompassing environmental monitoring, security and biomedical sensing, as well as more fundamental molecular studies and frequency metrology.

Quantum cascade lasers (QCLs) operating at terahertz (THz) frequencies have undergone rapid development since their first demonstration. These laser sources can now be designed with high power, broad tunability, high spectral purity, and ultra-broadband gain, leading to a breadth of potential applications ranging from astronomy, security screening, biomedicine, cultural heritage. Typically, continuous-wave (CW) operation is required in THz QCLs, in combination with a low divergent spatial profile in the far-field and a fine spectral control of the emitted radiation.

The talk will provide an overview of our recent technological developments of QCLs emitting at THz frequencies, from the engineering of broadband high-power, low divergent 1D and 2D continuous wave QC resonators, to broadly tunable geometries and modulation architectures.

References

1. S. Biasco et al. Nature Communications 9, 1122 (2018)
2. L. Li et al., Electronics Letters doi:10.1049/el.2018.6062, (2018).
3. L. Consolino et al. Science Advances 3, e1603317, (2017).
4. L. Masini et al. Light Science and Applications, 3, e1603317 (2017)
5. S. Biasco et al. Photonics 3, 32, (2016).
6. F. Castellano et al. Scientific Reports 6, 23053 (2016).
7. F. Castellano et al. Appl. Phys. Lett.107, 261108 (2015).
8. F. Castellano et al., Appl. Phys. Lett. 106, 011103 (2015).
9. F. Castellano et al. Optics Express 23, 5190 (2015).
10. A. Campa et al. Optics Express 23, 3751 (2015).
11. M.S. Vitiello et al. Nature Communications 5, 5884 (2014).
12. M.S. Vitiello et al. Nature Photonics 6, 525 (2012).

Recent advancements in QCL-based quartz-enhanced photoacoustic spectroscopy for gas sensing applications

P. Patimisco[1,2], A. Sampaolo[1,2], M. Giglio[1], V. Mackoviak[3], H. Rossmadl[3], A. Cable[4], F.K. Tittel[2] and V. Spagnolo[1,2]*

1 PolySense Lab-Dipartimento Interateneo di Fisica, University and Politecnico of Bari, Via Amendola 173, Bari, Italy
2 Department of Electrical and Computer Engineering, Rice University, 6100 Main Street, Houston, TX 77005, USA
3 Thorlabs GmbH, Hans-Boeckler Straße 6, 85221 Dachau, Germany
4 Thorlabs, Inc., 56 Sparta Ave., Newton, 07860, USA
** vincenzoluigi.spagnolo@poliba.it*

Summary: Here we review the latest advances in quartz-enhanced photoacoustic spectroscopy (QEPAS) based trace-gas sensing. Starting from QEPAS basic physical principles, a detailed theoretical analysis and experimental study regarding the influence of quartz tuning forks (QTFs) geometry on QEPAS performance will be provided. Guidelines for design QTFs optimized for QEPAS operation will be described and results obtained by exploiting novel micro-resonator configurations for sound amplification, capable of increasing the QEPAS signal-to-noise ratio by more than two orders of magnitude will be presented. Finally, results achieved using custom QTFs with novel detection module configurations will be described, including the realization of a QEPAS sensor capable to detect methane, ethane and propane with record sensitivities.

1 Introduction

Trace gas detection has long played an important role in developing and improving the technology and the solutions employed for gas sensing techniques. Optical sensors can offer higher sensitivity, selectivity and long-term stability with respect to other methods, with advantages, such as a much longer lifetime and shorter response time, which enables real-time and in-situ detection. Photoacoustic spectroscopy is one of the most sensitive optical detection schemes. It is based on the detection of acoustic waves, which result from the absorption of light in a specific targeted gas. Light absorbed excites a fraction of the ground-state molecular population into higher energy levels. These excited states subsequently relax through a combination of radiative and non-radiative pathways. The nonradiative component ultimately generates heat in the localized region of the excitation light beam and a pressure wave propagates from the source, which is then detected by a microphone. The targeted gas is enclosed inside a resonant acoustic cell. The quality factor Q and the resonance frequency f typically fall in the ranges of 40–200 and 1–4 kHz, respectively. Photoacoustic detection is unique since it is a direct monitor of the nonradiative relaxation channel and, hence, complements absorption spectroscopic techniques [1]. Furthermore, PAS does not require an optical detector and is wavelength independent. Other advantages include small size, large linear dynamic range (from few % to part-per-trillion concentration range) and long-term stability. These advantages make the PAS technology competitive with, and in many cases, preferred to, other trace gas sensing methods. A significant improvement of the PAS technique was made by replacing the microphone with a high-Q piezoelectric quartz tuning fork (QTF) acting as a sharply resonant acoustic transducer to detect weak photoacoustic excitation and allowing the use of extremely small volumes [2,3]. This variant of PAS is named as quartz-enhanced photoacoustic spectroscopy (QEPAS). Such an approach removes restrictions imposed on the gas cell by the acoustic resonance conditions. QEPAS measurements are usually performed using a standard QTF operating at a detection frequency of about 32 kHz and are more sensitive to the gas vibrational-translational relaxation rate compared to the conventional PAS, which is commonly performed at $f < 4$ kHz. In addition, the small prongs spacing (300 μm) of the standard QTF prevents the implementation of laser source with poor laser beam quality like fiber amplified near-IR diode laser or THZ QCLs sources. The successful realization of QTFs having lower resonance frequencies and larger prongs spacing, keeping high the resonance Q-factor, opened the way to advances of QEPAS technique, like the implementation of new acoustic micro-resonator (AmR) system capable to enhance the signal-to-noise factor of more than two orders of magnitude and the exploitation of the first overtone flexural mode for gas sensing leading to the first demonstration of simultaneous dual-gas sensing with QEPAS technique [4-7]. Recent advances of the QEPAS sensing, achieved using custom QTFs and novel AmR systems will be discussed, including the realization of a QEPAS sensor for petrochemical applications, capable to detect methane, ethane and propane with record detection limits.

2. Quartz-enhanced photoacoustic sensing setup

A schematic of a typical QEPAS setup, as used in most reported QEPAS sensor systems, is shown in Fig. 1. A laser source, typically a diode laser, a quantum cascade laser (QCL) or an interband cascade laser (ICL) serves

as excitation source for generating the QEPAS signal. The QTF acoustically coupled with a pair of microresonator tubes (named as acoustic detection module, ADM) is mounted inside a vacuum-tight cell equipped with optical windows. The laser beam is focused by a lens between the QTF prongs and it passes through the ADM. A power meter is used for monitoring the laser power as well as for optical alignment. A function generator is used to sinusoidally dither the laser current at a half of QTF resonance frequency and a lock-in amplifier to demodulate the signal at the resonance frequency (wavelength modulation and *2f*-detection).

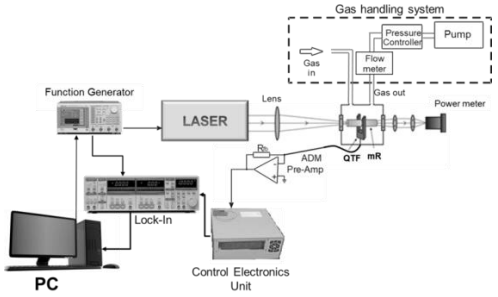

Fig. 1. Schematic of a typical QEPAS sensor setup. QTF, quartz tuning fork; mR, acoustic micro-resonator; ADM, acoustic detection module; PC, personal computer.

The flow rate and pressure of the sample gas passing through the ADM can be controlled and maintained by using a flow meter and pressure controller, respectively. A control electronics unit (CEU) is used to determine the main QTF parameters: dynamic resistance *R*, *Q*, and *f*.

3. Results

In terms of new results achieved with custom-made QTFs, a set of QTFs optimized for QEPAS have been designed, realized and tested. Starting from a QTF geometry designed to provide a fundamental flexural in-plane vibrational mode resonance frequency of ~ 16 kHz, with a quality factor of 15,000 at atmospheric pressure, two novel geometries have been realized: a QTF with T-shaped prongs and a QTF with prongs having rectangular grooves carved on both surface sides. The QTF with grooves showed the lowest electrical resistance, while the T-shaped prongs QTF provided the best photoacoustic response in terms of signal-to-noise ratio (SNR). When acoustically coupled with a pair of micro-resonator tubes, the T-shaped QTF provides a SNR enhancement of a factor of 60 with respect to the bare QTF, which represents a record value for mid-infrared QEPAS sensing.

A QEPAS sensor for hydrocarbon detection in gas phase, which represents a powerful tool to guide oil exploration and production operations for the oil & gas industry, have been realized and tested in laboratory environment. QEPAS technique fit requirements for such applications, which ask for high sensitivity, selectivity, robustness and compactness. A QEPAS sensor system has been designed to detect methane (CH_4), ethane (C_2H_6) and propane (C_3H_8) by using a single ICL emitting in the spectral range 3.342-3.349 µm. The QEPAS sensor achieved an ultimate detection limit of 90 ppb, 7 ppb and 3 ppm for CH_4, C_2H_6 and C_3H_8, respectively, for a 1 s integration time. The detection limit achieved for ethane represents a record value for the QEPAS technique. Propane has a broadband absorption spectrum and the capability of QEPAS to detect heavy molecules has been demonstrated in few ppm range. Measurements at both low and atmospheric pressures have been carried out for mixtures simulating typical downhole hydrocarbon concentrations.

4. Conclusions

In conclusion, several novel approaches of QEPAS based trace gas sensors have been demonstrated. The high sensitivity and selectivity, combined with small size, robustness and low cost makes QEPAS sensors mature for real-world applications.

5. References

[1] A. Elia et al., "Photoacoustic Techniques for Trace Gas Sensing Based on Semiconductor Laser," Sensors 9, 9616–9628, 2009.
[2] P. Patimisco, et al., "Quartz–enhanced photoacoustic spectrophones exploiting custom tuning forks: a review," Adv. Phys. X 2, 169, 2016.
[3] P. Patimisco, et al., "Recent advances in quartz enhanced photoacoustic sensing," Appl. Phys. Rev. 5, 011106, 2018.
[4] P. Patimisco, et al., "Analysis of the electro-elastic properties of custom quartz tuning forks for optoacoustic gas sensing", Sens. Act. B-Chem. 227, 539-546, 2016.
[4] A. Sampaolo, et al., "Improved Tuning Fork for Terahertz Quartz-Enhanced Photoacoustic Spectroscopy," Sensors, 16, 439, 2016.
[5] H. Zheng, et al., "Double antinode excited quartz-enhanced photoacoustic spectrophone," Appl. Phys. Lett. 110, 021110, 2017.
[6] H. Wu, et al., "Simultaneous dual-gas QEPAS detection based on a fundamental and overtone combined vibration of quartz tuning fork," Appl. Phys. Lett. 110, 121104, 2017.

Entrainment phenomenon in a mid-infrared QCL with external optical feedback and low frequency modulation

O. Spitz,[1,2,3,+] J. Wu,[3,4] M. Carras,[2] C. W. Wong,[3] F. Grillot[1,3,5]
[1]*LTCI Télécom ParisTech, Université Paris-Saclay, 46 rue Barrault, Paris, 75013, France*
[2]*mirSense, Centre d'intégration NanoInnov, 8 avenue de la Vauve, Palaiseau, France*
[3]*Fang Lu Mesoscopic Optics & Quantum Electronics Laboratory, UCLA, CA 90095, USA*
[4]*College of Electronic & Information engineering, Southwest University, Chongqing, China*
[5]*Center for High Technology Materials, University of New-Mexico, NM 87106, USA*

Summary: This experimental work reports on mid-infrared quantum cascade lasers operating under external optical feedback and external periodic bias forcing. A way of controlling spikes occuring in a deterministic chaotic pattern is experimentally described. These findings are of paramount importance for future optical countermeasure systems and secure atmospheric transmission lines as well as for reproducing neuronal systems and the communication between neurons due to sudden bursts.

1. Introduction

Quantum cascade lasers (QCLs), firstly experimentally demonstrated in 1994 [1], are optical sources exploiting radiative intersubband transitions within the conduction band of semiconductor heterostructures. The wide range of wavelengths achievable with QCLs, from mid-infrared to terahertz range, leads to a large number of applications including absorption spectroscopy, optical countermeasures and free space communications [2]. When applying optical feedback with an increasing strength, the QCL dynamics was found to bifurcate to periodic dynamics at the external cavity frequency and later to chaos [3]. Prior work proved that the dynamics of a laser diode operating with time-delayed optical feedback and periodic forcing show an arrangement of the power dropouts in the laser output [4,5]. These power dropouts result from low frequency fluctuations (LFFs) hence a manifestation of deterministic chaos [3]. In this paper, we unveil the first study of this kind for a QCL and we propose a way of controlling these irregular dropouts by using an external sine forcing at low frequency.

2. Experimental setup

The QCL under study is a distributed feedback (DFB) laser. The light intensity voltage (LIV) characteristics of the free-running QCL under study are depicted on Fig. 2 a) while Fig. 2 b) shows the optical spectrum retrieved with a Fourier transform infrared spectrometer (FTIR). The optical spectrum is perfectly single mode and the DFB peak is at 5.63 microns. The experimental setup is similar to that presented in [6] at 77K. It is made of an analysis path with a high bandwidth Mercury-Cadmium-Telluride (MCT) detector which is linked to an oscilloscope at 1 giga sample per second for real time acquirements and a RF spectrum analyzer to carry out accurate frequency measurements on the optical signal. The external optical feedback path is set with a gold plated mirror at 27 cm from the front facet of the QCL and a polarizer, which scales the amount of back-reflected light since the QCL wave is TM polarized. The current source in this experiment is a low noise source (Wavelength Electronics QCL2000 LAB) and the DC bias delivered by the source can be sine modulated up to 3 MHz with an external signal from a waveform generator (Rigol DG1022Z).

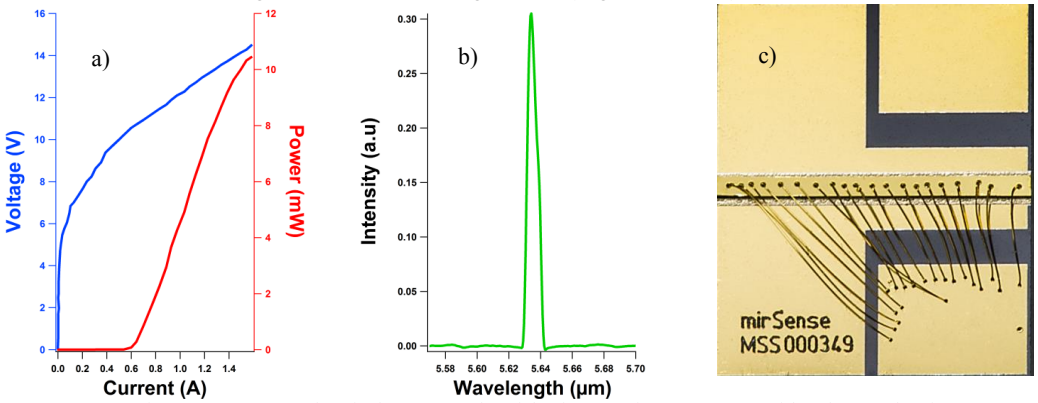

Figure 1: LIV (a) and optical spectrum (b) of the free running DFB QCL with a duty cycle of 3 % at 290K and close-up of the QCL under study (c)

3. Results and discussion

The behavior of the QCL under external optical feedback and sine forcing is studied through the analysis of the q : p parameter [4] where q represents the number of dropouts occurring in the time-series every p periods of the forcing. In our case, the number of dropouts is at least one per period, as can been seen on Fig 2. Therefore, p is fixed to 1. Increasing the modulation frequency from 2 MHz to 2.7 MHz makes the q value decrease from 5 to 2, emphasizing the key influence of the forcing frequency on the entrainment of the spikes which always appear for a fixed phase of the periodic forcing. Another parameter of prime importance in the occurrence of these LFF spikes is the amplitude of the sine forcing. Fig 3. shows that the q value is strongly increased when increasing the AC amplitude from 40 mA to 160 mA, the frequency of the sine forcing remaining constant at 2 MHz. This phenomenon occurs for various continuous biases applied to the QCL, the three of them being above the threshold of the solitary laser (331 mA at 77K). Furthermore, it is relevant to notice that changing the DC bias does not really affect the q value, whatever the value of the AC amplitude (Fig 3.).

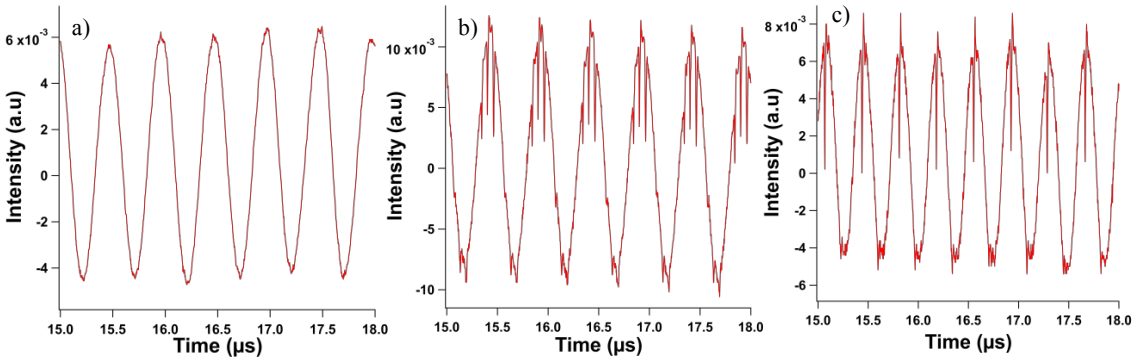

Figure 2: Experimental time traces when external optical feedback is applied to the QCL and with a sine periodic forcing of the bias DC current of : 2 MHz (b), 2.7 MHz (c); trace (a) corresponds to the case when no external optical feedback is applied and the modulation frequency is 2 MHz. All the traces were retrieved for a DC bias of 350 mA and AC amplitude of 120 mA, which is added to the DC bias.

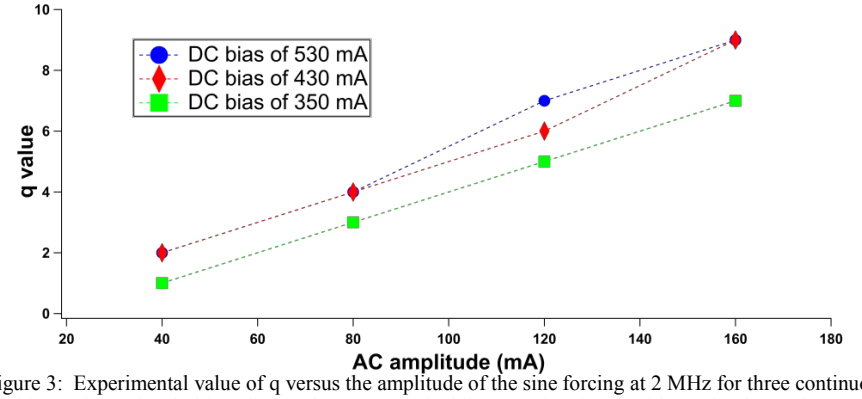

Figure 3: Experimental value of q versus the amplitude of the sine forcing at 2 MHz for three continuous biases above threshold applied to the QCL. Dashed lines are for visual guidance for the reader

4. Conclusions

We observed in the experimental waveforms that the spikes related to the LFFs occur for a given phase shift which depends on the amplitude of the periodic forcing, the value of the DC bias applied to the QCL and the frequency of the forcing. The number of spikes per period also depends on these parameters. This work is of prime importance to further understand the deterministic chaotic behaviors in QCLs in order to develop free-space secure communications and models to mimic the activity of the human brain.

5. References

[1] Faist, J. et al., *Science*, *264* (5158), 553-556. (1994).
[2] Capasso, F. et al., *IEEE Journal of Quantum Electronics*, *38*(6), 511-532. (2002).
[3] Jumpertz, L, Nonlinear Photonics in Mid-infrared Quantum Cascade Laser, Springer (2017).
[4] Mendez, J. M. et al., *Physical Review E*, *63*, 066218. (2001).
[5] Tiana-Alsina, J. et al., *Optics Express* 26, 7. (2018).
[6] Spitz, O. al., *Quantum sensing and Nano Electronics and Photonics XV, vol. 10540, 105401N*, (Proceedings SPIE Photonics West 2018).

Acknowledgements

This work is supported by the French DGA, the French ANR program, the Office of Naval Research and the National Science Foundation.

Terahertz self-detection near-field microscopy: recent advances in the weak feedback regime

M. Brambilla[1]*, C. Silvestri[2], L. L. Columbo[2], G. Scamarcio[1]

1. Dipartimento Interateneo di Fisica, Università degli Studi e Politecnico di Bari, and CNR-IFN, via Amendola 173, I- 70126 Bari, Italy

2. Dipartimento di Elettronica e Telecomunicazioni, Politecnico di Torino, Corso Duca degli Abruzzi 24, 10129 Torino, Italy

**massimo.brambilla@uniba.it*

Summary: By exploiting the modifications of the emitted field in a THz Quantum Cascade Laser (QCL), induced by an optical feedback via self-mixing (SMI) interferometry, it was demonstrated a new scheme for THz self-detection scattering-type Scanning Near-field Optical Microscopy (THz SD-sSNOM). The system is capable to achieve nanoscale (60-70nm) in-plane spatial resolution in both amplitude and phase contrast [1]. Here we propose an original procedure to extract information about the sample optical properties, beyond the "very weak" feedback regime, enhancing the SNR, by exploiting the peculiar nonlinearities governing the laser dynamics in the self-detection configuration.

1 Introduction and theoretical results

The idea at the basis of s-SNOM consists in focusing an incident laser beam on a sharp metallic tip of a Atomic Force Microscope (AFM) placed in close proximity (near-field) of the sample surface and strongly confining the radiation on its nanometric apex. Nanoscale resolved amplitude and phase images can be retrieved by analyzing the scattered radiation as a function of tip position through interferometric techniques [2]. In the THz frequency range (30–300 μm wavelength), where electromagnetic radiation can resonantly interact with fundamental excitations of molecules and solids, s-SNOM also represents an ideal candidate for the optical characterization (e.g. reconstruction of optical response function) of emerging low-dimensional materials and biological-systems.

Although the lack of fast and compact detectors in the range 1-10 THz greatly stimulated the use of the laser itself as source and detector of near-field radiation in self-detection configuration [3,4], only recently some of us showed the possibility to get nanometric resolution $\left(\sim\frac{\lambda}{1000}\right)$ in both amplitude and phase contrast (coherent imaging) [1].

In the experiment described in details in ref. [1] and sketched in Figure 1a the detected signal is represented by the voltage change (ΔV) across the electrical contacts of a THz QCL emitting at 2.7 THz induced by the SMI effect [5] where a small fraction ($10^{-4} \div 10^{-2}$) of the field emitted by the laser source and scattered by the tip-sample system coherently interferes within the laser intracavity field. As done in conventional s-SNOM, in order to eliminate the background scattering, while the sample is scanned the AFM is operated in the dynamic mode where the tip oscillates with a frequency Ω of tens of KHz and the SMI signal ΔV is demodulated at the lower harmonic frequencies nΩ, n=1…5 by a lock-in amplifier to give its harmonic amplitudes ΔV_n.

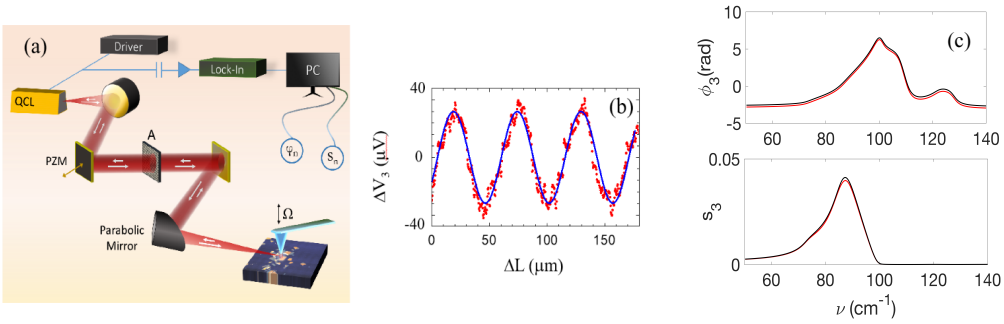

Figure 1: Self-detection s-SNOM at THz frequencies. (a) Schematic diagram of the experiment [1]. The distance $L \approx$ 60 cm between the QCL front facet and the tip can be varied by translating the piezoelectric mirror PZM. (b), (c) Amplitude and phase resolved THz nanoscopy on a resonant polar crystal of CsBr. (b) "Very weak" feedback regime: measured third harmonic of the SD signal (red symbols) and fitting function (blue line) used to extract the scattering amplitude (s_3) and phase (φ_3) as a function of the mirror displacement ΔL. (c) "Weak" feedback regime: simulated (red line) and calculated (black line) scattering amplitude (s3) and phase (φ3) for a fixed mirror position as a function of wave number ν.

By extending the well-known Lang-Kobayashi (LK) model [6] to encompass a complex sample permittivity, the relation between ΔV_n and the sample material optical properties is given by the Eq. (1) [1]:

$$\Delta V_n = \gamma s_n \cos(\omega_F \tfrac{2L}{c} - \varphi_n),\ \left(\Delta V_{\frac{\pi}{2}}\right)_n = -\gamma s_n \sin(\omega_F \tfrac{2L}{c} - \varphi_n) \qquad (1)$$

where s_n and φ_n are the amplitude and phase of the harmonic components of the scattering coefficient σ that is proportional to the effective polarizability of the tip-sample system in finite dipole approximation [7] and thus provides information about the optical response of the sample material. In Eq. (1) $\omega_F = 2\pi\ c\ /\ \lambda_F$ is the laser frequency perturbed by the presence of feedback [5], L is the laser-to-tip distance which varies due to the piezoelectric mirror (PZM) displacement and γ is a proportionality factor. Finally $\left(\Delta V_{\frac{\pi}{2}}\right)_n$ are the harmonic amplitude of the $\frac{\pi}{2}$ - shifted signal $\Delta V_{\frac{\pi}{2}}$ corresponding to the mirror displacement $\Delta L = \frac{\pi c}{4\omega_F}$.

In the "very weak" feedback regime, obtained by employing an attenuator A to reduce the optical feedback in the THz QCL, ω_F is very close to the free running laser frequency ω_0 and the optical coefficients s_n and φ_n , n = 1...5, can be easily extracted by combining the experimentally accessible quantities $\left(\Delta V_{\frac{\pi}{2}}\right)_n$ and ΔV_n:

$$s_n = \frac{1}{\gamma}\sqrt{\Delta V_n^2 + \left(\Delta V_{\frac{\pi}{2}}\right)_n^2} \qquad \varphi_n = \omega_0 \tfrac{2L}{c} + \tan^{-1}\frac{\left(\Delta V_{\frac{\pi}{2}}\right)_n}{\Delta V_n} \qquad (2)$$

or by considering a mirror displacement ΔL of few wavelengths and a fitting procedure based on Eq. (1) as illustrated in Figure 1b.

In order to increase the signal to noise ratio, that is actually limited by the small amount of back reflected radiation in the "very weak" regime, we have theoretically investigated the possibility to operate in regimes of higher feedback. In this case although the laser frequency ω_F is determined by a nonlinear transcendental equation in the LK model, analytical corrections can be determined so that at first order in the feedback strength (corresponding to the "weak" feedback regime) we get the following reconstruction formulas were two additional experimental determination of shifted signals are needed with respect to Eq. (2):

$$s_n = \frac{1}{2\gamma}\sqrt{\left[\left(\Delta V_{\frac{3\pi}{2}}\right)_n - \left(\Delta V_{\frac{\pi}{2}}\right)_n\right]^2 + \left[(\Delta V\ )_n - (\Delta V_\pi)_n\right]^2}, \quad \varphi_n = \omega_0 \tfrac{2L}{c} - \tan^{-1}\left[\frac{\left(\Delta V_{\frac{3\pi}{2}}\right)_n - \left(\Delta V_{\frac{\pi}{2}}\right)_n}{(\Delta V\ )_n - (\Delta V_\pi)_n}\right] \qquad (3)$$

The validity of this approximated approach is evident in Figure 1c where we report for CsBr the optical coefficients analytically calculated through finite dipole theory [7] together with those reconstructed through the numerical simulated SMI signals and the use of Eq. (3) for a fixed mirror position and as a function of the radiation wave number. These results also highlights the great impact on spectrally resolved optical nanoscopy that THz self-detection s-SNOM would have in case of broadly tunable THz QCLs [8] light sources.

3. Conclusion

We propose an original approach to enhance the signal to noise ratio in THz SD s-SNOM where, in the "weak" feedback regime, the amplitude and phase information on the scattering coefficient at the basis of coherent imaging and spectrally resolved nanoscopy are extracted by a proper combination of experimentally accessible SMI signals.

4. References

[1] M. C. Giordano et al., "Title," Phase-resolved terahertz self-detection near- field microscopy, vol. 26, pp. 18423-18435, 2018.

[2] F. Keilmann and R. Hillenbrand, "Near-Field Nanoscopy by Elastic Light Scattering from a Tip", in Nano- Optics and Near-Field Optical Microscopy, Zayats, & A. D. Richards, eds., Artech House, Boston, London (2009).

[3] P. Dean et al., "Apertureless near-field THz imaging using the self-mixing effect in a quantum cascade laser," Appl. Phys. Lett., vol. 108, 091113, 2016.

[4] R. Degl'Innocenti et al. , "Terahertz nanoscopy of plasmonic resonances with a quantum cascade laser," ACS Photonics, vol. 4, pp. 2150–2157, 2017.

[5] G.Giuliani and S.Donati,"Laser interferometry",in Unlocking Dynamical Diversity, JohnWiley & Sons,Ltd, pp. 217–255 (2005).

[6] R. Lang and K. Kobayashi, "External optical feedback effects on semiconductor injection laser properties," IEEE J. Quantum Electron., vol. 16, pp. 347–355, 1980.

[7] S. Amarie and F. Keilmann, "Broadband-infrared assessment of phonon resonance in scattering-type near-field microscopy," Phys. Rev. B,vol. 83, 045404, 2011.

[8] M. S. Vitiello and A. Tredicucci, "Tunable emission in Terahertz quantum cascade lasers," IEEE Trans. Terahertz Sci. Technol., vol. 1, pp. 76–84, 2011.